XFEL.EU THESIS-2017-004

X-ray Beam Characterization for Single Particle Imaging Experiments at Free Electron Lasers: Optimizing Wavefront Measurements

by

Masoud Mehrjoo

Hamburg, November 2017

European X-Ray Free-Electron Laser Facility GmbH

Holzkoppel 4

22869 Schenefeld

Germany

X-ray beam characterization for single particle imaging experiments at Free Electron Lasers: optimizing wavefront measurements

Dissertation

**zur Erlangung des Doktorgrades
des Fachbereich Physik
der Universität Hamburg**

vorgelegt von

Masoud Mehrjoo

Hamburg
2017

Gutachter der Dissertation	Dr. Thomas Tschentscher Prof. Dr. Henry Chapman
Gutachter der Disputation	Dr. Thomas Tschentscher Prof. Dr. Henry Chapman Prof. Dr. Jochen Küpper Prof. Dr. Christian Schroer Prof. Dr. Daniela Pfannkuche
Datum der Disputation	October 27 2017
Vorsitzende des Prüfungsausschusses	Prof. Dr. Daniela Pfannkuche
Vorsitzender des Promotionsausschusses	Prof. Dr. Wolfgang Hansen
Dekan der Fakultät für Mathematik, Informatik und Naturwissenschaften	Prof. Dr. Heinrich Graener

Eidesstattliche Erklärung

Hiermit erkläre ich an Eides statt, dass ich die vorliegende Dissertationsschrift selbst verfasst und keine anderen als die angegebenen Quellen und Hilfsmittel benutzt habe.

Die Arbeit wurde bisher keiner anderen Prüfungsbehörde vorgelegt und auch noch nicht veröffentlicht.

Ort, Datum

Masoud Mehrjoo

Abstract

Free-Electron-Lasers (FELs) have enabled tremendous possibilities in x-ray science due to their ultrashort, highly intense and coherent radiation. At present, FELs rely primarily on the Self Amplified Spontaneous Emission process, which is of a stochastic nature, and emit pulses which may fluctuate drastically from shot to shot. Since many of the novel experiments at FELs require a high degree of beam focusing, in particular for imaging single non-crystalline biological particles, it is imperative to characterize the specific properties of single-shot focused complex wave fields versus different states of the FEL machine. Therefore, a deterministic approach applicable to various FEL operation regimes is desirable to enable the investigation of photon beam properties. The statistical evaluation of the determined properties over different ensembles of pulses leads to an understanding of and potentially optimization of the radiation to be delivered.

In this thesis, I have studied different realizations and methods of focused wave field determination at beamline BL2 at the Free electron Laser At Hamburg (FLASH) for various radiation regimes. An iterative diffraction imaging technique has been developed to study highly coherent pulses. The method comprises of a phase retrieval algorithm applied to single far-field diffraction patterns of highly focused pulses. Also, the Hartmann Wavefront Sensing method, as a classical approach, has been applied to measure photon beam properties in the same machine state. The comparison of results has built confidence in the validity of the imaging method.

A transition to partially coherent radiation caused the algorithmic convergence of the iterative technique to fail. Therefore, a general iterative algorithm has been demonstrated based on Schell's theorem to reconstruct single-shot complex wave fields, as well as estimating the spatial degree of coherence. The properties of measured pulses have been determined with the lowest level of available information compared to the conventional methods, as a single-shot 2D diffraction pattern measured in the far-field. These imaging methods are applicable across a very broad photon energy range since no absorptive optics are needed between the focusing optics and the detector.

Additionally, the variation in longitudinal source position within the operating undulator segments has been determined precisely as feedback from both algorithms, providing further insight into how FEL machine parameters influence the optical properties of the photon beam.

Kurzfassung

Freie Elektronen Laser (FELs) haben dank ihrer ultrakurzen, hochintensiven und kohärenten Strahlung hervorragende Möglichkeiten im Bereich der Wissenschaft mit Röntgenstrahlung geschaffen. Zur Zeit basieren die meisten FELs auf dem Mechanismus der Selbstverstaerkung spontaner Emission (englische Abk. SASE), einem stochastischen Prozess, was sich in der Emission von Pulsen mit stark fluktuierenden Eigenschaften manifestiert. Eine Vielzahl neuartiger Experimente an FELs bedarf stark fokussierter Strahlung. Insbesondere für die Abbildung einzelner, nichtkristalliner, biologischer Teilchen, wird daher eine genaue Charakterisierung spezifischer Eigenschaften des komplexen Wellenfeldes des FELs in Abhängigkeit der Maschinenparameter für jeden einzelnen Schuss benötigt. Ein deterministischer Zugang, der auf verschiedene FEL Strahlungsregime angewendet werden kann ist zur Untersuchung der Röntgenstrahleigenschaften wnschenswert. Eine statistische Auswertung der ermittelten Eigenschaften für eine Anzahl verschiedener Pulsensembles führt somit zu einem Verständnis der Strahlungscharakteristiken und kann potenziel zur Optimierung dieser verwendet werden. Die systematische Veränderung der Strahlungsregime und quantitative Messung von Pulsen, die sich von Schuss zu Schuss innerhalb des Ensembles unterscheiden, erlaubt die Beobachtung der Variabilität gemessener Parameter zwischen verschiedenen Ensemblen.

In dieser Arbeit werden verschiedene Realisierungen und Methoden der Messung fokussierter Lichtfelder an der Beamline BL2 am Freie Elektronenlaser Hamburg (FLASH) in unterschiedlichen Strahlungsregimen untersucht. Für hochgradig kohärente Strahlung wird eine iterative Beugungsbildgebungstechnik weiterentwickelt, die Phasenrekonstruktion auf einzelne Fernfeld-Beugungsmuster von hochfokussierten Pulsen anwendet. Ein Vergleich mit dem klassischen Wellenfront-Messverfahren nach Hartmann schafft hierbei Vertrauen in die Gültigkeit der neuentwickelten iterativen Methode.

Für partiell kohärente Pulse konvergiert die iterative Methode jedoch nicht. Daher wird ein verallgemeinerter iterativer Algorithmus entwickelt und demonstriert, der Konzepte der optischen Theorie partiell kohärenter Rntgenstrahlen, basierend auf dem Schellschen Theorem, benutzt. Dieser Algorithmus erlaubt sowohl die Rekonstruktion des komplexen Wellenfeldes als auch eine Abschätzung der räumlichen Kohärenz einzelner Pulse. Der so ermittelte Kohärenzgrad in verschiedenen Strahlungsregimen ist in guter Übereinstimmung mit Simulationen der FEL Strahleigenschaften. Im Vergleich zu herkömmlichen Methoden wird hierbei der Kohärenzgrad und andere Parameter des Wellenfeldes mit der geringstmöglichen Menge an verfügbarer Information, der Messung eines einzelnen zweidimensionalen Beugungsmusters, gewonnen. Diese bildgeben-

den Verfahren sind über einen sehr breiten Bereich von Photonenenergien anwendbar, da keine absorbierenden optischen Elemente zwischen der fokussierenden Optik und dem Detektor benötigt sind.

Als zusätzliche Information kann ferner die longitudinale Quellposition im aktiven Undulatorsegment aus beiden Algorithmen genau ermittelt werden. Dies liefert weiteren Aufschluss darüber wie die Maschinenparameter des FELs die optischen Eigenschaften des Röntgenstrahls beeinflussen.

Publication

This project has resulted in a journal article that has been published. Presentations have also been made at various conferences, some of which are based on the work presented in this thesis. The publication is listed here for reference.

1. **M. Mehrjoo**, K. Giewekemeyer, P. Vagovic, S. Stern, R. Bean, M. Messerschmidt, B. Keitel, E. Plönjes, M. Kuhlmann, T. Mey, E.A. Schneidmiller, M.V. Yurkov, T. Limberg, A.P. Mancuso "*Single-Shot Measurements of Focused FEL Fields using Iterative Phase Retrieval*" , Opt. Express, Vol. 25, Issue 15, 17892-17903 (2017)

Contents

CHAPTER 1

Introduction

The advent of and rapid advances in synchrotron sources enables the determination of the structure and variability of crystalline biological specimens, such as protein and molecular structures[1] which have important practical ramifications, such as the development of medicines. X-ray crystallography is by far the most prolific method to visualize protein structure at the atomic level and enhances our understanding of protein function. One the key practical limitations of crystallography structure determination is that some of the most interesting proteins can not be crystallized, or are unable to be crystallized readily[2, 3, 4].

Recently, X-ray Free-Electron-Lasers (FELs)[5] have demonstrated the potential to determine the structure of small biological particle such as viruses and macromolecules in their native environment, without the need for crystallization and chemical staining[6, 7]. The unique properties of FELs such as ultrashort, high peak power and highly coherent pulses have led to the introduction of a new field of microscopy called Coherent X-ray Diffraction Imaging (CXDI) which allows the imaging of individual and very weakly scattering particles in a single-shot[8, 9, 10].

Coherent x-ray diffraction imaging is a method whereby one plane of diffraction data may be transformed into an image of the sample by phasing diffraction patterns. This can be in two-dimensions from a single measurement. To phase a diffraction pattern in the context of CXDI, different phase retrieval algorithms have been introduced (for example, see Chapter4), utilizing the different propagation formalism between the sample and detector[11, 12]. For example, in plane-wave illumination of the sample, the Fourier transform is often sufficient to describe the propagation between the sample and detector located in the far field.

To determine the structure of extremely small particles, or equivalently weak scatterer samples, a high degree of beam focusing is required to obtain the highest intensity probing the sample located in a downstream of the focus. Imaging a sample with a divergent illuminating beam introduces a robust technique of x-ray microscopy called Fresnel Coherent Diffraction Imaging (FCDI)[13, 6].

Here, the physical exit wave leaving the sample is related to a direct multiplication of the incident wave and the sample's 3D refractive index function. Therefore, phasing the diffraction pattern results in resolving a complex wave field containing the information of the sample and illuminating wave field.

To this end, the wave illuminating the sample must be known in order to correctly separate its features from those of the incident beam. This realization plays an important role to quantitatively interpret the structure of the sample investigated, and is called Wave Field Determination or Characterization of focused X-ray pulses.

FELs primarily rely on the stochastic nature of the Self-Amplification of Spontaneous Emission (SASE) process, and emit pulses which may fluctuate from shot-to-shot[5]. This statistical nature of FELs demands a comprehensive technique to characterize wave field properties on a single-shot basis. It potentially allows further statistical analysis over classes of determined properties to understand and optimize the radiation delivered, as well as the source characteristics.

Over the last few years, a variety of techniques have been developed to characterize FEL pulses, such as X-ray Grating Interferometry (XGI), Knife-edge scans, Ptychography Coherent X-ray Imaging (PCDI) and Imprints which are briefly described here as a background to the approaches developed in this thesis (see Chapters3-4-5)).

X-ray Grating Interferometry

It has been demonstrated that interferometry can be used as a well-established technique for spatially resolved *in situ* investigation of X-ray wave fields at synchrotrons and XFEL facilities[14, 15, 16]. Interferometry enables an at-wavelength characterization of the optical components and to determine, in a non-invasive manner, eventual fluctuations of wave field properties. The principle of x-ray grating interferometry is based on the Talbot effect. Following the diffraction by a periodic grating illuminated by the x-rays, the propagation direction changes by a small shear angle and, at certain-discrete distances downstream of the grating, a constructive interference pattern appears. Any transverse variation in the wave field induce a lateral displacement in the measured interference pattern. Recent theoretical developments showed that the complex wave field of x-ray pulses can be retrieved using the diffraction measured up to a certain-limited resolution[17, 18, 19].

The angular sensitivity of grating interferometer depends on the grating-to-detector distance and inversely on the period of the grating. The latter parameter also determines the period of the diffraction pattern which may not always be resolved by position sensitive detectors for practical grating pitches. Therefore, a second grating (absorption grating) having a period matching the Talbot pattern is often inserted in front of the detector as a transmission mask, creating a *Moiré* pattern that can be conventionally measured in a single-shot basis (fig.1.1).

For a parallel beam geometry (fig.1.1), the spatial resolution of grating interferometry is limited by either the pixel size of the detector or the pitch of the absorption grating, and thus, by the manufacturing process. More generally speaking, the performance of interferometry essentially depends on the quality of the grating. In addition, when interferometry applies to hard X-ray pulses the fabrication of the grating becomes more crucial. For example, the beam splitter grating G_1 (shown in fig.1.1) should consist of a low absorbing, phase shifting structure. G_2 would be designed precisely with a

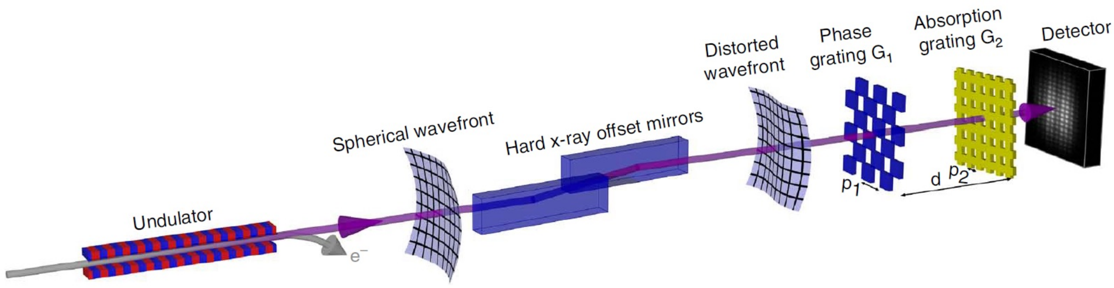

Figure 1.1: Experimental setup for single-shot wavefront sensing using XGI technique. The grating interferometer consists of a checkerboard pattern silicon phase grating G_1 and a gold absorption grating G_2, located at a distance d from the phase grating. In combination they generate a *moiré* pattern, from which the wavefront distrotion can be extracted.[14]

micrometer scale period and well-uniform structure. Its thickness has to provide a high contrast as well.

Knife-edge scans

In the Knife-Edge technique (also referred to as scanning knife edge) a sharp knife edge is scanned across the beam axis, and the total intensity of the transmitting beam is recorded as a function of the edge position[20, 21, 22]. The numerical differential of the measured intensity profile gives the line-spread function of the beam spot (fig.1.2).

The knife edge of the conventional method must be sharp and fully opaque. To satisfy these requirements, the penetration length of the knife-edge material must be smaller than the depth of focus. When the focal spot size in the hard X-ray region reaches a nanometer order, no ideal knife edge exists because the depth of focus becomes smaller than the penetration length. The validity of this method mostly relies on the assumptions that the beam profile has a well-defined, stable shape (mainly of a Gaussian profile) and that the scanning steps are sufficiently precise.[24]. Since FEL pulses fluctuate shot-to-shot, the variation of focus position and intensity distribution may result in observing an average profile of the beam; an over-estimation of the beam size.

Coherent X-ray Ptychography

Scanning coherent diffraction microscopy, also known as ptychography, has revolutionized nanobeam characterization at synchrotron radiation sources. In this X-ray microscopy technique, a sample is scanned on a grid perpendicular to the optical axis; through a confined, coherent beam; recording at each position of the scan a far-field diffraction pattern[25, 26] (fig.1.3).

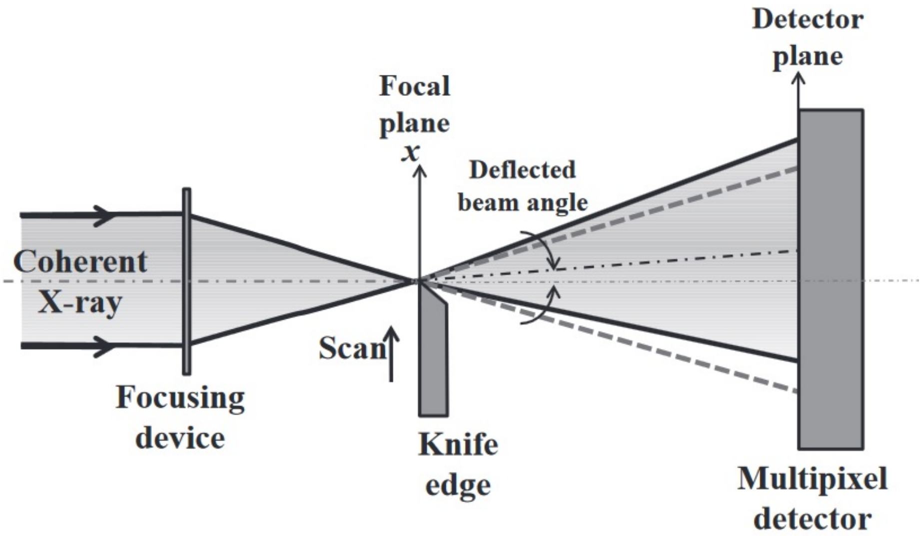

Figure 1.2: Conceptual drawing of microbeam knife-edge scan system with differential-phase-contrast mode.[23]

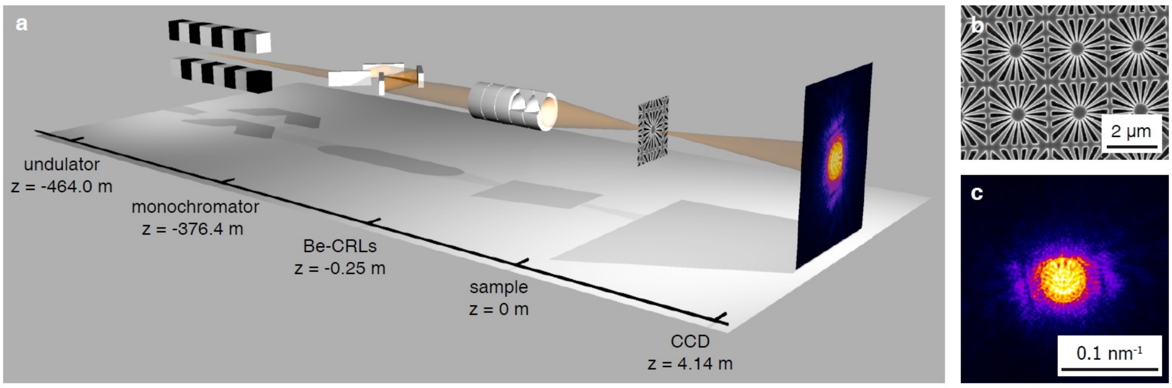

Figure 1.3: Description of ptychography setup and sample. (a) Schematic outline of the experimental setup. Optical axis is not to scale. (b) Scanning electron microscope (SEM) image of a high-resolution test chart made of a 40 by 40 array of starlike structures, patterned into a tungsten layer (thickness 1 mm) on a diamond substrate (thickness 100 mm). Its smallest features have a size of about 50 nm. (c) Single-pulse far-field diffraction pattern recorded as part of the ptychographic dataset (logarithmic scale)[25].

From these overlapping data, the complex transmission function, describing both the attenuation and phase shift by the sample, and the complex illuminating wave field can be reconstructed quantitatively by iterative phase retrieval algorithms. Therefore, a set of scan points (typically few measured scanning points) over a region of interest of the sample is needed to reconstruct the illuminating probe. The result delivers an average probe reconstruction that predominantly assumes a stable illumination. The method requires a large number of measurements. As such, shot-to-shot variations in the focus properties will not be captured. The reconstruction, albeit showing superb spatial resolution, reflects the properties of a statistical average.

It was shown that the method can reconstruct the illuminating probe from a single-pulse diffraction pattern, however, the comparison with a reconstructed average beam showed a more precise reconstruction[25]. In addition, the assumption of fully coherent illumination might not hold in many practical situations. The recent progresses showed that partially coherent beams could be retrieved by using ptychography if a mixture of coherent states is assumed[27]. Nevertheless, the validity of this assumption still requires a well-defined illuminating probe.

Imprints

Imprint techniques have predominantly been used to estimate FEL focus sizes with excellent spatial resolution as shown in [28]. For this purpose, single highly intense X-ray pulses illuminate a flat surface of a typically metallic sample and the ablated holes allows an estimation of the focus spot size and shape[29, 30]. Plotting the ablation imprint areas, created by single-shots in a solid material, in relation to the pulse energy logarithm should provide a linear sequence to be fitted by a line. The beam spot area is then given by the slope of the linear fit and the ablation threshold pulse energy is determined by a linear extrapolation to zero imprint area, i.e, no surface damage[30].

Practically, the random shot-to-shot fluctuations of XFEL pulse energy can be monitored in the focal spot. The interpretation of the results is statistical in nature and thus demands a large number of measurements. Moreover, the complex wave field of pulses can not be determined and *in situ* feedback is not provided. The imprints need to typically be retrieved from the focal area and investigated with a high resolution microscope. Additionally, when the pulse intensity distribution fluctuates shot-to-shot the assumption of linear integration may no longer be valid, and the dependence of the imprint pedestal areas on the pulse energy logarithm may become non-linear[30]. Such a non-linear behavior could be incorrectly attributed to material properties and might introduce severe inaccuracies into the results leading to an undesirable misinterpretation of the focus characteristics.

To summarize, in the former approach, pinhole arrays or gratings are designed for a limited range of photon energies. The accuracy of reconstructions specifically relies on the assumption of a small angle deflection, which decreases the sensitivity to small local phase changes[31]. The latter approach require a large ensemble of measurements, in the presence of a sample, to retrieve the illuminating probe. Intuitively, shot-to-shot fluctuations of the focus properties will not be resolved and a statistically averaged picture of the focused beam is obtained.[32]

A solution to overcome these problems is to use an iterative diffractive imaging technique[33, 34, 35] applied to single far-field diffraction patterns of a highly focused beam[36, 13]. This method comprises an Iterative Phase Retrieval Algorithm (IPRA) with real space and intensity modulus constraints, utilizing the spherical phase curvature of the focused beam. This modification results in the fast, reliable and predominantly unique convergence of the algorithm[37, 38].

In this thesis, an extension of this method to systematically characterize highly focused X-ray pulses under more general experimental conditions than previously assumed is presented. The technique can be used to explore both the complex wave field information, as well as source-point position and its fluctuations. The latter is particularly interesting for short FEL beamlines and yields valuable information about the gain length of the source. In addition, it is shown that the partial coherence of the illuminating beam can be accommodated into a general algorithm that enables us to retrieve an estimation of the coherence function associated with single shots. This achievement provides a unique vision to dynamic fluctuations of both coherence properties of FEL sources.

The method applies to a very broad photon energy since no manipulative optics or sample is needed between the focusing optics and the detector. In particular, the method enables the characterization of hard X-ray pulses measured in far-field of focusing optics without either a need for the unique fabrication process or scanning over a sample upstream of the detector. The numerical implementation of the method discussed within this thesis shows the feasibility of the iterative method to converge reliably when the specified conditions are met for the given energy that practically allows the method applies to soft and hard x-ray beamlines, solely by a change in the generic geometry of x-ray microscopy proposed within the next chapters. As it will be shown later, for the soft and hard x-ray wave field determination the far field condition to measure diffraction patterns varies in order of few meters. This realization is often compatible with the availabilities provided in most beamlines, such as those reported at the SPB/SFX instrument at the European XFEL for hard x-ray energy range or as an alternative to the softer photon energy at the FLASH beamline BL2.

The wave field characterization experiments presented in this thesis were conducted at FLASH beamline BL2. FLASH, the Free-electron LASer in Hamburg, is the world's first free-electron laser for extremely bright and ultra short pulses in the extreme ultraviolet and soft x-ray range. The soft x-ray output, based on the SASE process, possesses unprecedented flux about 10^{13} photons per pulse with pulse duration in the femtosecond range and a high level of spatial coherence. The FLASH source provides a tuning range from 40 - 10nm [39].

The ability to use varying groups of undulators (diverse gain regimes[5]), as well as distinct longitudinal electron bunch compressions (radiation's mode reduction[40]), made FLASH suitable for the study of FEL source radiation. This can be considered as a comparative investigation to XFELs, which practically shares many similarities to the European XFEL, though for a different operational wavelength range.

Outline

The thesis is organized as follows. Within Chapter 2, selected aspects of wave field determination are described. The purpose is to outline the necessary mathematical and numerical tools for the implementation of the optical modeling techniques used throughout the thesis.

Chapter 3 describes the Hartmann Wavefront Sensing method and different relevant approaches to retrieve a complex wave field by finding local phase gradients. Particular emphasis is placed on the Fourier Demodulation method which forms the basis of all experimental wave field analyses within the chapter.

Chapter 4 presents an extension of an intermediate-far field iterative phase retrieval algorithm to characterize single-shot highly focused x-ray pulses of FLASH, for fully coherent illuminations. First, the main body of the iterative algorithm is described theoretically by introducing a mixed propagation strategy, and later its performance is assessed by numerical simulations. It is shown that the method is capable of reconstructing the complex wave field of pulses to a high resolution, and can resolve small variations in phase. The iterative method allows tracking the longitudinal focus fluctuations with an uncertainty of approximately 2 mm which, in turn, reflects the longitudinal source-positional variations within the active undulator segments with an unprecedented level of accuracy. Additionally, the key issues governing the method's convergence, such as the required coherence level and signal-to-noise ratio, are discussed when different pulses of different radiation regimes apply.

Chapter 5 presents a general multi-feedback algorithmic approach to study wave fields of partially coherent sources. The physical interpretation of measured intensities is described using the Generalized Schell's theorem, using reciprocal constraints of phase retrieval algorithms for reconstruction of partially coherent pulses. This new algorithm delivers an estimate of the coherence function associated with each pulse and provides a statistical insight into the coherence fluctuation as well as the wave field variations, as SASE based sources are statistical in nature. The conditions governing the transition from conventional approaches to the general algorithm are discussed.

The thesis ends with a short summary and conclusion in Chapter 6.

CHAPTER 2

The Fundamentals of Wavefront Determination

In this chapter, an outline of paraxial optics is provided to describe light propagation in free space for different geometrical regimes. Important relations of Fourier theory are reviewed to aid the discussion of the solution of the Helmholtz equation for different geometrical regimes, describing the propagation of an electromagnetic field. Beyond analytical studies, particular numerical aspects are studied to define the proper sampling criteria to satisfy the Nyquist theorem. The phase problem in the context of a complex wave field is reviewed and discussed.

A large body of literature is available on the topic from which a selection ([41]-[42]) was used in the preparation of this chapter.

2.1 Fourier Analysis

The representation of certain functions by expansion into orthogonal functions forms a powerful technique that can be used in a large class of problems. The particular orthogonal set chosen depends on the symmetries involved. We consider an interval [a,b] in a variable ζ with a set of real or complex functions $U_n(\zeta)$, square integrable and orthonormal (satisfying the Dirichlet condition) on the interval [a,b]. The orthonormality condition on the function $U_n(\zeta)$ can be expressed as

$$\int_a^b U_m^*(\zeta) U_n(\zeta) d\zeta = \delta_{mn}, \tag{2.1}$$

where * indicates the complex conjugate counterpart.
An arbitrary function f(ζ), square integrable (in Hilbert space) on the interval [a,b], can be expanded in a series of orthonormal functions $U_n(\zeta)$. If the number of terms in the series is finite (N),

$$f(\zeta) \leftrightarrow \sum_{n=1}^{N} a_n . U_n(\zeta) \tag{2.2}$$

minimizing the mean square error[43]:

$$M_N = \int_a^b |f(\zeta) - \sum_{n=1}^{N} a_n.U_n(\zeta)|^2 d\zeta \tag{2.3}$$

can demonstrate the proper choice of the coefficients as

$$a_n = \int_a^b f(\zeta).U_n^*(\zeta) d\zeta. \tag{2.4}$$

If there exist a finite number N_0 such that for $N > N_0$ the mean square error can be made smaller than any arbitrarily small positive quantity, then the series representation

$$f(\zeta) = \sum_{n=1}^{\infty} a_n.U_n(\zeta) \tag{2.5}$$

with a_n given by (2.4) is said to **converge in the mean** to $f(\zeta)$. Series (2.5) can be rewritten with the explicit form (2.4) for the coefficients a_n :

$$f(\zeta) = \int_a^b \{\sum_{n=0}^{\infty} U_n^*(\zeta')U_n(\zeta)\} f(\zeta') d\zeta'. \tag{2.6}$$

Since this represents any function in the interval (a,b), the bilinear term $U_n^*(\zeta')U_n(\zeta)$ only must exist in the neighborhood of $\zeta = \zeta'$. In fact, the kernel of 2.6 converges to the Dirac's delta function as following,

$$\sum_{n=0}^{\infty} U_n^*(\zeta')U_n(\zeta) = \delta(\zeta - \zeta'). \tag{2.7}$$

This is the so-called **completeness** relation. The most famous orthogonal complete basis functions are *Sine* and *Cosine* which form a **Fourier series**.

Expressing Fourier sets in an exponential form, we can write the Fourier series as

$$f(\zeta) = \sum_{n=0}^{\infty} a_n. \exp(in\zeta), \tag{2.8}$$

where $\sqrt{-1} = \mathrm{i}$.

When f(ζ) is periodic with a period 2L (for example, propagating electromagnetics waves are of periodic nature) the coefficient can be presented as

$$a_m = \frac{1}{2L} \int_{-L}^{L} f(\theta) \exp(i\frac{-m\pi\theta}{L}) d\theta. \tag{2.9}$$

In turn the resulting Fourier series is

$$f(\zeta) = \sum_{n=0}^{\infty} \int_{-L}^{L} f(\theta).\exp(i\frac{n\pi}{L}(\zeta - \theta))d\theta. \tag{2.10}$$

We now let the parameter L approach ∞, transforming the finite interval [-L,L] into the infinite interval $[-\infty,\infty]$. Setting a new parameter space $\frac{n\pi}{L} = k$, $\frac{\pi}{L} = \delta k$, (2.10) introduces a unitary integral operator

$$f(\zeta) = \frac{1}{2\pi} \int_{-\infty}^{\infty} \exp(-ik\zeta)dk \int_{-\infty}^{\infty} f(\theta)\exp(ik\theta)d\theta, \tag{2.11}$$

where $\mathcal{L} = \frac{1}{\sqrt{(2\pi)}} \int_{-\infty}^{\infty} \exp(-ik\zeta)\, dk$, $\mathcal{L}.\mathcal{L}^{\dagger} = \mathbf{1}$ and $\mathbf{1}$ represents the unit operator in Hilbert space. (2.11) is called **Fourier integral theorem**.

We now define $g(\mathbf{k})$ (Hereafter the vectors are being indicated by boldface type) the three dimensional **Fourier transform** of the function $f(\mathbf{x})$ ($\mathbf{x}$ = (x,y,z)) by

$$g(\mathbf{k}) = \frac{1}{(\sqrt{2\pi})^{\frac{3}{2}}} \int_{-\infty}^{\infty} f(\mathbf{x})\exp(i\mathbf{k}.\mathbf{x})d\mathbf{x}, \tag{2.12}$$

and also the **inverse Fourier transform** of $g(\mathbf{k})$ can be expressed as :

$$f(\mathbf{x}) = \frac{1}{(\sqrt{2\pi})^{\frac{3}{2}}} \int_{-\infty}^{\infty} g(\mathbf{k})\exp(-i\mathbf{k}.\mathbf{x})d\mathbf{k}. \tag{2.13}$$

An analogous representation of Fourier transform for D(D=1-3) dimensional reciprocal spaces can be expressed as :

$$g(\mathbf{k}_D) = \frac{1}{(\sqrt{2\pi})^{\frac{D}{2}}} \int_{-\infty}^{\infty} f(\mathbf{x}_D)\exp(i\mathbf{k}_D.\mathbf{x}_D)d\mathbf{x}_D, \tag{2.14}$$

where the subindex D represents a D dimensional vector.
(2.13) may be interpreted as an expansion of a function $f(\mathbf{x})$ in a continuum of plane wave eigenfunctions; $g(\mathbf{k})$ then becomes the amplitude of the wave $\exp(-i\mathbf{k}.\mathbf{x})$. It can be shown[43] that on the space $L^2(\mathbb{R})$ of square-integrable functions on $\mathbb{R}$ the Fourier theorem (2.12,2.13) defines a bijective mapping, i.e. there is a one-to-one correspondence between a function and its Fourier transform and vice versa.

2.1.1 Important properties of the Fourier Transform

Assume that $\mathcal{F}$ represents the Fourier transform of a function. Hereafter, 2D Fourier transforms will be considered mainly within this thesis.
Then If $\mathcal{F}(g) = G$ and $\mathcal{F}(h) = H$, thus

1. **Shifting**

The Fourier transform of a shifted function is given by the Fourier transform of the original times an exponential.
$\mathcal{F}(g(\xi-\xi_0,\eta-\eta_0)) = \exp(i(k_\xi\xi_0+k_\eta\eta_0)).\mathcal{F}(g(\xi,\eta))$,
$\mathcal{F}(g(\xi,\eta).exp(i(k_{\xi_0}\xi+k_{\eta_0}\eta))) = G(k_\xi-k_{\xi_0},k_\eta-k_{\eta_0})$.

2. **Convolution Theorem**
   We define the convolution of two functions as
   h⊗g $\equiv \frac{1}{2\pi}\int_{-\infty}^{\infty} g(\xi,\eta)h(x-\xi,y-\eta)d\xi d\eta$.
   Then the Fourier transform of the convolution can be interpreted as the direct product of the Fourier pairs or the Fourier inverse transfrom of a product of Fourier transform is the convolution of the original function h⊗g.
   $\mathcal{F}(h\otimes g) = G.H$

3. **Correlation Theorem**
   We define the cross correlation of two functions as
   h⊕g $\equiv \frac{1}{2\pi}\int_{-\infty}^{\infty} g(\xi,\eta)h^*(x+\xi,y+\eta)d\xi d\eta = \frac{1}{2\pi}\int_{-\infty}^{\infty} g(\xi-x,\eta-y)h^*(\xi,\eta)d\xi d\eta$.
   Note that as an operator on a pair of functions h and g, the correlation operator generally is not commutative. **Autocorrelation** is one of the desired extensions of cross correlation in the context of optics when h = g. The Fourier transform of the autocorrelation can be interpreted as the *power spectrum* or *energy density* in Fourier space.
   $\mathcal{F}(g\oplus g) = |G|^2$.

4. **Parseval's Theorem**
   Taking the inverse Fourier transform of the previous result and setting the integrand's free parameters to zero, demonstrates a useful relation as follows:
   $\iint_{-\infty}^{\infty}|g|^2d^2r \;\; = \iint_{-\infty}^{\infty}|G|^2d^2k$

5. **Derivation relation**
   Derivatives in real space are translated into a multiplication with the reciprocal coordinate k in Fourier space:
   $\mathcal{F}(\frac{d^n}{dx^n}g) = (ik)^n$ G.

2.2 Maxwell Equations: Propagation of light in free space

It was Maxwell's prediction that light can be described as an electromagnetic wave phenomenon, and that electromagnetic waves of all frequencies could be produced, which drew the attention of physicists and stimulated much theoretical and experimental research into light propagation in free space and matter [41].
The non-source form of Maxwell's equations describes the propagation of light in free space, however, when combined with Lorentz's force equation and Newton's second law of motion, these equations provide a complete description of the classical dynamics of

interacting charged particles and electromagnetic fields.The free space form of Maxwell's equations can be written as below [41]:

$$\nabla.\mathbf{E}(\mathbf{r},t) = 0\,. \tag{2.15}$$

$$\nabla.\mathbf{B}(\mathbf{r},t) = 0\,. \tag{2.16}$$

$$\nabla \times \mathbf{E}(\mathbf{r},t) + \frac{\partial \mathbf{B}(\mathbf{r},t)}{\partial t} = 0\,. \tag{2.17}$$

$$\nabla \times \mathbf{B}(\mathbf{r},t) - \varepsilon_0 \mu_0 \frac{\partial \mathbf{E}(\mathbf{r},t)}{\partial t} = 0\,. \tag{2.18}$$

Here **B** is the magnetic induction, **E** is the electric field, ε_0 and μ_0 are equal to the electric permittivity and magnetic permeability of free space , ∇ and $\nabla\times$ are the three-dimensional gradient and curl operators,$(\mathbf{r}, t)$ is a 4-vector where the first element denotes the displacements vector of an arbitrary 3D coordinate and t is time.
In order to obtain the free-space wave equation for the electric field ,taking the curl of (2.17), one obtains:

$$\nabla[\nabla.\mathbf{E}(\mathbf{r},t)] - \nabla^2 \mathbf{E}(\mathbf{r},t) + \nabla \times \frac{\partial \mathbf{B}(\mathbf{r},t)}{\partial t} = 0. \tag{2.19}$$

The first term of this equation vanishes, due to the free space form of (2.15). Similarly, by taking curl from (2.18) and regarding (2.16) the magnetic field equation can be found. The speed at which the electric and magnetic field disturbances propagate in vacuum, which is called speed of light in free space, is inversely related to the electric permittivity and magnetic permeability of free space as [41]:

$$c = \frac{1}{\sqrt{\varepsilon_0 \mu_0}}. \tag{2.20}$$

The individual components of $\mathbf{E}(\mathbf{r}, t)$ and $\mathbf{B}(\mathbf{r}, t)$ in (2.19) obey all the same scalar equation, suggesting that it is sufficient to study the 3D scalar field $\Psi(\mathbf{r}, t)$, obeying the scalar wave equation. In this manner, we will decompose a wave field as a superposition of monochromatic fields, using the Fourier integral [44] :

$$\Psi(\mathbf{r},t) = \frac{1}{\sqrt{2\pi}} \int_0^\infty \psi_\omega(\mathbf{r}) \exp(i\omega t) d\omega\,. \tag{2.21}$$

Here Ψ describes the scalar electromagnetic field.
Substituting (2.21) in (2.19), one obtains :

$$(\nabla^2 + k^2)\psi_\omega(\mathbf{r}) = 0, \qquad k = \frac{\omega}{c} \tag{2.22}$$

where k is called the wave number and is proportional to the inverse of the wavelength; k $= \frac{2\pi}{\lambda}$.
The time-independent equation for the spatial component $\psi_\omega(\mathbf{r})$ of a monochromatic field

is known as the **Helmholtz equation** which is a central equation of the scalar diffraction theory. Hereafter, we take out the subindex ω to ease notation. In this formalism, even in the presence of an external source $\sigma(\mathbf{r})$, a coherent, monochromatic wave field in a plane transverse to the propagation direction can be described as

$$\psi(\mathbf{r}) = A(\mathbf{r})\exp(i\phi(\mathbf{r})), \tag{2.23}$$

where A and ϕ refer to the amplitude and phase of the complex wave field respectively. Therefore, the wave field contains all information of the source such as its amplitude and phase.

Expanding the 3D Laplacian of (2.22) as $\nabla^2 = \nabla_\perp^2 + \frac{\partial}{\partial z}$, the Helmholtz equation may be written as [45]:

$$\left(\nabla_\perp^2 + \frac{\partial^2}{\partial z^2} + k^2\right)\psi(\rho, 0) = 0\,. \tag{2.24}$$

Here $\nabla_\perp^2$ is the transverse Laplacian operator and $\rho_j = (x_j, y_j)$.

Let us decompose (2.24) as two conjugated operators :

$$L_+ L_- \psi(\rho, 0) = 0\,. \tag{2.25}$$

Hereafter we omit the $\perp$ subindex for simplicity.

$L\pm$ are the propagation operators for the positive and negative z direction

$$L\pm = \frac{\partial}{\partial z} \mp i(k.(1 + \frac{\nabla_\perp^2}{k^2})^{\frac{1}{2}})\,. \tag{2.26}$$

A solution of (2.25) can be the linear combination of the solutions of $L_+\psi = 0$ and $L_-\psi = 0$[43]. Let us call ψ_+ and ψ_- the solution of L_+ and L_-. Thus one can express the solution of (2.26) as $C_1\psi_+ + C_2\psi_-$.

The solution of the $L_+\psi(r)$ describes a wave which travels along the positive z direction. We consider it as the proper solution of (2.26) which means $C_2 = 0$. Thus,

$$\psi_+(\rho, z) = \exp(ikz(1 + \frac{\nabla^2}{k^2})^{\frac{1}{2}})\ \psi(\rho, 0)\,. \tag{2.27}$$

(2.27) is a representation of the **Fresnel diffraction integral** using the Dirac operator[46]. Considering the Fourier space derivative relation, one can map the real space gradient into Fourier space taking the Fourier inverse of both sides of the result,

$$\nabla = i\mathcal{F}^{-1}(\mathbf{k}_\perp)\mathcal{F}\,. \tag{2.28}$$

Consequently the Laplace operator can be written as follows[44]

$$\nabla_\perp^2 = -\mathcal{F}^{-1}(k_x^2 + k_y^2)\mathcal{F}\,, \tag{2.29}$$

where $k_\perp^2 = k_x^2 + k_y^2$.

Substituting (2.29) in (2.27), one can directly obtain

$$\psi_+(\rho, z) = \mathcal{F}^{-1} \exp(iz(k^2 - k_\perp^2)^{\frac{1}{2}})\, \mathcal{F}\psi(\rho, 0)\,. \tag{2.30}$$

Note that all the following propagation equations could also be written as equations relating an arbitrary pair of propagation planes.

Most theoretical treatments of optical wave propagation are concerned with a useful approximation of (2.30), because exact analytical solutions are rare. The most prominent one, experimentally of interest as well, is the **Paraxial approximation**.

2.2.1 Paraxial approximation

Consider again the problem of propagation of a monochromatic wave field $\psi_\omega(\rho, 0)$ from the plane z = 0 into a plane z = const > 0. The paraxial condition for a wave field is introduced as [44],

$$|\Psi_+(k_\perp, 0)|^2 > 0 \qquad only\, for \qquad k >> k_\perp, \tag{2.31}$$

which means the plane wave components will contribute in the propagated field only if their wave vector $(k_\perp, k_z)$ makes a small angle with respect to the optical axis.
The small angle condition, thus can be met in Fourier space as : $\sqrt{k^2 - k_\perp^2} \simeq k - \frac{k_\perp^2}{2k}$.

Using above approximation one can rewrite (2.30) as :

$$\psi_+(\rho, z) \simeq exp(ikz)\mathcal{F}^{-1} \exp(-iz\frac{k_\perp^2}{2k})\; \mathcal{F}\; \psi(\rho, 0)\,. \tag{2.32}$$

Hereafter, we call it as the **Fresnel Near Field Propagation** of a paraxial wave.

The last right hand terms in (2.32) are the Fourier pair of a convolution integral in the real space,

$$\exp(-iz_{ij}\frac{k_\perp^2}{2k})\; \mathcal{F}\; \psi(\rho', z_i) \;=\; -\frac{i}{\lambda z_{ij}}\mathcal{F}(\iint \exp(i\frac{k}{2z_{ij}}(\boldsymbol{\rho} - \boldsymbol{\rho}')^2).\psi(\rho, z_i)\, d^2r). \tag{2.33}$$

Here $z_{ij} = z_i - z_j$ and ρ is the dummy integrand .

Taking the inverse Fourier transform of (2.33), implies that $\psi_+(\rho', z_j)$ can be interpreted as a summation over all spherical waves emanating from the original plane, with amplitude $\psi(\rho, z_i)$. Thus $\psi_+(\rho', z_j)$ can be represented in an integral format ,

$$\psi_+(\rho', z_j) \;\simeq\; -\frac{i}{\lambda z_{ij}} \exp(i\frac{k}{2z_{ij}}\rho'^2) \iint \exp(i\frac{k}{2z_{ij}}\rho^2).\exp(i\frac{k}{z_{ij}}\boldsymbol{\rho}.\boldsymbol{\rho}').\psi(\rho, z_i)\, d^2r. \tag{2.34}$$

Alternating the integrand's exponential argument parameter as $\mathbf{k}_\perp = \frac{k}{z_{ij}}\boldsymbol{\rho}$, (2.34) manifests itself as a single Fourier transform involved propagation operator,

$$\psi_+(\rho', z_j) \;\simeq -\frac{i}{\lambda z_{ij}} \exp(i\frac{k}{2z_{ij}}\rho'^2)\, \mathcal{F}(\exp(i\frac{k}{2z_{ij}}\rho^2)\,.\,\psi(\rho, z_i)). \tag{2.35}$$

Mathematically, we have reduced the convolution form of Fresnel propagation to a simplified Fourier transform version. It is called the **Fresnel Intermediate Field Propagation** of a paraxial wave.

In the context of electrodynamics the **Fresnel number** establishes coarsely the terminology of Near, Intermediate and Far field[47]. Assume a_{max} indicates the diameter of largest area, within that $\psi(x, y)$ varies significantly. Thus the **Fresnel Number** is defined as

$$FN = \frac{a_{max}^2}{\lambda z}. \tag{2.36}$$

When FN>1, propagation is described by different versions of Fresnel operators introduced previously. If FN≪1, the on-axis distance would be larger than the transverse area covered by the lateral field distribution. The exponential integrand in (2.35) vanishes and $\psi_+(\rho', z_j)$ is related to the primary wave by a simple Fourier transform,

$$\psi_+(\rho', z_j) \simeq -\frac{i}{\lambda z_{ij}} \exp(i\frac{k}{2z_{ij}}\rho'^2)\, \mathcal{F}(\psi(\rho, z_i)). \tag{2.37}$$

Eq(2.37) is called the **Far field** or **Fraunhofer propagation** approximation, while the small angle condition is met.

2.3 The sampling theorem

It is often convenient, both for data processing and mathematical analysis purposes, to represent a function by an array of its sampled values on a discrete set of points in a 2D plane. Intuitively, it is clear that if these samples are taken sufficiently close to each other,they would be an accurate representation of the original function. (2.3) represents a class of functions to be minimized through points a and b which illustrates a less obvious fact : for a particular class of functions, so-called **Band-limited Functions**, a discrete representation can fully describe the original function. This result was originally pointed out by *Whittaker*, in 1915, and was later popularized by *Shannon* in his studies of information theory.[48]

The principal impact of the Shannon sampling theorem on information theory is that it allows the replacement of a band-limited signal by a discrete sequence of its samples without the loss of any information.

Theorem 1 *If $f \in \mathbb{C}; \mathbb{C} \subseteq \mathbb{R}$ and F, the Fourier transform of f, is supported on the interval $[-b, b]$, then*

$$f(x) = \sum_{n\in\mathbb{Z}} f(\frac{n}{b})\, \mathrm{sinc}(\pi b(x - \frac{n}{b}))$$

converges to f in $\mathbb{C}$[49].

In other words, the theorem states that if an absolutely integrable function contains no frequencies higher than b, then it is completely determined by its samples at a uniform grid spaced at distances $\frac{1}{2b}$.

A function g is supported on a set $\mathbb{C}$ if it is zero on the complement of this set. The support of g, which we denote by $supp(g)$, is the minimal closed set on which g is supported.

A function $f \in \mathbb{C}$ is band-limited if there exists $b \in \mathbb{C}$ such that $supp(F) \subseteq [-b, b]$. b is a band-limit for f and 2b, the corresponding frequency bandwidth. The supremum of the absolute values of all frequencies of f , is called the **Nyquist rate** [50]. Note that here, to simplify the problem, we assumed a symmetrical frequency distribution.
In (2.8) a proper discrete representation for f, in the real space, has been derived. As a simple proof of theorem 1 , consider the inverse Fourier representation of F, thus

$$F(\eta) = \sum_{n \in \mathbb{Z}} c_n \exp(-\frac{\pi i n \eta}{b}), \tag{2.38}$$

where,

$$c_n = \frac{1}{2b} \int_{-b}^{b} F(\eta) \exp(\frac{\pi i n \eta}{b}) d\eta = \frac{1}{2b} \int_{-\infty}^{\infty} F(\eta) exp(\frac{\pi i n \eta}{b}) d\eta = \frac{1}{2b} f(\frac{n}{b}). \tag{2.39}$$

Therefore ,

$$F(\eta) = \sum_{n \in \mathbb{Z}} \frac{1}{2b} f(\frac{n}{b}) \exp(-\frac{\pi i n \eta}{b}). \tag{2.40}$$

From (2.40) it is already clear that f can be completely recovered by the values $f(\frac{n}{b})$, where the function is sampled at the Nyquist frequency $f_N = b$; half of the supremum of the frequencies in Fourier space. To conclude the recovery formula, it is enough to invert F as follows:

$$\begin{aligned} f(x) &= \int_{-b}^{b} F(\eta) exp(2\pi i x \eta) d\eta = \sum_{n \in z} f(\frac{n}{b}) \frac{1}{2b} \int_{-b}^{b} \exp(\pi i (x - \frac{n}{b}) \eta) d\eta \\ &= \sum_{n \in \mathbb{Z}} f(\frac{n}{b}) \frac{sin(\pi b (x - \frac{n}{b}))}{\pi L (x - \frac{n}{b})} = \sum_{n \in \mathbb{Z}} f(\frac{n}{b}) \mathrm{sinc}(\pi b (x - \frac{n}{b})). \end{aligned} \tag{2.41}$$

Replacing b by $\frac{1}{\delta x}$, one can find the original sampling theorem representation in real space. Note that the sampling theorem can equally be applied in the Fourier domain.

Clearly stated, in principle, for the replacement of any Fourier transform by its discrete analogue, the Nyquist rate needs to be fulfilled. To implement (2.27), using either (2.32) or (2.35), a sufficient criterion that ensures adequate sampling is required. In practice, the best one can do is to ensure that all frequencies present on the numerical grid are represented correctly.
The key to achieve an accurate result when (2.32) or (2.35) are applied, is to sample the quadratic phase factor inside the Fourier or inverse Fourier transform at a high

enough rate to satisfy the Nyquist criterion. If it is not sampled finely enough, it might cause aliasing. The intended higher frequency contents would show up in the lower frequencies[51, 52, 53].
Assume in 1D space, without losing generality, δx.δk $= \frac{2\pi}{N_x}$. where δx and δk are numerical variables in the real and Fourier space. The local rate of phase change is basically given by[47]:

$$f_{local} = \frac{1}{2\pi}\nabla_i\phi \tag{2.42}$$

where i indicates the variable of derivative either x or k_x.

Consider (2.32), the local phase gradient with respect to the frequency variable k_x is:

$$\frac{\partial\phi}{\partial k_x} = \frac{-z.k_x}{k}. \tag{2.43}$$

It can be interpreted as the local frequency in the Fourier space. The Nyquist sampling rate is satisfied when[54]

$$\frac{1}{2\pi}|\frac{\partial\phi}{\partial k_x}|_{max} \leqslant \frac{1}{2\delta k}. \tag{2.44}$$

It can be seen from (2.44) that the largest phase difference between two sampling points may not vary larger than π. It is thus straightforward to finalize the previous steps as,

$$\frac{\lambda z}{N_x(\delta x)^2} \leqslant 1. \tag{2.45}$$

A similar procedure for intermediate propagation utilizing the local frequency variation in the real space demonstrates the numerical constraint on (2.35) as

$$\frac{\lambda z}{N_x(\delta x)^2} \geqslant 1. \tag{2.46}$$

The intermediate field propagation involves a leading phase factor outside the integral which is not sampled generally according to the Nyquist theorem when the integrand is enough finely sampled at or even better than the Nyquist frequency.

Numerically, the 2D discrete Fourier transform takes as its input a 2D discretely sampled array with a pixel size of δx and returns an array of the same size with a pixel size δk $= \frac{2\pi}{N\delta x}$. By (2.34), at the z_j plane, δk $= \frac{k}{z}x$ (to simplify the notation z_{ij} is replaced by z), thus,

$$\delta k.\delta x' = \frac{2\pi}{N} \rightarrow \delta x' = \frac{\lambda z}{N\delta x}. \tag{2.47}$$

Thus, a discrete Fourier transform may shrink or expand the physical extent of an array, depending on the propagation distance and wavelength.

Lastly, we note that the transition to the Fresnel diffraction regime relies on an approximation accurate to second order in $r_\perp$. Luckily, a large body of experimental setups can be designed both in the optical and x-ray regime, where this approximation is very well justified.

2.4 Phase problem

As described by eq(2.23), complex wavefronts are uniquely specified by their modulus and phase as a function of position and time. The modulus (or the amplitude) of the wavefront can be directly measured using readily available detectors such as CCD camera, or even human eye which measures the intensity as the square of the amplitude. However, the phase of the wave field can not be directly measured because it is not currently possible to design detector with a temporal bandwidth comparable to the optical frequencies. Therefore, to fully determine the complex wavefront it is necessary to employ indirect techniques such as the local phase gradient based methods[14, 55, 56, 57] or coherent diffraction imaging phase retrieval[58, 36, 26, 25]. These two methods describes the two main approaches used within this thesis to characterize the wave fields measured at the FLASH beamline BL2. The basic principle of which is described in the following.

2.4.1 Local phase gradient determination

The local phase gradient measurement methods rely on using appropriate manipulative optics to determine the rate of the phase change over localized discrete regions, surrounding the spatial extent of the wave field. Manipulative optics vary from a series of gratings to a simpler array of pinholes modified by using x-ray lenses. Those methods are called **X-ray Grating Interferometry**(XGI) and **Hartmann(-Shack) wavefront sensing**(HWS). The pattern displacement measured downstream of manipulative optics in comparison with a reference pattern leads one to determine the lateral phase derivatives, perpendicular to the on-axis propagation direction. The derivatives then are integrated to exploit the structure of the entire phase. These methods are inherently resolution-limited due to the limited spatial resolution of optical elements.

2.4.2 Coherent diffraction imaging phase retrieval

The essential characteristic of coherent diffraction imaging phase retrieval is the use of numerical techniques to extract information about the phase of the optical wave field by a measurement of the beam. Conventionally, the measured beam is called either diffraction pattern of a localized wave field or the scattered wave filed. It was shown that if the measured pattern is densely enough sampled, the phase can be retrieved in two or three dimensions without losing any information. The sampling requirement in turn implies that the wave field is spatially localized within a closed 2D boundary.

The method is based on an iterative algorithm, starting by a trial wave field. The trial wave is formed by the modulus of the measured intensity and a random phase. Then it numerically propagates between a series of specified planes and is constrained to converge on the original wave field. The imposed constraints are typically the diffraction pattern measured and the spatial extent of the wave field. The recently developed algorithms are flexible enough to reconstruct the wave field by a measurement of the diffraction pattern in the different optical regimes, mainly far and intermediate zone.

An intermediate wave field determination requires measurements of a divergent beam, involving finite curvature. The phase curvature itself imposes a strong constraint to the algorithm, leading to a faster and unique convergence[59]. The approach to phase retrieval algorithm used in this thesis falls into the category of intermediate wave field determination, employing a new algorithm developed for the deterministic recovery of phase information using mixed Fresnel propagators to uniquely determine the phase of single shots.

2.5 Coherence as a statistical property of light

The assumption of strictly static electromagnetic fields has been present in the previous sections up to this point.This assumption may fail in many realistic cases, such as synchrotron and FEL sources, due to the statistical treatment of light[60, 61]. To illustrate this fact, consider an extended source comprising infinite independent point sources. Each point source randomly radiates for some period of time. At the observation point the total radiation field, which due to the superposition principle is the sum of all fields from the individual sources, fluctuates as function of time. These fluctuations are extremely fast and can not be detected, therefore only statistical properties of these fluctuations can be determined. In order to describe adequately a wave field produced by a electrodynamic source it is evidently desirable to introduce a measure for the correlation which might exist between the oscillations at the different points. In[62] it is clearly recognized that the radiation field from such sources can be treated with a correlation function of the complex wave fields.

This statistical measure is given as the Mutual Coherence Function(MCF)[62],

$$\Gamma(\boldsymbol{r_1}, \boldsymbol{r_2}; \tau) \;=\; \langle E^*(\boldsymbol{r_1}, t).E(\boldsymbol{r_2}, t+\tau)\rangle, \tag{2.48}$$

which characterizes the associated time and space fluctuations of the electric field $E(\boldsymbol{r}, t)$. It describes the correlation between two complex wave fields $E(\boldsymbol{r_1}, t)$ and $E(\boldsymbol{r_2}, t+\tau)$ at the different points $\boldsymbol{r_1}$ and $\boldsymbol{r_2}$ and a time difference τ. Indeed, the mutual coherence function is a statistical property which reflects the temporal correlation of the electric field at two positions in space with respect to time. Here, the expectational value denotes the average of all instances of the fields radiated in time,

$$\langle f(t)\rangle = \lim_{T\to\infty} \frac{1}{T}\int_0^T f(t)dt. \tag{2.49}$$

The function Γ is the first order correlation function of the wave field. The mutual coherence function may be normalized against the mean spatial amplitude of the fluctuating electric field. This specifies a quantity known as the Complex Degree of Coherence(CDC), γ_{12}, which is defined by the alternative form[62],

$$\gamma_{12}(\boldsymbol{r_1}, \boldsymbol{r_2}, \tau) = \frac{\Gamma(\boldsymbol{r_1}, \boldsymbol{r_2}, \tau)}{[\langle I(r_1, \tau)\rangle\langle I(r_2, \tau)\rangle]^{\frac{1}{2}}}, \tag{2.50}$$

where$\langle I\rangle$ represents an average intensity over the detection period. γ_{12} is generally a complex function of τ.

The Degree of Coherence (DC) depends on the value of γ_{12} is defined as follows:

1. $|\gamma_{12}(\boldsymbol{r_1}, \boldsymbol{r_2}, \tau)| = 1$ *coherent*
2. $0 < |\gamma_{12}(\boldsymbol{r_1}, \boldsymbol{r_2}, \tau)| < 1$ *partially coherent*
3. $|\gamma_{12}(\boldsymbol{r_1}, \boldsymbol{r_2}, \tau)| = 0$ *incoherent*

When light is partially coherent, $\gamma_{12}(\boldsymbol{r_1}, \boldsymbol{r_2}, \tau)$, is close to unity when $\boldsymbol{r_1} = \boldsymbol{r_2}$ and drops when $|\boldsymbol{r_1} - \boldsymbol{r_2}|$ increases. The area scanned by $r_{1\perp}$, when $r_{2\perp}$ assumed to be fixed, within which the function $|\gamma_{12}|$ is greater than $\frac{1}{e}$ is called the coherence area[63]. It presents the spatial extent of $|\gamma_{12}|$ as a function of the relative distance.

In most FEL experiments neither completely coherent nor completely incoherent radiation is realized and we may frequently speak of fluctuations which are partially coherent. We will address this property later in this thesis (see chapter(5)) and for the moment restrict ourselves to define two fundamental concepts associated with the mutual coherence function of a partially coherent wave field.

- **Cross Spectral Density**

  It was shown in[62] that the mutual coherence function satisfies a pair of wave equations in free space namely,

$$(\nabla_i^2 - \partial_t^2)\, \Gamma(\boldsymbol{r_1}, \boldsymbol{r_2}, \tau) = 0 \quad i = 1, 2\,, \tag{2.51}$$

  where ∂_t^2 is the second order partial derivative in respect to the time difference and i specifies in which of $\boldsymbol{r_1}$ and $\boldsymbol{r_2}$ the Laplacian operates on Γ. By defining a new function as the Fourier transform of Γ,

$$W(\boldsymbol{r_1}, \boldsymbol{r_2}, \omega) = \frac{1}{2} \int \Gamma(\boldsymbol{r_1}, \boldsymbol{r_2}, \tau) \exp(-ik\tau) d\tau, \tag{2.52}$$

  one can utilize eq(2.51) in the frequency domain as,

$$(\nabla_i^2 + k^2) W(\boldsymbol{r_1}, \boldsymbol{r_2}, \omega) = 0, \tag{2.53}$$

  where $k = \frac{\omega}{c}$ is the wave number of light corresponding to frequency ω. W is known as the Cross Spectral Density (CSD) function defining the temporal Fourier transform of the mutual coherence function with respect to the time variable and satisfies the Helmholtz equation. This pair of elliptical differential equations for the cross spectral density is easier to solve than the pair of hyperbolic wave equations for the mutual coherence function; The mutual coherence function then can be readily determined by taking an invers Fourier transform of the cross spectral density.

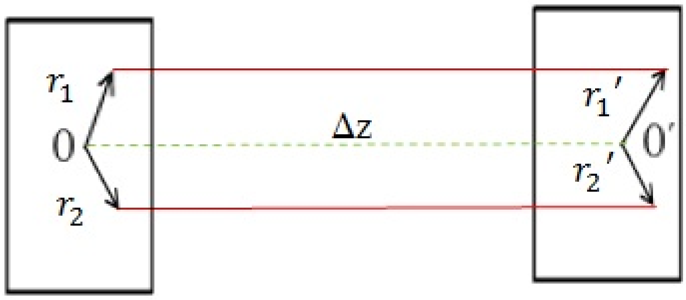

Figure 2.1: The propagation geometry .

- **Mutual Optical Intensity**

  When the source is stationary in time, $\tau = 0$, the mutual coherence function is known as the Mutual Optical Intensity of light[60],

$$J(\boldsymbol{r_1}, \boldsymbol{r_2}) = \Gamma(\boldsymbol{r_1}, \boldsymbol{r_2}, 0). \tag{2.54}$$

Reshaping the propagation of quasi-monochromatic light in free space, eq(2.32) and eq(2.34) represent,

$$E^{'}(\boldsymbol{r_1'}) = \int K(\boldsymbol{r_1} - \boldsymbol{r_1'})E(\boldsymbol{r_1})d^2r_{1\perp} \tag{2.55}$$

where $\boldsymbol{r_1'}$ and $\boldsymbol{r_1}$ are the positional vector of O$^{'}$ and O spaces as shown in fig.(2.1). $K(\boldsymbol{r_1} - \boldsymbol{r_1'})$ represents the free space Kernel of eq(2.32) and eq(2.34).

Therefore, $J(\boldsymbol{r_1'}, \boldsymbol{r_2'})$ can be related to $J(\boldsymbol{r_1}, \boldsymbol{r_2})$ as,

$$\begin{aligned} J(\boldsymbol{r_1'}, \boldsymbol{r_2'}) &= \langle E^*(\boldsymbol{r_1'}).E(\boldsymbol{r_2'})\rangle, \\ J(\boldsymbol{r_1'}, \boldsymbol{r_2'}) &= \iint d^2r_{1\perp} \iint d^2r_{2\perp}\, K^*(\boldsymbol{r_1} - \boldsymbol{r_1'})K(\boldsymbol{r_2} - \boldsymbol{r_2'})\langle E^*(\boldsymbol{r_1})E(\boldsymbol{r_2})\rangle, \\ J(\boldsymbol{r_1'}, \boldsymbol{r_2'}) &= \iint d^2r_{1\perp} \iint d^2r_{2\perp}\, K^*(\boldsymbol{r_1} - \boldsymbol{r_1'})K(\boldsymbol{r_2} - \boldsymbol{r_2'})J(\boldsymbol{r_1}, \boldsymbol{r_2}) \end{aligned} \tag{2.56}$$

The measurable intensity at O$^{'}$ is straightforward obtained when $\boldsymbol{r_1'} = \boldsymbol{r_2'} = \boldsymbol{r'}$,

$$I(\boldsymbol{r'}) = J(\boldsymbol{r'}, \boldsymbol{r'}), \tag{2.57}$$

where $I(\boldsymbol{r'})$ is no longer the modulus of the wave field propagating to O$^{'}$ and would be interpreted as the partially coherent intensity. Indeed, $\gamma_{12}(\boldsymbol{r_1}, \boldsymbol{r_2})$ of J represents the correlation between two transverse points of the wave field at a given plane at the same time, a measure known as the transverse degree of coherence.

CHAPTER 3

Hartmann Wavefront Sensing Method : Theory, Simulation and Experiment

Hartmann Wavefront Sensing (HWS) is known as a classical method that may be applied to characterize single-shot soft x-ray FEL beams to a limited resolution.

In this chapter, the HWS method is introduced and different, relevant approaches to retrieve a complex wavefront by finding local phase gradients are discussed. The Fourier Demodulation (FD) method is described as a fast and reliable approach to reconstruct complex wave field. The successful reconstructions lead to the numerical back propagation of the wave fields and the possibility of the evaluation of the beam parameters from shot-to-shot.

3.1 Different Approaches of the Hartmann wavefront sensing analysis

Hartmann wavefront sensors are widely applied in a broad range of optical science such as adaptive optics and laser beam quality measurements, as well as real time complex wavefront characterization at FELs[64, 65, 66].

A Hartmann wavefront sensing device consists of an array of apertures mounted at a distance L from a 2D imaging unit, and is a simple device that is capable of measuring both pulse intensity and phase distribution in a single frame of data. The key idea of Hartmann wavefront sensing can be explained in the context of ray optics. When a distorted complex wavefront illuminates the pinhole array, each aperture acts as an "optical lever", distributing the diffracted spots into different lateral positions on the detector, proportional to the phase tilt ($\frac{\partial \phi}{\partial x_i}$) over the aperture(fig.3.1)[67, 68]. Here, $\frac{\partial}{\partial x_i}$ presents a partial derivative in X or Y direction in a Cartesian coordinate. ϕ is a 2D real function ascribed as the phase of the wave field in Cartesian coordinate.

The dissected diffraction pattern can be analyzed either in the image or Fourier domain to obtain the phase gradient (derivatives). The first and more common approach is the *centroid method* [69, 70, 71, 72]. Here the local phase gradient at each spot is individually measured. Typically, a reference spot pattern is measured as an average of many single shots (black spots in fig.3.1). The measured diffraction patterns must be divided into a

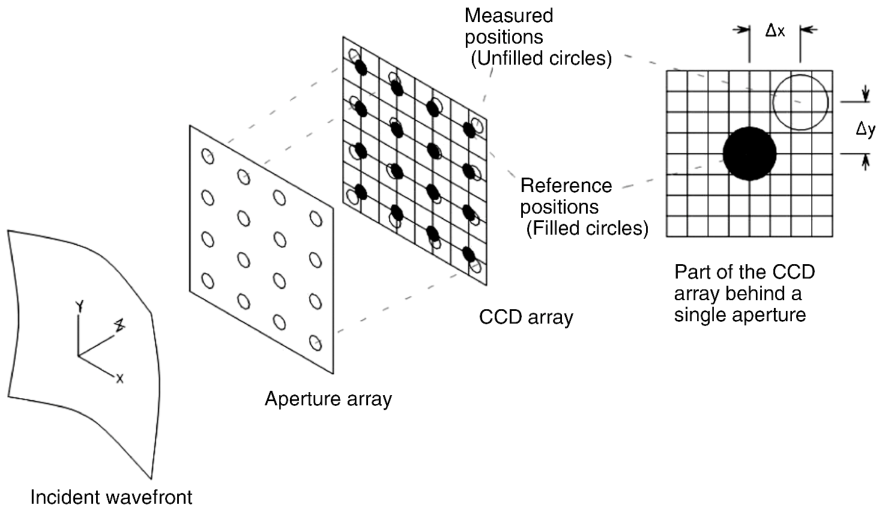

Figure 3.1: Principle of The HS operation. The scheme shows an incident wave field traveling along the optical axis illuminating an aperture array and the diffracted spots distributed in a CCD. [68]. The displacement of the diffracted spots leads to retrieve the complex wavefront.

set of small window grids, each centered on a spot peak, with one window per pinhole (a single window is shown in fig.3.1). Thus, the diffracted spot locations, within the defined windows, are determined from centroids along the lateral directions, for the reference and illuminating wave, as shown in fig.(3.1). Correspondingly, geometrical displacements (ΔX and ΔY) provide a measure of the phase gradient in each direction.

An alternative method is the *Fourier demodulation* [73, 74, 75, 76, 77, 78]. In this technique the recorded intensity pattern is considered as a whole, rather than investigating each individual spot by itself. This implementation enables a direct measurement of the geometrical displacements in Fourier domain.

In the following sections we will explain the *Fourier demodulation* method as a fast and easily automized approach to study Hartmann wavefront sensing single-shots data analysis based on the data collected at the FLASH beamline BL2.

3.2 Fourier demodulation method

When a plane wave illuminates the Hartmann pinhole array, the irradiance function of the detected pattern at the detector plane can be expressed as a direct product of a grating modulation function and the transmitted wave pattern amplitude[79, 80] as,

$$I(\mathbf{r}) = V(\mathbf{r})(1 + \frac{1}{2}\sum_{i=x,y} \exp(\pm i k_i r_i)), \tag{3.1}$$

where $V(\mathbf{r})$ is the complex valued pattern amplitude at location $\mathbf{r} = (x, y)$ and is assumed to be slowly varying and non-vanishing within the aperture.

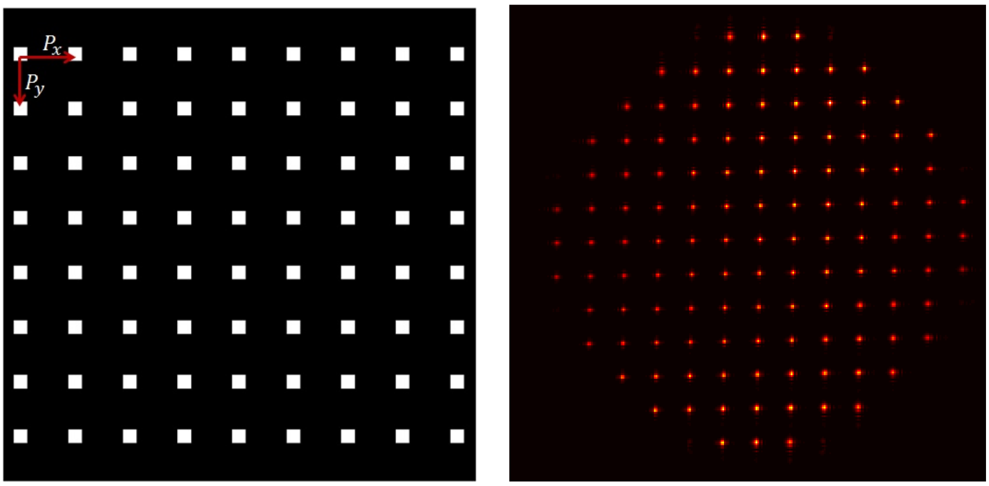

(a) (b)

Figure 3.2: Typical Hartmann plate (a) and measured modulated diffraction pattern(b) for a single shot exposure. $P_i s$ indicate the transverse array pitch sizes . Note that in (b) the incoming wave illuminates the Hartmann-plate only partially.

The illumination of the pinhole array with a distorted wavefront causes a local gradient over each aperture, causing a irregular displacement of the entire pattern. The gauge translation relates the new coordinate to the rest frame, as sketched in fig.(3.3). It can be mathematically expressed as,

$$\frac{\nabla\phi}{k} \approx \frac{\Delta\mathbf{r}}{L} \rightarrow \acute{\mathbf{r}} = \mathbf{r} + \frac{L}{k}\boldsymbol{\nabla}\phi, \tag{3.2}$$

where k is the wave number and $\boldsymbol{\nabla}\phi$ indicates the transverse gradient in real space. L specifies the distance between the pinhole array and the detector. In eq(3.2) it is assumed that the local phase curvature varies smoothly over the aperture size.

The irradiance modulation therefore is proportional to the phase gradient,

$$I'(\mathbf{r}) = V(\mathbf{r})(1 + \frac{1}{2}\sum_{i=x,y}\exp(\pm ik_i(r_i + \frac{L\partial_i\phi}{k}))). \tag{3.3}$$

The Fourier transform of eq.(3.3) represents the total transverse phase gradients as the argument of the first side lobes of the pattern; the noted feature that exploits the feasibility of the Fourier demodulation method to determine the general phase slopes. The transformed intensity pattern of eq.(3.3) consists of convolution of a slowly varying function with laterally shifted Dirac's delta functions as following :

$$\hat{I} = \frac{1}{2}\{\hat{V} + \hat{b_x} * \delta(q_x - k_x) + \hat{b_y} * \delta(q_y - k_y) + C.C\}, \tag{3.4}$$

where $\hat{b_i}$ are the Fourier transforms of $V(\mathbf{r}).\exp(i\frac{L\partial_i\phi}{k})$. q_i s are the transverse coordinates in the Fourier domain. * indicates the convolution and ˆ denotes the Fourier transform.

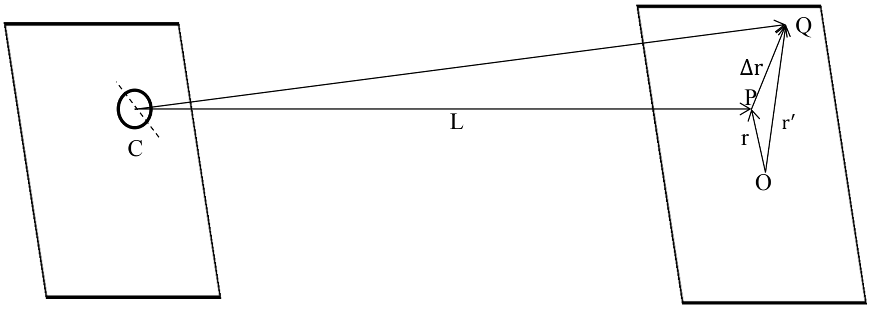

Figure 3.3: Geometrical interpretation of the gradient translation. The local phase variation over C (an arbitrary pinhole) displaces the primary diffracted spot from P to Q at the detector. Thus the new spot position is related to the previous one by $\Delta\mathbf{r}$. $\mathbf{O}$ represents the center of the detector coordinates.

C.C abbreviates the complex conjugate of the right hand side terms.

$V(\mathbf{r})$ varies slowly and thus $\hat{V}$ is localized in the Fourier domain. The reconstruction process proceeds in 2 steps as follows:

1- The first term in eq.(3.4) is explicitly the Fourier transform of the intensity pattern. According to the Nyquist theorem if the diffraction pattern is sampled enough at a frequency smaller than half of the inner maximum frequency, the intensity pattern can be fully reconstructed without losing information. However, using the Hartmann wavefront sensing method, the limited pitch size constrains the modulated frequency of the pattern that results in a lack of resolution. A circular filter surrounding the central peak with a radius equal to half of k_i satisfies the Nyquist frequency requirement as well as bypassing the effects of other side lobes. The inverse Fourier transform of sampled $\hat{V}$ outputs the integrated intensity, illuminating the pinhole array.

2- The last terms in eq.(3.4) are shifted in Fourier space by k_i. It is noted that in this step the pattern has to be sampled, as mentioned previously. Translation of the Fourier pattern can be performed easily using the convolution of I' with a shift factor as following :

$$\mathcal{F}(I' \exp(ik_i.x_i)) = \int I' \exp(ik_i.x_i) \exp(iq_i.r_i) dx_i = \hat{I}(q_i + k_i). \tag{3.5}$$

Here also the central low pass filter suppress the effect of higher harmonics in Fourier space.

To integrate the phase slopes, we used the complex derivative operator as mentioned in[44, 43]. Let us define $\blacktriangle$:

$$\blacktriangle = \partial_x + i\partial_y. \tag{3.6}$$

Thus one can express a complex 2D function f(r) by its transverse partial derivatives as follows :

$$\blacktriangle\mathcal{F} = \int \blacktriangle f(r)\exp(iq_i.r_i)d^2r = -\int f(r)\blacktriangle\exp(iq_i.r_i)d^2r =$$
$$-\int f(r)(iq_x - q_y)\exp(iq_i.r_i)d^2r \Rightarrow$$
$$f(r) = -\mathcal{F}^{-1}(\frac{\mathcal{F}(\blacktriangle f(r))}{iq_x - q_y})$$
$$f(r) = -\mathcal{F}^{-1}(\frac{\partial_x f(r) + i\partial_y f(r)}{iq_x - q_y}). \quad (3.7)$$

The phase of a complex wave field is a real function therefore, it is represented as the real part of (3.7) using the obtained lateral derivatives as;

$$\phi(r) = -\mathcal{R}(\mathcal{F}^{-1}(\frac{\partial_x\phi(r) + i\partial_y\phi(r)}{iq_x - q_y})). \quad (3.8)$$

Here $\mathcal{R}$ represents the real part. The denominator of (3.8) has a singularity at the origin, a so called ill-posed problem. Tikhonov regularization is commonly used to renormalized the singularity[81]. The last inverse Fourier transform is a Cauchy principal value integral, choosing a compact support in the real coordinate which passes the singularity. Thus, the value of the integral is set to zero at the origin where $\mathbf{q}_\perp = (0, 0)$.

Given the Shannon sampling theorem, a 2D raster scan with a step of half pitch size can increase the sampling of the entire wave field at the position of plate (e.g. the wave field is scanned with a known step size similar to the ptychography approaches). However, it is no longer applicable for the purpose of single-shot wave field characterization, and may only provide an average picture of fluctuating pulses.

In practice, the reconstructed phase may contain aberrations due to the imperfectness of the optical system. An aberration may even be the dominant term of the reconstructed phases in an ensemble study, and may obscure the phase fluctuations from being monitored precisely. A straightforward approach is to separate the overall aberration by finding an appropriate model, and describing the aberrated phase within a defined boundary. As seen in fig(3.2.b), the transmitted pattern of the wave field can be defined within a circular boundary which enables to describe the phase of the wave field by using the Zernike Polynomials.

3.2.1 Zernike polynomials

A real optical imaging system does not produce an ideal image because it may not be perfect. In the context of optics, a departure of the performance of an optical system from prediction of ideal paraxial optics is called an aberration[62]. A formed image (here we refer to the phase of a complex wave field) may suffer from several aberrations such as spherical aberration,astigmatism,coma etc. A circular phase profile associated with aberrations can be mathematically modeled using *Zernike Polynomials*[82, 83]. Zernike polynomials are a complete set of orthonormal functions which meaningfully and systematically describe optical phase aberrations. The properties of the orthogonal functions has been described in detail in Chap.2.

Consider an optical system defined within a circular boundary of radius D. Let (r, θ) the polar coordinate of a point within the closed boundary. Let $\rho = \frac{r}{D}$ such that $0 \leq \rho \leq 1$. The wave aberration function A(ρ, θ) of the system can be expanded in terms of a complete set of Zernike circular polynomials, $Z_n^m = R_n^m(\rho).sin\theta$ and $Z_n^m = R_n^m(\rho).cos\theta$, as shown in fig.(3.4),which are spanning the spatial space as a set of orthogonal basis,

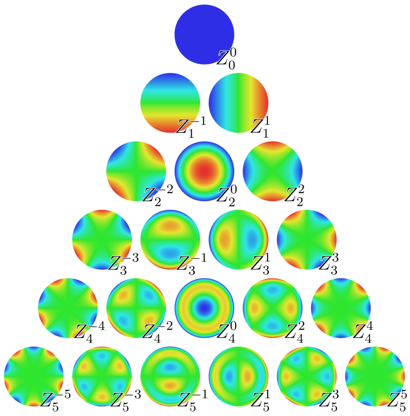

Figure 3.4: The first 21 Zernike polynomials, ordered vertically by radial degree and horizontally by azimuthal degree.

$$A(\rho, \theta) = \sum_{n=0}^{\infty} \sum_{m=0}^{n} [2.\frac{n+1}{1+\delta_{m0}}]^{\frac{1}{2}}.R_n^m(\rho).(a_{nm}.cosm\theta + b_{nm}.sinm\theta), \tag{3.9}$$

where a_{nm} and b_{nm} are the aberration coefficients, m and n are positive integers including zero such that n-m$\geq$0, δ_{nm} is a Kronecker delta and

$$R_n^m(\rho) = \sum_{l=0}^{(n-m)/2} \frac{(-1)^l.(n-l)!}{l!.(\frac{n+m}{2} - s)!.(\frac{n-m}{2} - s)!} \rho^{n-2.l}, \tag{3.10}$$

is a polynomial of degree n in ρ.

The index n represents the radial degree and m is called the azimuthal frequency. The orthogonality in the radial and azimuthal parts are presented as follows,

1. $\int_0^1 R_n^m(\rho) R_{n'}^m(\rho)\rho d\rho = \frac{1}{2.(n+1)}.\delta_{nn'}$,
2. $\int_0^{2\pi} cos(m\theta).cos(m'\theta) = \pi.(1+\delta_{m0}).\delta_{mm'}$,
3. $\int_0^{2\pi} sin(m\theta).sin(m'\theta) = \delta_{mm'}$.

Note that the ordering of Zernike polynomials does not necessarily imply that the aberration coefficients decrease as n increases.

Utilizing the Zernike polynomials, one can recognize the dominant aberrations associated with the reconstructed phases and subtract them from an ensemble of phase reconstruction. Thus, the phase fluctuations within different data sets can be observed accurately.

The theoretical background described in the previous sections, and the knowledge of aberration modeling pave the way for the analysis of collected data using Fourier demodulation as follows in the proceeding sections.

3.3 Experiment

As earlier discussed, this thesis addresses an extension of Fresnel coherent diffraction imaging to characterize highly focused x-ray pulses on a single-shot basis. Since the European XFEL has only just come online in 2017, the approaches described in this thesis were established to be compatible with the FLASH's (the Free electron LaSer in Hamburg) capabilities, as it shares many similarities with the European XFEL. For example, the FLASH 1 facility provides flexible regimes of radiation by altering the radiation parameters, such as the number of active undulators and different electron bunch compression regimes[40]. The former affects the signal-to-noise (SNR) ratio of pulses delivered, and the latter influences the coherence degree associated with pulses[84]. Additionally, both parameters may result in different levels of beam instability, as well as observing chaotic variations of the intensity and phase patterns. All of those parameters (so-called source related variations) are considered as the key issues linked to data interpretation of Fresnel coherent diffraction imaging experiments[13].

At the FLASH beamline BL2, conventionally the Hartmann wavefront sensing method is used as a well-established method to characterize soft x-ray pulses. Therefore, it was possible to propose an x-ray microscopy setup which can benefit from both Hartmann wavefront sensing and imaging methods. Thus, the results of the imaging approach can be compared with the Hartmann wavefront sensing method to illustrate the feasibility of the imaging approach and to benchmark it against the Hartmann wavefront sensing method. Here, we describe the general scheme of both experiments and focus on the Hartmann wavefront sensing branch for the sake of data interpretation and systematical analysis.

A schematic of the setup, as well as the experimental realization at BL2 are depicted in fig(3.5). X-ray of wavelength 14.7 nm are cropped by an aperture, located in a finite distance downstream of the source, and then focused by an elliptical mirror with a nominal focal length of 2 m.

Hartmann Sensors were placed downstream of the ellipsoidal mirror at position A, taking advantage of filters incorporated into BL2 beamline, and additionally into the wavefront sensor, and at position B where an Au mirror under 45^o incident angle guides the focused beam into the Hartmann wavefront sensing branch, as well as the Andor camera, allocated for the imaging experiments (to be explained in the next chapter). A niobium(Nb-384.8nm) filter and a couple of zirconium filters(Zr - 289nm,191.5nm) transmit only the fundamental wavelength and effectively block the third and fifth harmonics

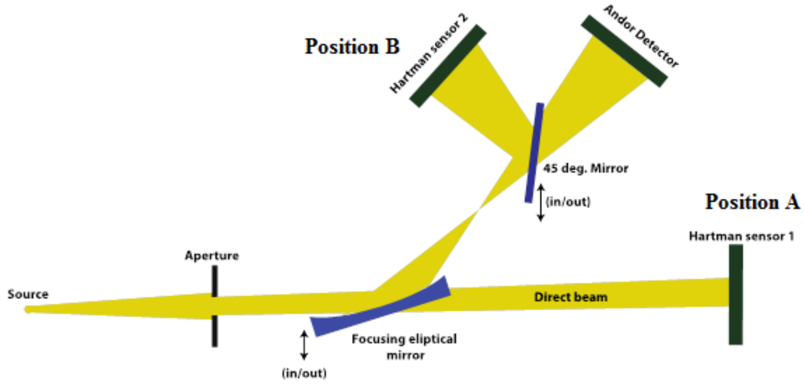

Figure 3.5: Experimental setup. The source radiation passes through an aperture and is focused by an ellipsoidal mirror with 2m nominal focal length. Hartmann sensors are placed at 2 different positions;(A) is illuminated by the direct beam and (B) by the focused beam using an Au mirror under 45^o incident angle. Note that Andor detector was allocated to perform Fresnel coherent diffraction imaging experiments.

which carry less than 1% of the fundamental intensity prior to filtering. The sensor's positions are chosen such that the beam illuminates a sufficient number of pinholes. The data acquisition is performed using the different apertures upstream of the ellipsoidal mirror. As previously mentioned, the experiments were conducted for the different source parameters; the weak and strong electron bunch compression regimes and the different gain length(operating various insertion sections or undulators). The longitudinal bunch compression can be described as follows,

"High peak currents are needed in extreme-ultraviolet and X-ray free-electron lasers. These cannot be produced directly by the electron gun. Therefore moderately long bunches with a low peak are created in the source, quickly accelerated to higher energy and then compressed in length by few orders of magnitude" [40]. The effect of different bunch compression modes and undulator segments on delivered wave fields will be studied by performing statistical analysis over variations in these parameters in the result section.

The Hartmann sensors were designed by Laser-Laboratorium Göttingen e.V. [85] to operate from 10 to 40 nm, which is within the accessible FLASH wavelength range fig(3.6). The Hartmann sensors are adjustable both laterally and with respect to tip and tilt. The translation range is $\pm$10mm [86]. The characteristics features of both Hartmann sensors are drawn in Table(3.1).

A typical intensity distribution from Hartmann sensor A is shown in fig.(3.7). The smooth diffraction distribution around the intense peaks demonstrates the Airy pattern of the pinholes in the near field regime. As seen, the information available for the retrieval process is limited to a few diffraction points.

Table 3.1: **Overview of the Hartmann sensors at FLASH BL2**

	Camera	Hartmann Plate
HS A	Softhard SHT MR285MC 1392(H) x 1040(V) pixels 8.98mm(H) x 6.71mm(V) field of view	hole diameter 75μm pitch size 250μm 198.251mm plate to CCD
HS B	Princeton Instruments PI-SX: 1300 1340(H) x 1300(V) pixels 19.5mm(H) x 19.5mm(V) field of view	quadratic holes 110μm x 110μm pitch size 250μm 250mm plate to CCD

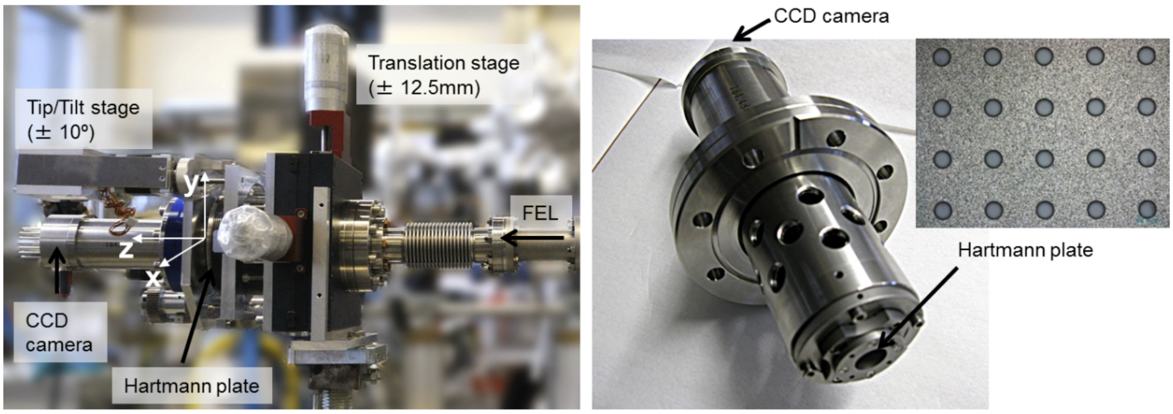

Figure 3.6: Left panel: Compact design of the modified Hartmann sensor with enhanced mechanical stability and motorized movement. Right panel: The instrument has capability of operating different Hartmann plates. For instance a elctro-formed pinhole array(magnification 10X) is shown as inset [86].

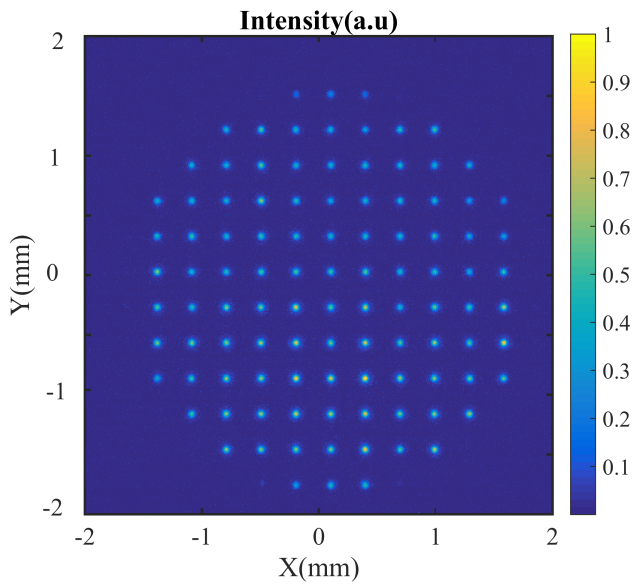

Figure 3.7: A typical spot pattern measured at the detector behind a Hartmann plate. This data frame was measured using HS-B,1064.5mm downstream of the ellipsoidal mirror, at wavelength 14.7nm and the weak compression regime with 30 electron bunches and 6 active undulators. Colorbar indicates the intensity in a normalized unit.

3.4 Simulation

To investigate the procedure of phase retrieval using the Fourier demodulation, as theoretically stated in sec.2.2, a series of wave field measurements were simulated. Here the Hartman sensor consists a 40 x 40 pinhole array, with 100μm hole diameter and 400μm pitch size, and is mounted 300mm upstream of the detector with 1340 x 1340 pixel, each 20μm x 20μm. A fluctuating field **E** with a certain level of the Poison noise illuminates partially the pinhole array, as shown in fig.(3.8), and the diffracted wave propagates to the detector by the near field Fresnel propagator,

$$\psi(r_\perp, L) \simeq exp(iqL)\mathcal{F}^{-1}(exp(-iL\frac{q_\perp^2}{2q})\ F\ \psi(r_\perp, 0))\,. \tag{3.11}$$

Here $\psi(r_\perp, 0)$ is the wavefront after the pinhole array, L is the pinhole to detector distance, q is the wave number. $\perp$ indicates the transverse coordinates of Fourier space.

Therefore, the wave field intensity (I$'$) at the detector is $\psi(r_\perp, L).\psi^*(r_\perp, L)$. Following the phase retrieval procedure, according to eq(3.4), at the next stage $\hat{I}$ is calculated. The central and first side lobes in each lateral direction are selected as illustrated in fig.3.9. The inverse Fourier transform of the side lobes demonstrates the phase gradient in each lateral direction as $V(\mathbf{r}).\exp(i\frac{L\partial_i\phi}{k})$. The obtained phase derivatives in this method are the argument of an exponential function, and may be wrapped. A wrapped phase

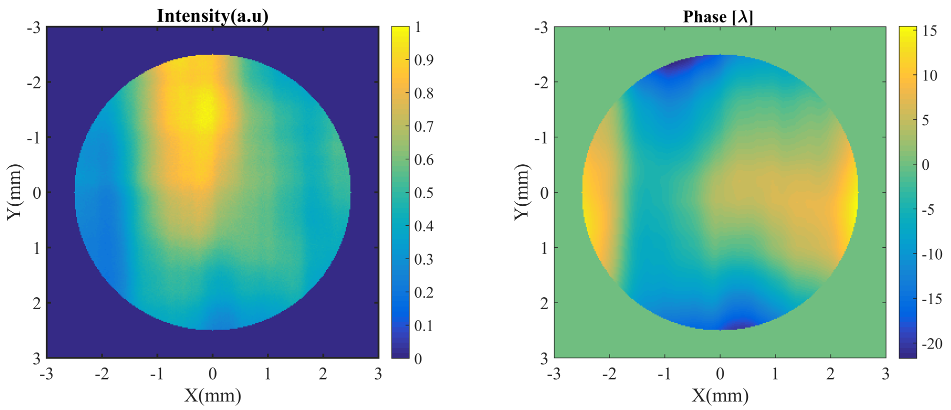

(a) (b)

Figure 3.8: (a) and (b) are the intensity and phase components of the complex wave field, illuminating the pinhole array. As seen, the intensity consists of a low flux distribution that is expected for some of the operational configurations. The centroid method requires either intense pulses, or an averaging over a few low intensity pulses to retrieve phase, otherwise the centroid locations are not distinct.

means that all phase points are constrained to their principal values in a range $[0,2\pi]$ or equivalently, $[-\pi,\pi]$. For example, $\exp(i\frac{L\partial_i\phi}{k})$ is a multi-valued complex exponential function and has a series of branches, repeating by a factor 2π (see fig.(3.10)).

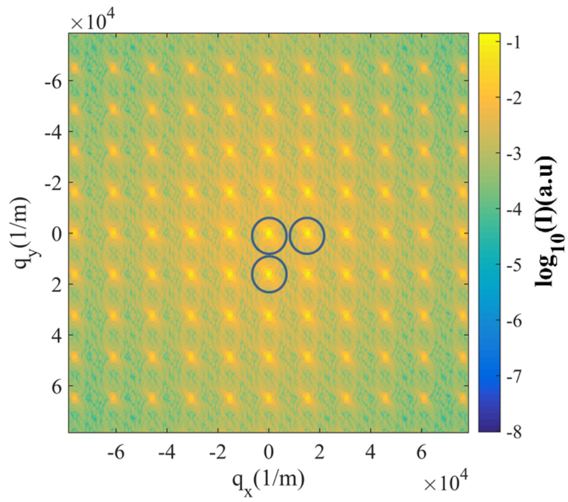

Figure 3.9: Fourier transform of the measured intensity at the detector plane. The localized distributed carrier harmonics are apparent in Fourier space. The circled lobes (the central and first transverse) carry on the complex wave field information. The low pass filters are indicated by blue circles. The colorbar represents the intensity on a logarithmic scale in an arbitrary unit.

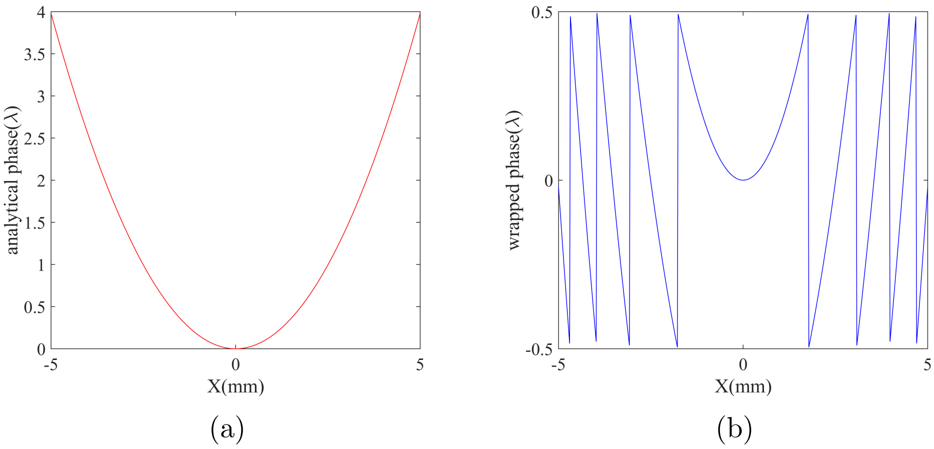

Figure 3.10: The (a) analytical phase and the (b) wrapped phase profiles of a 2D spherical phase. When the phase exceeds more than $|\frac{n}{2}\lambda|$, the wrapped edges can repetitively be seen in (b).

The easiest way to unwrap the phase can be summing the phase differences sampled at a discrete location. This method suffices as long as the differences does not jump larger than 2π. Otherwise, a more complex algorithm has to be implemented to deal with the circumstances in which this condition does not apply[87]. Here, 2D version of the 3D unwrapping algorithm described in[88] has been used. The approach starts to unwrap a function within a defined boundary such that the function is zero-valued outside of the boundary. Thus, the algorithm divides the area covered by the boundary to small region-of-interest (ROIs), and tries to unwrap the function locally. Therefore, the unwrapping procedure requires a well-defined boundary to be calculated. A straightforward solution was found using retrieved intensity. A binary mask is defined such that the intensity levels less than 15% of the maximum flux are set to zero. Thus, the high-frequency distributions are excluded from analysis, which is a limit to the resolution obtained from the Hartmann wavefront sensing method, alongside of the pitch size fabrication as a practical issue to affect the resolution.

The retrieved complex wave field is shown in fig(3.11).

To understand the accuracy of a wave field retrieval by Fourier demodulation method, we define two measures indicating the differences between the simulated and reconstructed wave fields. The first measure is a pairwise correlation between the intensities (simulated and reconstructed) and phases as well. The correlation shows how accurate the general map of the intensity or phase is reconstructed. The second measure is defined as the P-V error ratio to quantify the resolution of the reconstructed phase.

Thus, for the given wave field, the first measure yields

$$e = \left(\frac{(P-V)_{simulation} - (P-V)_{reconstruction}}{(P-V)_{simulation}}\right) * 100\% = 10\%, \tag{3.12}$$

which demonstrates that phase structure has not been well-determined.

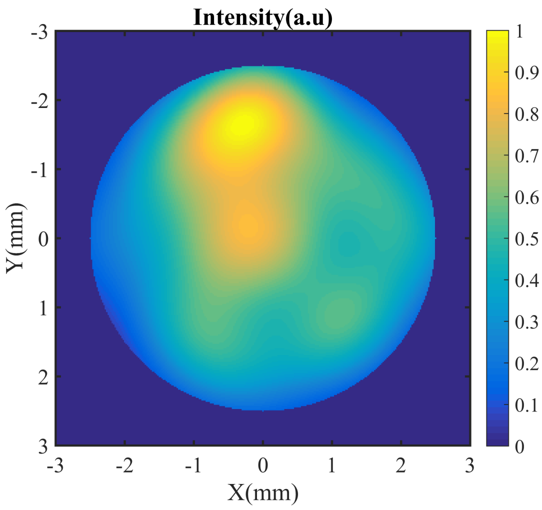

(a)

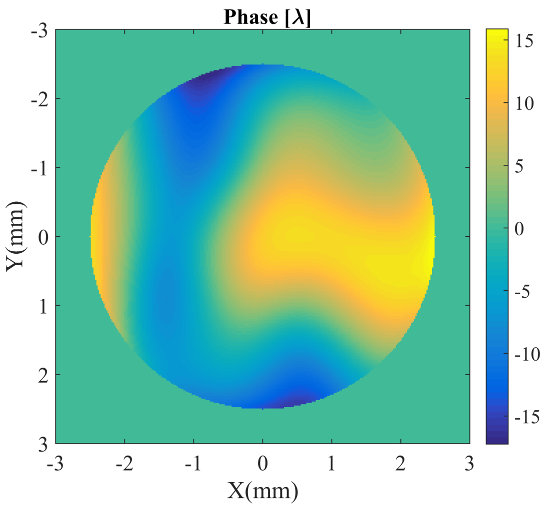

(b)

Figure 3.11: The reconstruction of the simulated complex wave field (fig.3.8) using the Fourier demodulation method. The phase and intensity are retrieved by using 100 diffraction spots. The recovered intensity approximately determines the illuminating field distribution before the pinhole array (a). (b) displays that the general phase map is successfully reconstructed, however the smaller structures have not been retrieved due to the limited resolution, as predicted.

The reconstructed intensity correlates reasonably with the simulation in a factor of 0.95%. As seen, the reconstructed intensity distribution also has not been completely resolved. The reconstructed wave field can be described as a blurred version of the simulated wave field due to the limited-resolution of the Hartmann wavefront sensing method. Nevertheless, the results of the Hartmann wavefront sensing method can be used to quantitatively measure significant shot-to-shot phase and intensity fluctuations which are observable with the resolution of the system.

3.5 Result

Different ensembles of measured data for different source parameters, as listed in table(3.2), were analyzed for different apertures(10, 5, 3 mm diameter) upstream of the ellipsoidal mirror.

Table 3.2: **Different source setting,considered for the complex wavefront retrieval using the Fourier demodulation method.**

Case	Compression regime	Number of Undulators	Wavelength(nm)	Measurement
A1	weak	4	14.7	A
A2	weak	6	14.7	B
A3	strong	4	14.7	A
A4	strong	6	14.7	B

For each data set, an ensemble of dark images, without beam or the aperture in the beamline, was measured. Then, the averaged dark image was subtracted from each frame of data within the data set to account for noise distributions. The background subtracted diffraction patterns were converted in Fourier space. For each data frame, the Fourier demodulation algorithm identified the central and first side lobes. As such, the intensity and the lateral phase gradients were retrieved from the Fourier space patterns. Since the phase gradients were wrapped, a binary mask was defined to initialize the unwrapping algorithm. The mask has zero values for the intensity levels less than 10% and is 1 elsewhere. It was observed that the masks form a circular boundary around the reconstructed intensity for either intense pulses (6 active undulators) or pulses with lower signal levels (4 active undulators).

To illustrate the reconstruction of pulses measured, we show a series of the reconstructed phase and intensity for the different radiation regimes, when a 5 mm aperture was used (fig3.12). The data shown yielded the lowest value of P-V among 100 frames within a data set (A1-A4). Also, the shown reconstructed phases are aberration corrected by subtracting the first 7 Zernike polynomials (Eq(3.11)), as the dominant components of aberration. By fitting the Zernike polynomials to the reconstructed phases of different radiation regimes, we observed that the further coefficients of the Zernike polynomials (8 and higher) are negligible. Therefore, the first 7 aberration polynomials were selected to describe the systematic aberration of the optical system.

Every data set consisted of 100 frames of measured diffraction patterns. Since FEL's properties may change shot-to-shot, therefore the measured properties associated with the intensity and phase is required to be observed statistically. Thus, we would obtain an average value for each complex wave field property illustrating a statistical picture of a dynamic source. Intuitively, increasing the ensembles of measured pulses would result in a more accurate conclusion about the source's systematic fluctuations. Nevertheless, the amount of data frame acquired by the FLASH experiment resulted in observing the determined parameters fitting well with previous works done[86].

Table(3.3) specifies the reconstruction's parameters obtained for the different ensembles of measured data versus each source setting. It is seen that the weak compression regime possesses a higher beam positional stability, especially in the horizontal direction. In addition, the average RMS error and positional fluctuation of A4 demonstrates that the strong compression regime with a longer insertion section radiates more chaotically in comparison with the other cases. And also, It is observed that 6 undulators setup significantly increase the noise distribution. This effect manifests itself when a diffraction pattern is transfered to Fourier space, as a decrease of the signal-to-noise ratio in the side lobes. Additionally, during the strong compression regime we expected to observe less stable pulse radiation compare to the weak compression, however the results show that even a weak compression may exhibit significant shot-to-shot fluctuations of the intensity. We observed that the combination used in A3-A4 dramatically change the intensity shot-to-shot fluctuations compared to a combination of weak compression and different undulator number.

Furthermore, radiation simulations have shown that for the same geometry given (a 5mm aperture here) one expects to measure pulses with 85% degree of transverse coherence in the weak compression regime with 4 active undulator segments and 75% in the strong compression. Since the Hartmann wavefront sensing method is not sensitive to the coherence degree of the pulse, there is no more precise measure to distinguish the coherent and partially coherent pulses except the results of radiation simulations. Therefore, to categorize the measured pulses in terms of coherence, the simulated analyzed value will be considered hereafter in this chapter. It will be shown in the next chapter that the imaging approach and its algorithmic structure well categorizes the measured pulses with respect to their coherence properties.

Table 3.3: **The reconstructed wave field parameters for the different ensembles of pulses via different source parameters.<> indicates an ensemble average.**

Case	<Phase P-V>(λ)	<Phase RMS error> (λ)	Standard deviation of the beam position (mm)
A1	1.47	0.067	$\sigma_x = 0.088$ - $\sigma_y = 0.590$
A2	1.11	0.065	$\sigma_x = 0.034$ - $\sigma_y = 0.198$
A3	1.53	0.062	$\sigma_x = 0.407$ - $\sigma_y = 0.502$
A4	1.84	0.095	$\sigma_x = 0.812$ - $\sigma_y = 0.666$

For coherent radiation, it is possible, and relatively straightforward, to numerically back propagate the reconstructed wave field from the sensor to the focus of the elliptical mirror. Theoretically, A1 and A2 radiation regimes radiate coherently enough which

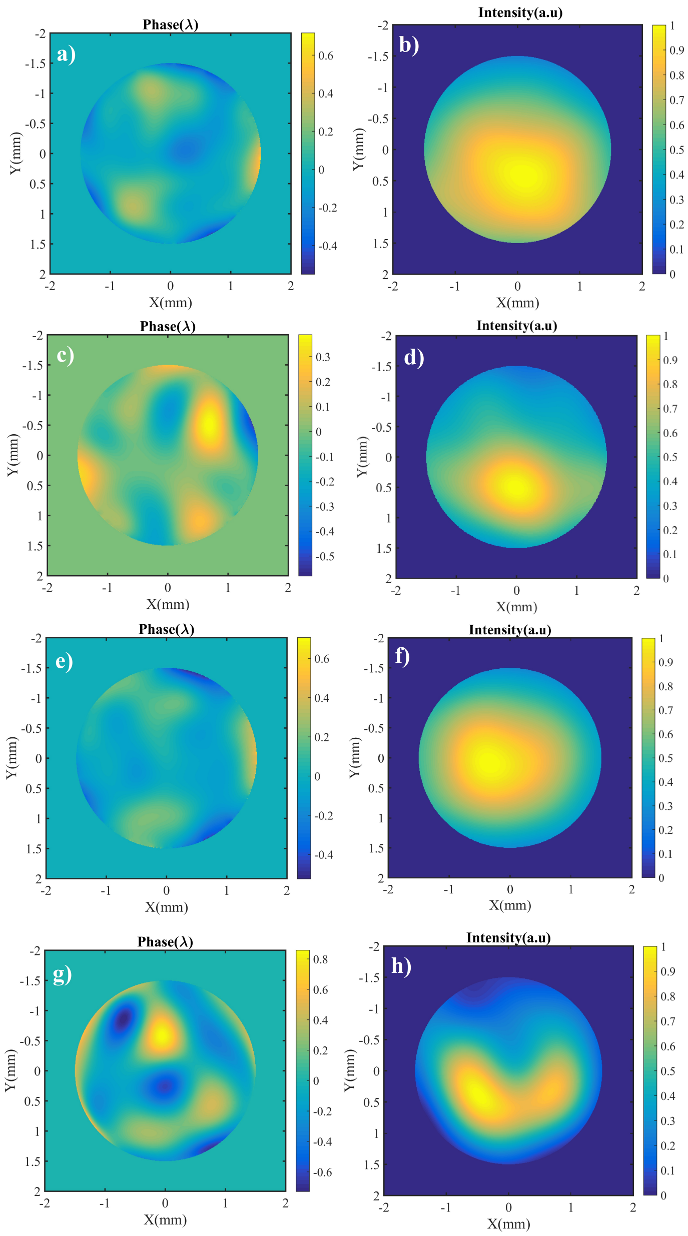

Figure 3.12: The reconstructed data of the Hartmann wavefront sensor B, focused X-ray pulses of 14.7 nm wavelength, and a 5 mm aperture upstream of the elliptical mirror. Each row represents the components of reconstructed wave fields (the intensity and aberration-free phase) for A1 to A4 regimes. As seen, the Fourier demodulation method is successfully applied to reconstruct pulses with the different signal-to-noise and coherence degree. For a 5 mm aperture size approximately 25 diffraction spot were measured for each single-shot. The data shown yielded the lowest P-V among 100 frames of the measured data for each radiation regime indicating in table(3.2).

enable us to back propagate the reconstructed wave field, and determine the complex wave field at the *image plane*. The image plane specifies where the source is imaged, which needs not to be the focal plane of the elliptical mirror[47]. This plane can be considered as the Fourier transform plane of the ellipsoidal mirror performing transform, and located slightly downstream of the nominal focal length. Thus, ray-optics governs that all reflecting rays from the ellipsoidal mirror are collected at the image plane (i.e. the focus of the beam). Therefore, the intensity distribution is highly localized at that plane and the sharpness[89],

$$S(z) = \iint I^2(x, y; z)\, d^2r\,, \tag{3.13}$$

reaches its maximum value.

Numerically, the retrieved wave field at the detector back propagates to the nominal focal plane of mirror, and eq(2.32) and eq(2.45) are utilized to propagate the new wave field in a neighborhood of the mirror focus. Measuring an ensemble of wave fields, eq(3.13) demonstrates the location of the image plane, as shown fig(3.13). Since the variation of the image plane would be observed statistically for a shot-to-shot pulse characterization experiment, we would describe the position of the image plane as a mean value and its standard deviation.

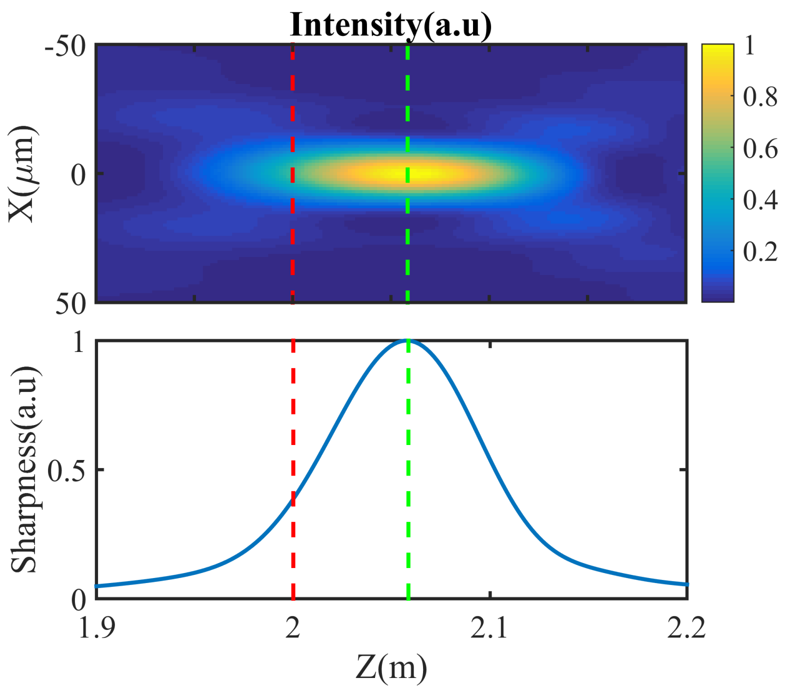

Figure 3.13: The image and focal planes are indicated by the green and red lines respectively. As seen, the normalized sharpness reaches the unity when the intensity is highly localized, illustrating the image plane.

In fig.(3.14) three different meridional intensity distributions, of pulses yielding the minimum beam positional instability within the data sets, versus different aperture sizes for A2 radiation regime are shown. The 1D line profile of the image planes (a scan in direction of the white lines) show a central peak with different fringe distributions related to the aperture size and the coherence degree of pulses. Also, the non-uniform distribution of the high frequency fringes, for 3 mm and 5 mm aperture sizes, are due to the stochastic intensity distribution of the pulses illuminating the aperture, otherwise a smooth fringe distribution at higher frequencies would be observed. For 10 mm aperture size, the high frequency features appear uniformly since the area covered by aperture might be larger than the spatial coherence length of the pulses. Therefore, the transition from fully to highly coherent radiation is observed. Additionally, The FWHMs of the peaks determined by the 1D profiles cover an area with only a few numerical pixels (approximately 6 pixels) that manifests a resolution limited picture of the image plane. So forth, those positional fluctuations, in the lateral direction, of the pulses that are smaller than the resolution limit may not be resolved completely.

Fig.(3.15) shows the reconstructed wave field at image plane of a pulse shown in fig.(3.14.c). The lateral line profiles through the center illustrate a slightly different fringe distributions can be attributed to the stochastic intensity distribution of wave field illuminating the aperture. The center of mass of the image plane intensity distribution was found in (0,0) with a standard deviation of $\pm$ 1.5μm in both lateral directions. The determined lateral displacements of the image plane for the different data set of different radiation regimes were always smaller than the resolution element (lateral pixel size), so the lateral displacements can not be meaningfully observed by the limited resolution of the Hartmann wavefront sensing approach.

Since, the determined intensity distribution of the pulses at the image plane are more structured than a simple Gaussian distribution, especially when a 3 mm aperture sized used, the beam width at image plane can not be perfectly described by a Gaussian fitting to the 2D intensity distributions. Therefore, as a conventional method in laser optics we determine the FWHM of pulses at image plane utilizing the 2^{nd} momentum method[64]. In this approach, the second momentum of the intensity in a pixel-wise system within the numerical array is calculated as follows:

$$4\sigma = 4. < r_i^2 >= 4.\frac{\iint (r_i - \bar{r_i})^2 \, I(x,y) \, d^2r}{\iint I(x,y) \, d^2r}, \tag{3.14}$$

where i indicates (x,y). The wings of the beam profile influence the 4σ value more than the center of the profile since the wings are weighted by the square of its distance, r^2, from the center of the beam. Then, the FWHM is related to 4σ as 68% of its value,

$$FWHM = \sqrt{\frac{\ln 2}{2}} \, . \, 4\sigma. \tag{3.15}$$

Theoretically, when a coherent and nearly planar pulse illuminates a finite size focusing optics the diffraction limited spot size (FWHM of intensity) can be calculated as[47],

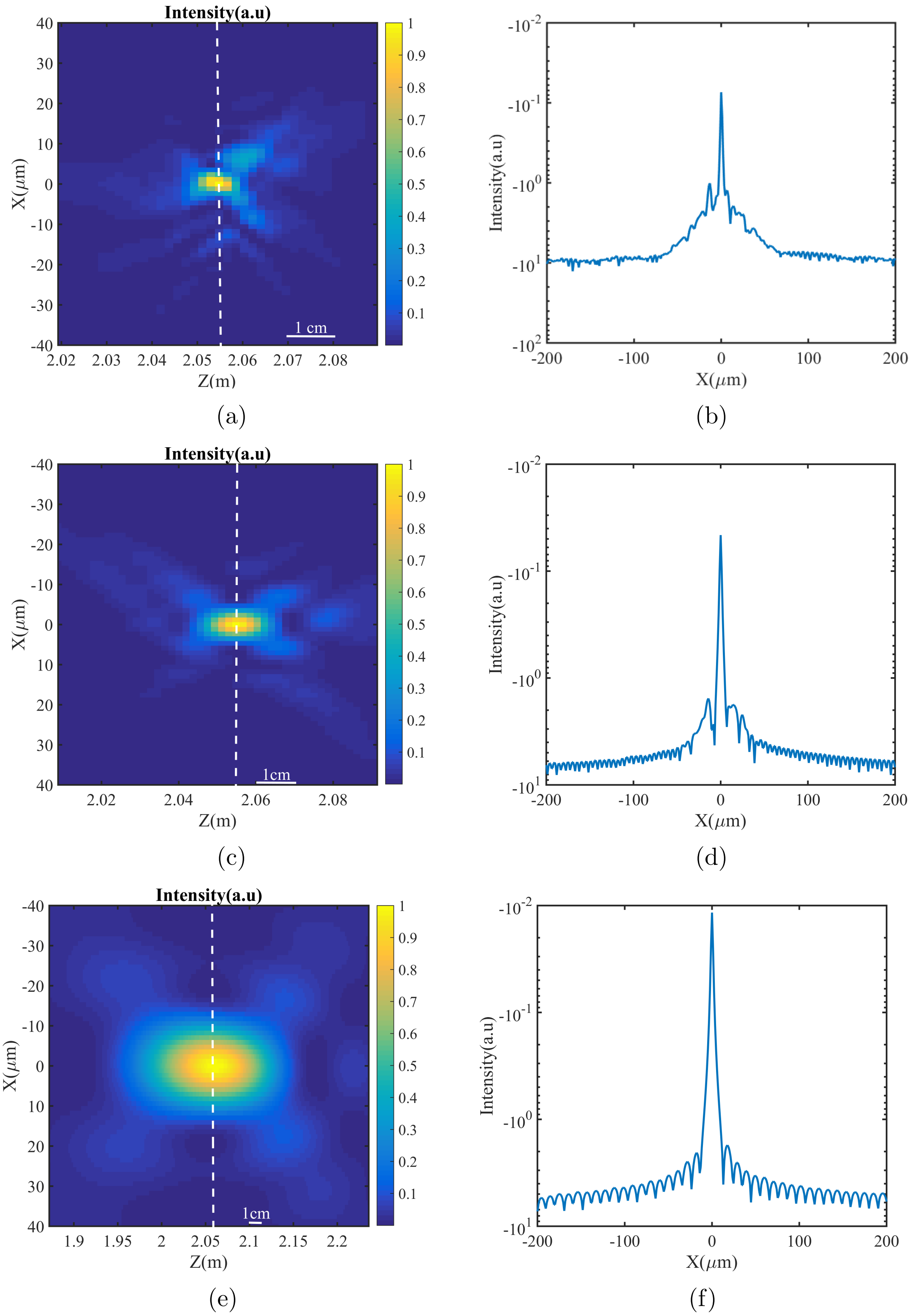

Figure 3.14: (a,c,e) show the meridional profiles of the reconstructed wave fields versus the different aperture sizes (3, 5, 10 mm). The dashed lines indicate the beam waist position in each case. (b,d,f) present the cross sectional field distribution at the waist position.

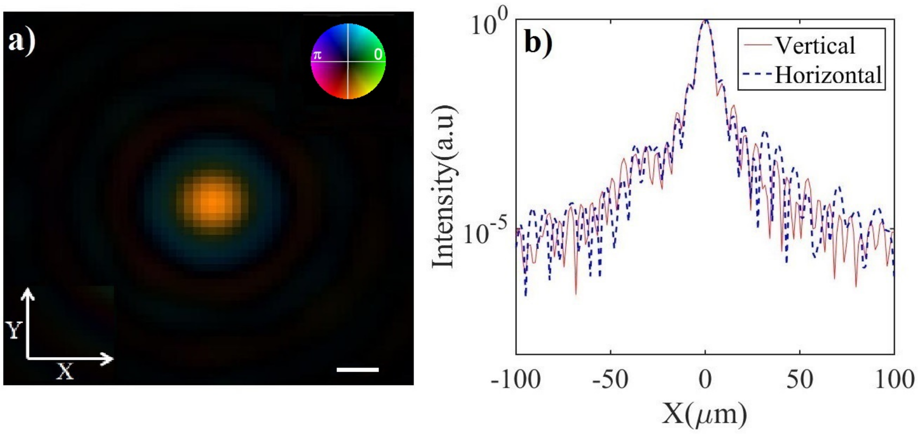

Figure 3.15: The Hartmann wavefront sensing reconstructed complex wave field in the image plane of a pulse having the same longitudinal position as indicated in fig.(3.14-c). In (a) phase is expressed by the hue and intensity by the brightness. (b) displays the lateral line profiles of the intensity at the image plane. The FWHM was estimated as $9.63_v \times 9.63_h \mu m^2$. The solid white line is a $20\mu m$ scale bar.

$$FWHM = 1.03\,\frac{\lambda\, z_{image}}{D}, \tag{3.16}$$

where z_{image} is the image plane on-axis position and D is the diameter of the aperture.

In Table(3.4) the average of FWHMs, determined over 100 pulses of A2 regime using 3,5,10 mm apertures, and expected diffraction spot size values (FWHM of intensity), by assuming a plane wave radiation, at the image plane are compared. The calculated FWHMs in all cases are larger than the theoretically expected diffraction spot sizes. The discrepancy can be attributed to the divergence of the beam illuminating the aperture (a non-planar phase curvature of the pulses) and non-uniform intensity distribution within the aperture regardless of the aperture size. Therefore, the assumption of a plane wave illumination is not longer valid here, illustrating the effect of short beamlines into the focus properties. For hard x-ray pulses, since the distance between the source and the focusing optics is typically a few thousands of meters, the phase curvature of the pulses illuminating the focusing optics would not strongly affect the spatial distribution of the focused wave at image plane, and the FWHM is expected to correlate with the diffraction spot size of optics.

3.6 Summary and Conclusion

In this chapter, the experimental realization and theoretical considerations for applying the Hartmann wavefront sensing to characterize single-shot highly focused pulses at the FLASH beamline BL2 has been discussed.

The possibility of using the Fourier demodulation method to retrieve the complex

Table 3.4: **Comparison of the average FWHMs at the image plane over 100 pulses of A2 regime and theoretically calculated diffraction spot size values, versus different aperture sizes.**

aperture size(mm)	Measured FWHM(μm)	Diffraction limited spot size(μm)
10	6.71 ± 1.47	3.11
5	9.51 ± 0.18	6.22
3	17.86 ± 0.17	10.38

wave fields of many patterns measured with Hartmann arrays has been introduced. In this method, the measured patterns are studied in Fourier space, and the information of the phase gradient and intensity are extracted from the central and first side lobes of the converted patterns while the Shannon sampling criterion is satisfied.

The retrieved complex pulses in the coherent regime (i.e. weak electron bunch compression) enabled the determination of the properties of the pulses at the image plane. The lateral beam position variation was not determined, due to the limited resolution of the Hartmann system. A strong shot-to-shot (aberration-corrected) phase variation was observed within the strong compression data sets while the weak compression regime possessed a smoother shot-to-shot variation, to be seen as a well-defined phase mode. The fluctuations (phase and intensity) observed within the pulses of the strong compression regime may be linked to the growth of the strong nonlinear terms[5] in the electron motions which estimates this more statistically shot-to-shot variation as measured.

The probability density function analysis showed the difference between the coherence properties of the weak and strong compression regimes. This effect can be attributed to the change in the RMS bunch length which is directly linked to the uncorrelated energy spread ($\frac{\Delta E}{E}$) of the bunch. When a strong compression is applied, the number of radiation modes increase, as released by the probability analysis, and consequently the contribution of the dominant mode decrease[5].

The caustic distribution of coherent pulses demonstrated a structured intensity distribution at the image plane for 3 and 5 mm aperture sizes, showing that the transverse coherence length of pulses is comparable to the extent of apertures. For 10 mm apertures, the features were significantly smoothed out.

Lastly, it should be noted that utilizing the Hartmann wavefront sensing method at FLASH was enabled due to the use of soft x-ray radiation. This approach may not be possible at a hard x-ray beamline. The Hartmann plates usually are designed to operate in the soft x-ray regime and are transparent when illuminated with hard x-rays . To analyze short wavelength radiation with a Hartman sensor, a longer distance between the plate and the detector is needed to validate the assumption of $\Delta\phi \ll 2\pi$. This requirement may affect the prerequisite of near field distance between the plate and detector, and reduce the accuracy of the analysis. Therefore, the Fresnel coherent diffraction imaging method will be introduced as a potentially applicable approach across a broad range of photon energies to characterize single-shot highly focused pulses in the next chapter. The result of the Fresnel coherent diffraction imaging technique will be compared against the results of the Hartmann wavefront sensing method to assess the meaningful correlations between those methods and to benchmark the iterative method.

CHAPTER 4

Coherent Diffraction Imaging Technique : Background, Simulation and Experiment

Imaging non-crystalline small biological samples at FELs require a high degree of X-ray beam focusing to obtain the highest intensity or an optimal matching between beam size and the spatial extent of samples to be injected [90, 26]. To enable a complete analysis of data for a large fraction of experiments performed at FELs with focused beams, it is important to know the exact properties of the focused complex wave fields including the phase, intensity and spatial distribution. This is particularly the case for imaging experiments which require either a well-defined or well-characterized wave field to quantitatively interpret the structure of the sample investigated.

The characterization of highly focused X-ray pulses is particularly challenging due to the stochastic shot-to-shot fluctuations of the SASE process as well as a focused peak intensity that exceeds the damage threshold of any material[91]. Therefore, an approach is required to understand the variation of specific properties of pulses that furthermore would enable a statistical analysis over various changing parameters– particularly of the FEL source.

Different methods have been developed to characterize FEL pulses either in a single-shot basis or as an average over an ensemble of measured data[92, 14, 25]. Most of those methods suffer from applicability in a limited photon energy range or measuring a large ensemble of overlapped data in the presence of a sample to whether provide an average picture of delivered pulses.

A solution to overcome these problems is to use an iterative diffractive imaging technique[33, 34, 35] applied to single far-field diffraction patterns of a highly focused beam[36]. This method comprises an Iterative Phase Retrieval Algorithm (IPRA) with real space and intensity modulus constraints, utilizing the spherical phase curvature of the focused beam; known as the Fresnel Coherent Diffraction Imaging (FCDI) method[59, 13]. This technique retrieves the phase of the measured far-field diffraction pattern of a finite size focusing optics illuminated by an x-ray source. It has been shown that the Fresnel coherent diffraction imaging algorithms result in a fast and predominantly reliable convergence compared to the conventionally used coherent diffraction imaging algorithms[37, 38].

In this chapter, we propose an extension of the Fresnel coherent diffraction imaging method to systematically characterize highly focused X-ray pulses under more general experimental conditions than previously assumed[36, 93]. The technique can be used to explore both the complex wave field information, as well as the source-point position and its fluctuations. The latter is particularly interesting for short FEL beamlines and yields valuable information about the gain length of the source[5]. The opportunity of using Fresnel coherent diffraction imaging for a high-resolution, highly focused wave field characterization in a single shot basis are discussed in detail. The concepts of phase retrieval algorithms are introduced, and numerical simulations based on the geometry used at the FLASH beamline BL2 are performed to assess the effectiveness of the Fresnel coherent diffraction imaging approach as a function of the signal-to-noise ratio and coherence degree. I discuss the data treatment and analysis of the imaging technique for the measured diffraction patterns of different ensembles. The reconstructed data are compared with Hartmann wavefront sensing measurements as a classical benchmark.

4.1 Iterative Phase Retrieval Algorithm

It was shown that the phase information of a scattered wave field can be fully recovered if the associated diffraction intensity is sampled fully enough at a spacing that is finer than the Nyquist frequency. In 1975, Fienup developed algorithms for retrieving the phase of a 2D Localized Field Distribution (LFD) based on the iterative free-space propagation of the wave field in real and Fourier space, utilizing a priori knowledge of each domain, so-called **Iterative Phase Retrieval Algorithms**[11].

Iterative phase retrieval algorithms can be interpreted as iterative maps onto constraint sets. Assume $\mathbb{Q} \in \mathbb{R}$, then a subspace L$\in \mathbb{Q}$ is a constraint set if its elements obey a certain constraint. For example, the constraint L_1, consisting domain information, can be formulated as:

$$L_1 := \{\psi \in \mathbb{Q} || D_{Fr}(\psi)| = |\tilde{\psi}| = \sqrt{I}\}, \tag{4.1}$$

where D_{Fr} is the Fresnel diffraction integral operator and I is the measured intensity. Additional knowledge about the spatial localization of the wave field can be formulated in another constraint set and is called **Mask** or **Support** in real space(L2). A solution of ψ must fall into the elements of intersection $L' = L_1 \cap L_2$.

If one could map any element of $\mathbb{Q}$ onto an element of L', the solution would obey the given constraints. This mapping operator can be a projection defined as[35],

$$\mathbb{P} := \psi \to D_{Fr}^{-1}\{\sqrt{I}.\frac{\tilde{\psi}}{|\tilde{\psi}|}\}. \tag{4.2}$$

that iteratively sends every point of $\mathbb{Q}$ to the set of nearest points in L'. A solution of projection onto set exists if the euclidean space metric achieved a minimum in $\mathbb{Q}$,

$$\epsilon := min_{\psi\in\mathbb{Q}}||\mathbb{P}(\psi) - \psi||. \tag{4.3}$$

Generally, the phase retrieval problem may involve **incompatibility in the Constraints** or, in mathematical language, **nonconvex constraint sets** due to the noise in the data, highly symmetric geometry or even missing data regions in the diffraction pattern[94]. Thus, the algorithm could stagnate in a local minimum and not approach to eq(4.3).

4.1.1 Gerchberg and Saxton algorithm

The first iterative propagation based algorithm was proposed by Gerchberg and Saxton (GB algorithm) in the imaging community. The aim of the algorithm is to retrieve the phase of a localized field distribution where the amplitude of a wave field in two planes separated by a distance z is known. In this setting the number of independent equations ($2N_P$ for an image with N_P pixels) is equal to the number of independent unknowns ($2N_P$ real and imaginary pixel values). The method uses the Fourier transform relationship for a wave field between a near plane downstream of the localized field distribution and the far-field diffraction plane. These measurements give the amplitude of the wave field at two related positions in space allowing an iterative phase retrieval to be performed. The iterative scheme of the original Gerchberg-Saxton method proceeds as follows.

1. The measured intensities in both planes are transformed to be represented as the modulus of the complex amplitudes of the wave field i.e. $|\psi(\vec{r})| = \sqrt{I}(\vec{r})$
2. The near plane amplitudes are then assigned random phases, as a first guess to their values, and transformed to the diffraction plane in the far-field (Fourier transformed).
3. The calculated phases in the diffraction plane are kept, and the magnitudes of the amplitudes corrected by the measured amplitudes.
4. The estimated diffraction-plane field is transformed back to the image plane where again the amplitudes are corrected by the measurements and the phases are kept.
5. The estimated near-plane field is then transformed to the diffraction plane where the process is again repeated successively correcting the iterated amplitudes with the measured amplitudes until the phases calculated converge on the solution.

The convergence of the algorithm reaches when the Euclidean distance between the current estimate of the wave field's amplitude in the far-field ($\mathbb{P}(\psi_j)$), and the measured intensity (I_F),

$$\epsilon_j^2 = ||\mathbb{P}(\psi_j) - \sqrt{I}_F||^2, \tag{4.4}$$

is minimized such that no further improvements after j^{th} iteration is observed, and ϵ stays at a constant value.

Note, however, that convergence of the algorithm does not generally guarantee that the algorithm has found the correct solution. In other words, there may be many different fixed points which are not the desired solution.

4.1.2 Error Reduction Algorithm

If only one intensity measurement is available and if the object function is characterized by a distortion in phase and amplitude, the Gerchberg-Saxton algorithm is not applicable. With additional constraints in the near plane the problem can still be solved in many cases. The Error Reduction algorithm (ER) is a modification on the Gerchberg-Saxton method where the real space constraints are altered. In the error reduction algorithm the real-space constraint is no longer the amplitude of the wave field, but the finite extent of the real-space amplitude of localized field distribution. This could achieve if the first step of the Grechberg-Saxton algorithm (the amplitude constraint) is altered as,

$$\psi_{j+1}(\vec{r}) = \begin{cases} \psi_j(\vec{r}) & \text{if } \vec{r} \in \mathbb{Q}, \\ 0 & \text{if } \vec{r} \notin \mathbb{Q}. \end{cases}$$

where $\mathbb{Q}$ is the set of points that are within the known finite extent of the localized field distribution.

Just as for the Gerchberg-Saxton algorithm the error ϵ_j ideally decreases monotonically with the number of iterations in the error reduction algorithm, hence the naming of the algorithm.

4.1.3 The Hybrid Input-Output Algorithm

Another modification to the Gerchberg-Saxton algorithm, the Hybrid Input-Output algorithm (HIO) is based on the interpretation of the modulus constraint as a nonlinear system with input ψ_j and output ψ'_j at iteration j. The new iterate ψ_{j+1} is now formed not by (minimally) modifying ψ_j in order to obey the support constraint as it is done in the error reduction algorithm. Instead, ψ_{j+1} is formed as a linear combination of the input and output of the modulus constraint system . Hence, the j th iteration can be formulated as follows:

$$\psi_{j+1}(\vec{r}) = \begin{cases} \psi'_j(\vec{r}) & \text{if } \vec{r} \in \mathbb{Q}, \\ \psi_j - \beta\psi'_j & \text{if } \vec{r} \notin \mathbb{Q}. \end{cases}$$

where $\mathbb{Q}$ is the set of points that are within the known finite extent of the localized field distribution and the damping parameter β satisfies $0 < \beta < 1$ and is commonly taken as about 0.8. This has the effect of damping the regions where the amplitude should converge to zero, and provides the real space constraint that drives the algorithm towards convergence along with the Fourier modulus constraint. This algorithm has met with much success where the Gerchberg-Saxton algorithm has failed to converge and stagnated. This is due to the flexible nature of the real space constraint applied in hybrid input-output algorithm.

In the following sections we introduce the theoretical considerations required to implement a Fresnel coherent diffraction imaging based phase retrieval algorithm for the single-shot x-ray wave field determination. The error reduction algorithm is used as the main body of the phase retrieval algorithm introduced in this chapter.

4.1.4 Highly Focused FEL Phase Retrieval Algorithm

Consider the problem of imaging highly focused FEL pulses. Experimental schemes to do so can be proposed as depicted in fig(4.1). The apertures A and B introduce two different setups that enable the performance of single-shot focused x-ray wave field characterization based on the Fresnel coherent diffraction imaging concept to utilize the phase curvature of a divergent beam into the phase retrieval algorithms. The focusing optics may consist of a Fresnel Zone Plate (FZP), and an order sorting aperture (OSA) (setup A), or a combination of an aperture located upstream of an elliptical, toroidal or even Kirkpatrick-Baez mirror system (setup B). In setup (A) the extent of the Fresnel zone plate can be considered as the spatial support. The order sorting aperture is used to remove higher-order foci. In (B) the aperture is used to define the spatial extent of the localized field distribution. As it is desired to apply the iterative technique to a broad range of photon energies, the setup A might not be feasible in all cases, since the issues related to the fabrication of Fresnel zone plates cause similar problems as discussed for the x-ray grating interferometry method. The setup B potentially can be used without a need for special fabrications, and the geometrical distance can be easily altered; compatible with different beamlines. Also, the use of an aperture upstream of the focusing optics enables the implementation of the error reduction algorithm, since the extent of the support is known ideally. Therefore, by measuring the far-field diffraction intensity of pulses, and given the knowledge of the aperture, both constraints of an error reduction algorithm are provided.

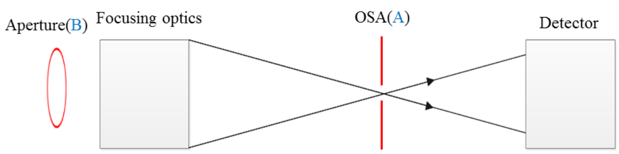

Figure 4.1: A scheme of the Fresnel coherent diffraction imaging wave field characterization. (A) and (B) introduce two different setups described within the section. The scheme is not to scale.

Depending on the extent of the aperture, the wavelength used and the aperture-to-focusing optics distance, it is possible to design a phase retrieval algorithm involving different Fresnel propagation operators. This opportunity increase the flexibility for experimental designs. The scheme of a modified iterative algorithm using the error reduction concept with setup A's modulus constraint set is depicted in fig.(4.2). The algorithm is started by a random guess of phase for the measured diffraction pattern and the trial wave field back propagates to where the support is positioned. The complex wave field is masked out(Π operator as the real space constraint set) by the support function. Henceforth, the estimation of localized field distribution propagates forward to the detector plane and the modulus of the resulting diffracted wave is replaced by the measured intensity(P projects the intensity modulus). The convergence is obtained when the Euclidean error metric approaches to a general minimum.

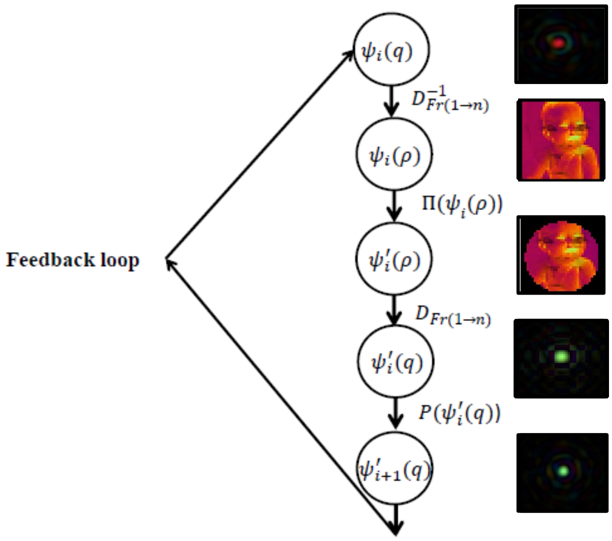

Figure 4.2: Iterative phase retrieval algorithm. The algorithm is initialized by ascribing a random phase to the measured diffraction intensity, and a series of reciprocal propagation (Feedback loop) is utilized until the Euclidean distance between the current estimate and measured amplitude converges to a steady state. Here P and Π are the Fourier and real space constraints used for an error reduction phase retrieval algorithm. The right column (up to bottom) shows an example of an iterative wave field reconstruction. Typically, a zero-padding in real space applies to satisfy the sampling requirement which is, for simplifying, not shown here. Phase is expressed by the hue and intensity by the brightness.

The solution to the 2D phase retrieval problem for a discrete diffraction pattern that can be represented by a Fourier series is almost unique when the diffracted wave is related to the original wave field via eq(2.35) [37, 38]. Intuitively, exploiting the strong curvature of a divergent beam downstream of the image plane ensures utilizing eq(2.35). Note that the unique solution is obtained if the numerical stability of the different operators is met,as well as the required sampling criterion. These key issues are addressed in the following section.

4.2 Modeling of Experiment

The experimental setup and general scheme of both Hartmann wavefront sensing and imaging experiments were described in the previous chapter in detail. In this section, the imaging branch will be investigated regarding required criteria to analyze the measured data.

4.2.1 Important Criteria

In principle, depending on the geometry chosen, the sampling criteria and intermediate field condition as well as the propagation stability have to be properly considered. The main issue linked to the canonical transformation (a Fourier transformation containing a spherical term) is the proper sampling of the spherical term such that the maximum local spatial frequency be sampled at the Nyquist rate.

Based on the FLASH beamline BL2 capability, the setup B of the previously proposed geometries was chosen using an elliptical mirror as the focusing optics, as well as a series of different size apertures. The scheme of highly focused wave field imaging experiment at BL2 is sketched in fig.(4.3). X-rays of wavelength λ are clipped by an aperture and focused by an elliptical mirror. A 2D CCD detector is located downstream of the focal plane where the Fresnel number satisfies the intermediate field condition.The distances at BL2 were measured as: $z_{01} = 71.5$ m,$z_{12} = 3.85$ m,$z = z_{23} + z_{34} = 3.2$ m. The nominal focal length of the elliptical mirror was given as $f = 2$ m.

Due to the sampling requirements on the intensity distribution, the support must be finite in extent. Here we consider the aperture size as a rigid constraint in real space. The aperture extent covers a region that at least is larger than the beam FWHM at the given plane, though not so large that it is a negligible aperture. Clearly, there is a trade off between selecting a more coherent region and avoiding to block most of the beam at the aperture plane.

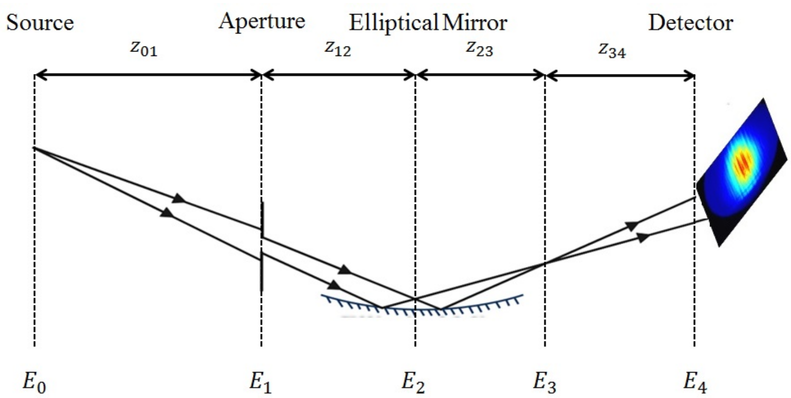

Figure 4.3: The highly focused wave field characterization geometry. Soft x-rays of wavelength λ are clipped by a circular aperture and focused by an elliptical mirror with 2 m nominal focal length. A two-dimensional detector (CCD) is located downstream of the focal plane where the Fresnel number satisfies the far-field condition. The aperture diameters, 10-5-3 mm, were the same as used for the Hartmann wavefront sensing experiments.

As discussed in the previous section, the phase retrieval algorithm may involve different propagators depending on the geometry and radiation wavelength. Alongside the benefit of this freedom, it is of vital importance to note that the quadratic phase factor involved in the Fresnel intermediate propagation may oscillate too rapidly to be sampled properly in a discrete array of convenient computational size. However, due to the beam divergence required, eq(2.35) governs the propagation between the elliptical mirror and detector. Therefore, as the remaining degree of freedom, the separation gap between the aperture and elliptical mirror can be adjusted such that the propagation obeys eq(2.32). This combination can increase the stability of the forward propagation strategy by convenient recasting of the propagation plane.

As discussed in chapter(2), eq(2.45) and eq(2.46) provide the rough sampling criteria for near and intermediate field propagation. In addition to the previously noted inequalities, the geometrical distances, z_{12} and $z = z_{23} + z_{34}$, as well as the aperture size must be chosen such that the Fresnel number, eq.(2.36), approaches the specific limits, establishing the near and intermediate zones.

Demonstrated by eq(2.47), an intermediate Fresnel propagation leads the sampling rate to be rescaled between two on-axis planes, the so-called propagation and observation planes. The sampling rate in the observation plane thus linearly depends on the propagation distance and inversely to the numerical field of view in the propagation plane.

The forward beam propagation from the elliptical mirror to the detector can be evaluated as a single Fourier transform which is the most straightforward. This method is desirable because of its computational efficiency. But, practically, the detector pixel size is fixed and determines the sampling rate at the focusing mirror. Thus, this transformation shrinks the sampling rate at the mirror plane and a forward propagation to the image plane, as would be needed to perform further analysis, expands the sampling rate at the image plane. The second strategy evaluates the Fresnel integral twice, which works out inversely by shrinking the sampling (or increasing the resolution) at the image plane, which is an ultimate goal of a successful complex wave field characterization. To clarify the resolution difference in two strategies, assume a detector with a 1024×1024 pixels, each 20μm×20μm , $z_{23} = z_{34} = 2.5$ m and $\lambda = 10$ nm. A direct propagation leads to a sampling rate equal to $\delta_2 = 2.4\mu$m at the EM plane and $\delta_3 = 10\mu$m at the image plane consequently. While a two steps propagation provides $\delta_3 = 1.2\mu$m which is 8 times smaller than the previously calculated. The indirect propagation method adds some flexibility in the grid spacing at the cost of performing a second Fourier transform, which is practically necessary to resolve typical foci in XFEL experimental setups.

Following the indirect propagation method, the propagation from the elliptical mirror to the image plane contains two spherical terms in the arguments of the Fourier transformation in eq(2.35). One of them governs the canonical transform and the other one the elliptical mirror effect as a perfect thin lens. Analytically, it can be formulated as following:

$$\psi(\rho', z_j) \simeq -\frac{i}{\lambda z_{ij}} \exp(i\frac{k}{2z_{ij}}\rho'^2)\, \mathcal{F}(\exp(i\frac{k}{2z_{ij}}\rho^2)\,.\,\exp(-i\frac{k}{2f}\rho^2)\,.\,\psi(\rho, z_i)), \tag{4.5}$$

where z_{ij} is the propagation distance between the elliptical mirror and image plane, f and λ are the nominal focal length of the elliptical mirror and wavelength. The third exponential term is the elliptical mirror effect as a perfect thin lens. ρ and ρ' are the transverse coordinates of the EM and image planes. Here we assume δ as the elliptical mirror plane numerical sampling rate.

Considering eq(2.42), the effective phase factor inside the argument of the Fourier transformation has to be sampled at least twice the Nyquist rate in each lateral direction,

$$f_{local} = \frac{1}{2\pi}\nabla_i \frac{k}{2}(\frac{1}{z_{ij}} - \frac{1}{f})\,\rho^2 = (\frac{1}{z_{ij}} - \frac{1}{f})\frac{\rho}{\lambda} \leq \frac{1}{2\delta} \tag{4.6}$$

ρ takes on its maximum value at the edge of the numerical grid where $\rho = \frac{N\delta}{2}$ and N is the grid number. After some algebra, we obtain

$$z_{ij} \geq \frac{N\delta^2 f}{2\lambda f + N\delta^2}. \tag{4.7}$$

The image plane distribution, $\psi(\rho', z_j)$, is highly localized in the neighborhood of ρ'. In practice, $\rho' \ll z_{34}$ results in the highly oscillatory region of this function does not contribute to the argument of the second Fourier transform, for a reciprocal propagation in between the image and detector planes. Therefore, the highly oscillatory term at the image plane is sampled finely enough and the numerical stability of the algorithm is preserved for an indirect propagation.

4.2.2 Wave Field Retrieval

One of the issues linked to the back propagation is that the sampling criterion is not satisfied in E_4 and the highly oscillating part contributing in the back propagation can not be properly sampled in the discrete array. This is overcome by recognizing that the wave is formed through the multiplication of a slowly varying component with a quickly varying one. By analytically propagating the quickly varying part and numerically propagating the remaining, the iterative algorithm remains numerically stable. To explain clearly, assume a simple two steps back and forth propagation,

$$\psi_{forth}(\rho', z_j) \simeq -\frac{i}{\lambda z_{ij}}\exp(i\frac{k}{2z_{ij}}\rho'^2)\,\mathcal{F}(\exp(i\frac{k}{2z_{ij}}\rho^2)\,.\,\psi(\rho, z_i)), \tag{4.8}$$

$$\psi_{back}(\rho, z_i) \simeq \frac{i}{\lambda z_{ij}}\exp(-i\frac{k}{2z_{ij}}\rho^2)\,\mathcal{F}(\exp(-i\frac{k}{2z_{ij}}\rho'^2)\,.\,\psi_{forth}(\rho', z_j)), \tag{4.9}$$

The first exponential term inside the Fourier transformation in ψ_{back} cancels out with the first exponential term, involving ρ', in ψ_{forth}. This inherent property of a feedback propagation algorithm enables numerically avoiding the highly oscillating term, involving ρ_4, which appears in the beginning and final steps of the algorithm. The analytical propagation here exploits this mathematical property.

With this information in hand, we can summarize the algorithm steps qualitatively as following: The algorithm is started by a guess of phase for the measured diffraction pattern and the trial complex wave field back propagates to an intermediate plane that specifies the approximate location of the image plane. Then it propagates to where the support is located and the complex wave field is masked out. Henceforth, the estimation of localized field distribution propagates forward to the intermediate plane and the detector plane. Then, the modulus of the resulting diffracted wave is replaced by the measured intensity at the detector plane.

To simplify the algorithm steps mathematically, Fresnel propagators are termed by $\Omega(\rho, z)$ as,

$$\psi_{(}\rho', z_j) \simeq -\frac{i}{\lambda z_{ij}}\Omega(\rho', z_{ij})\,\mathcal{F}(\Omega(\rho, z_{ij})\,.\,\psi(\rho, z_i)). \tag{4.10}$$

Also, we refer to eq(2.32) by using $\Upsilon_{z_{ij}}$ within this chapter.

The experimental geometry at beamline BL2 is designed such that eq(2.32) is valid for propagation distance z_{12} whereas eq(2.35) describes propagation over distances z_{23} and z_{34}.

To recover the complex wave field in the detector plane we use an extension of the iterative algorithm presented by Quiney *et al.*[36]. More specifically, we introduce an additional propagation between the entrance aperture and the focusing element. In addition, we consider a finite distance between source and aperture plane. Consequently, we require reciprocal propagation between four planes: the support plane E_1, the elliptical-mirror plane E_2, the approximate focal plane E_3, and the detector plane E_4.

Representing the wave field $\psi(\rho_4, z_{34})$ at the detector plane as a product $\psi^d\,\exp(i\frac{k}{2z_{34}}\rho_4^2)$ of a (nearly) planar and spherical component, the algorithm can be described as follows:

1. $\psi(\rho_3, z_3) \simeq \frac{i}{\lambda z_{34}}\Omega(\rho_3, -z_{34})\,.\mathcal{F}(\psi^d_{guess})$,
2. $\psi(\rho_2, z_2) \simeq \frac{i}{\lambda z_{23}}\Omega(\rho_2, \frac{z_{23}.f}{z_{23}-f})\,\mathcal{F}(\Omega(\rho_3, -z_{23})\,.\,\psi(\rho_3, -z_3))$,
3. $\psi(\rho_1, z_1) \simeq \Upsilon^{-1}_{z_{12}}(\psi(\rho_2, z_2))$,
4. impose support constraint on $\psi(\rho_1) \rightarrow \psi_{New}(\rho_1)$,
5. $\psi(\rho_2, z_2) \simeq \Upsilon_{z_{12}}(\psi_{New}(\rho_1, z_1))$,
6. $\psi(\rho_3, z_3) \simeq \frac{-i}{\lambda z_{23}}\Omega(\rho_3, z_{23})\,\mathcal{F}(\Omega(\rho_2, \frac{z_{23}.f}{f-z_{23}})\,.\,\psi(\rho_2, z_2))$,
7. $\psi(\rho_4, z_4) \simeq \frac{-i}{\lambda z_{34}}\,.\,\mathcal{F}(\Omega(\rho_3, z_{34})\,.\,\psi(\rho_3, z_3))$
8. impose wave field amplitude constraint on $\psi(\rho_4) \rightarrow \psi_{New}(\rho_4)$,
9. Substituting $\psi_{New}(\rho_4)$ as ψ_{guess} in step 1,

where subindex n of ρ_n corresponds to the n-th plane. Here f denotes the nominal focal length of the elliptical mirror and ψ^d_{guess} is a random complex wave field to initiate the algorithm. Later, within the context of Chapter 5 we refer to this algorithm as **Algorithm 0**.

The discrete Fourier transform (DFT) relation defines the pixel sizes between two consecutive planes and are given by:

$$\delta x_i = \delta x_j \quad (FN >> 1), \tag{4.11}$$

$$\delta x_i = \frac{\lambda z_{ij}}{N \delta x_i} \quad (FN << 1), \tag{4.12}$$

where δx_{ij} is the linear pixel size in two planes linked by the discrete Fourier transform, N is the pixel number in the discrete array, λ is the wavelength of x-ray and z_{ij} is the linear distance between two planes.

The Shannon sampling condition, to adequately sample quadratic terms involving in both Fresnel formalisms can be expressed as follows[95, 53]:

$$\frac{\lambda z_{ij}}{N(\delta x_i)} \leq 1 \;\; (E_1 \leftrightarrow E_2), \tag{4.13}$$

$$\frac{\lambda z_{ij}}{N(\delta x_i)} \geq 1 \;\; (E_2 \leftrightarrow E_3 \; and \; E_3 \leftrightarrow E_4) \tag{4.14}$$

here δx_i identifies the numerical sampling at the plane of propagation and $\leftrightarrow$ refers to a reciprocal propagation between two consecutive planes.

In the first few iterations we use a priori knowledge of the support's approximate size, and in further iteration a powerful tool to find a better estimate of support is called as **Shrink-Wrap** algorithm [34]. The support in this method is updated by thresholding the intensity of a blurred version of the current estimate of the localized field distribution under reconstruction. Thresholding traces the boundary of the localized field distribution at a given intensity contour. The blurring acts to smooth out the noise and provide a form of regularization. To find a new support one can thus make a convolution of intensity of localized field distribution with a Gaussian function of the width σ, typically covering a few pixel. *A-priori* knowledge of the support can potentially speed up the algorithm convergence, however, the support can be reconstructed by the shrink-wrap algorithm given minimal information about the support.

To establish a connection to the operator notation, we introduce projectors for the various multiplication in the algorithm as sketched in fig.(4.4).

The iterative algorithm can be compactly expressed by operator notation, as illustrated in fig.(4.4):

$$\psi_{k+1} = [M(I(q_x, q_y)).\pi.\chi.\Upsilon.S(A(x,y)).\Upsilon^{-1}.\chi^{-1}.\pi^{-1}]\psi_k. \tag{4.15}$$

Once convergence has been achieved, the algorithm is halted at step 7, which constitutes the best estimate of the wave field distribution, bounded within the aperture, in the detector plane.

The measure of algorithm convergence, ε, in this work will be based on that commonly used in the single plane coherent diffraction imaging phase recovery. The traditional definition of ε^t as referred to in [12] is

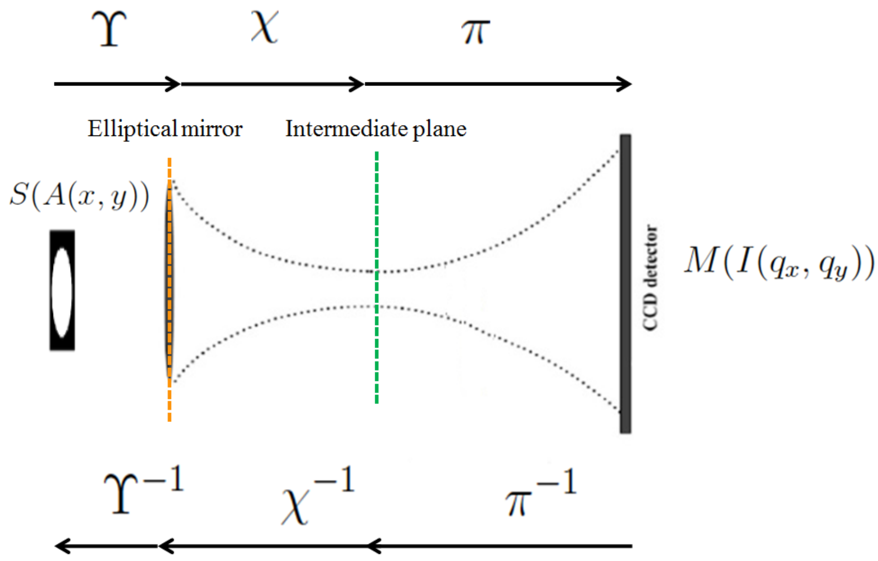

Figure 4.4: Operator notation. Each propagation is indicated by a projection and the constraints are specified with S as the support and M as the mapping operator in Fourier space. π,χ and Υ correspond to the eq(2.32) and eq(2.35) respectively. In the operator notation, the elliptical mirror is implemented as a perfect lens. The intermediate plane is an approximate location of the image plane, estimated using the focal length of the lens and z_{01}.

$$\varepsilon_q^t = \sqrt{\frac{\sum_{ij}(|\psi_p^q(\rho_4, z_{34})| - \sqrt{I_{measured}^q})^2}{\sum_{ij} I_{measured}^q}}, \tag{4.16}$$

where i,j represents the detector as a discrete array and q is the p-th measured intensity evaluation index.

Statistically, we can introduce a pixel wise error or standard deviation of the reconstruction in a 2D grid,

$$\varepsilon_q^s = \sqrt{\frac{\sum_{ij}(|\psi_p^q(\rho_4, z_{34})| - \sqrt{I_{measured}^q})^2}{i.j}}. \tag{4.17}$$

The convergence is obtained when either ϵ^t or ϵ^s approaches to a certain value fluctuating monotonically without an extreme deviation. Obviously, the error scale differs in the above definitions.

4.2.3 Numerical Modeling

To validate the algorithm's performance, we simulated the focus characterization experiment at the FLASH beamline BL2, as shown in fig.(4.3). Soft x-rays of wavelength 14.7 nm are cropped by a 5 mm circular aperture and focused by an elliptical mirror with

2m nominal focal length. A 2D pixellated detector containing 1024×1024 pixels with a pixel pitch of 13μm, is located downstream of the focal plane where the Fresnel number satisfies the far-field condition. In order to simulate the forward propagation of the wave field to the detector plane, we follow steps 5 to 7 of the algorithm. The distances are defined as: $z_{01} = 71.5$ m, $z_{12} = 3.85$ m, $z = z_{23} + z_{34} = 3.2$ m.

The simulated intensity and phase at the aperture plane are shown in fig.(4.5). Note that a stochastic intensity distribution is used as the incident intensity at the aperture plane, and the incident unmodified phase is taken to be spherical with a radius of 71.5m.

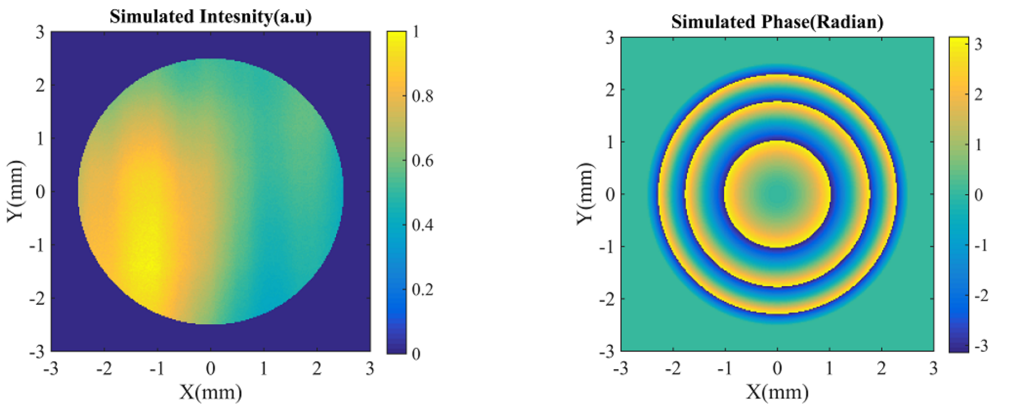

(a) (b)

Figure 4.5: Simulated divergent wave field. (a) and (b) show the input intensity and phase for a wave field illuminating the aperture. The image are 1024×1024 pixels with 23.3μm square pixels. The source-to-aperture distance is 71.5 m and the wavelength is 14.7 nm.

Then, we propagate the focused wave field to close to the theoretically calculated image plane, called an intermediate plane as indicated in fig(4.4) and located 2.044 m downstream of the elliptical mirror. Finding the plane with maximum sharpness norm in a vicinity of the intermediate plane would precisely figure out the on-axis image plane location. For each simulated single-shot reconstruction 200 iterations are used utilizing the shrink-wrap algorithm to find the proper support. The support is simply assumed as a perfect aperture with 5 mm diameter. The algorithm is initialized by a randomly distributed wrapped phase varying in a range [-π,π].

Fig.(4.6) illustrates the simulated diffraction pattern of the input wave field at the detector plane. In fact, this is essentially a low resolution image of the combined pupil function. In contrast to the Hartmann wavefront sensing method the higher frequency information can be accessible as shown in fig.(4.6.b).

Fig.(4.7) summarizes the results from the reconstruction of the simulated input wave field at the aperture plane. A 1D-profile comparison of the simulated and reconstructed phase within the aperture indicates an accurate reconstruction with a rms error of $0.05\lambda_{14.7}$. The phase was unwrapped here using a 2D version of the 3D unwrapping algorithm described in [88]. An average pixel-wise residual of less than 1% was observed

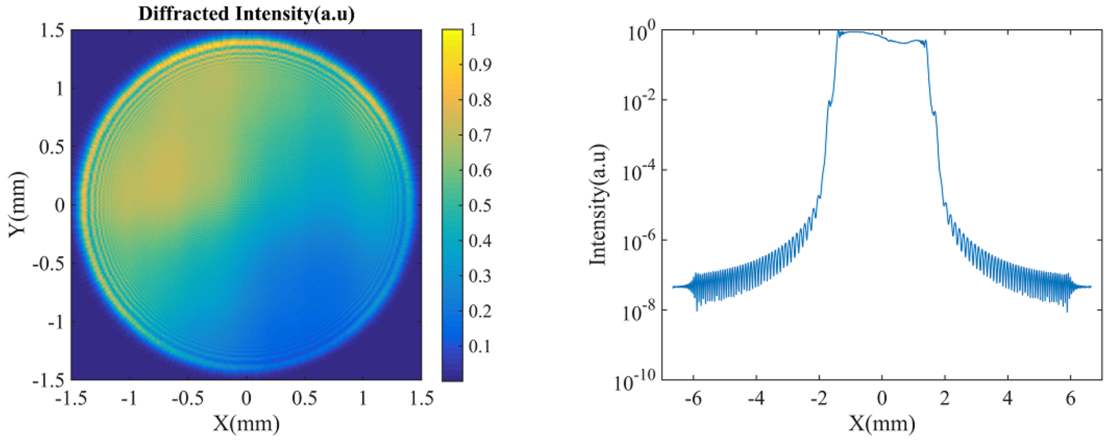

(a) (b)

Figure 4.6: The simulated diffracted intensity at the detector plane. The effect of aperture upstream of the focusing optics appears clearly as the circular fringes.

in the reconstructed intensity. As seen in Fig. 4.7(c), the reconstruction error monotonically approaches a minimum after 150 iterations. The support considered in the simulation was retrieved successfully within the first few iterations of the shrink-wrap algorithm. The reconstructions were performed by ascribing a random phase to the simulated amplitude to initiate the algorithm. The wave field reconstruction was found to be reliable and reproducible upon 50 trials for every single-shot by monitoring the lowest values of ϵ. A deviation of 2%, between these minimum values, was found and the absolute ϵ was less than 10^{-3}, indicating good convergence.

Under the assumption of geometrical optics the image plane location is 2.054 m downstream of the elliptical mirror. As demonstrated by eq(3.13), the peak of the sharpness indicates the precise position of the image plane which is specified by a red dashed line in fig.(4.8.a). A meridional profile of the simulated and reconstructed intensity at the intermediate plane, as an important involved step in the forth-back propagation, verifies the feasibility of the algorithm to reconstruct the localized wave field as depicted in fig.(4.8.b). After performing 50 simulated trials the average position of the image plane was obtained by back-propagating the reconstructed wave field and using eq.(3.13), as shown in Fig4.8(a). This yields $z_{23} = 2.054$ m with a standard deviation of $\Delta z = \pm 2$ mm, which indicates the uncertainty in the focal position that can be ascribed to the algorithm.

4.2.4 Noise Stability of The Algorithm

An important consideration to any algorithm one wishes to realize experimentally is its behavior in the presence of an imperfect signal. More specifically, in this application the key issue is the convergence (or potentially lack thereof) of the method, in comparison with the ideally simulated data. This can be explored by simulating noisy data by adding a normally distributed Gaussian noise with an average of zero and different

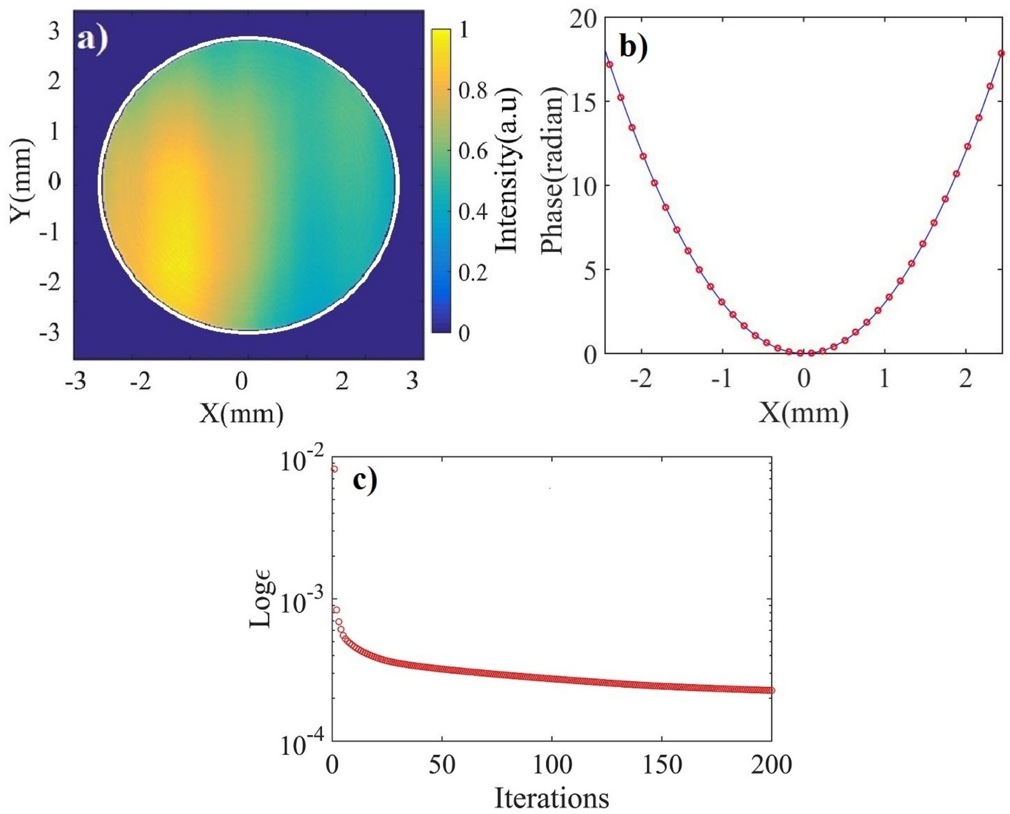

Figure 4.7: Input wave field reconstruction at the aperture plane. A visual comparison of the reconstructed (a) and simulated intensity (see Fig. 4.5) confirms a good quantitative recovery. The white circle in (a) represents the extent of the successfully reconstructed support. (b) displays a central line profile comparison of the simulated (blue line) and reconstructed (red dots) phase concluding an accurate reconstruction. The error evaluation is depicted in (c).

standard deviation equal to some defined proportion of the signal in each pixel, to the simulated diffracted intensities. Note that, we consider a simple case of a Gaussian noise distribution which is valid in the limit of large counts per pixel. For many trials of simulation, different levels of noise were considered. It was observed that, with a noise level less than 10% of the signal level, the algorithm converges to a reliable solution according to the relative difference between the reconstructed noisy and noise-free simulated wave fields,

$$\alpha = \frac{\sum_{ij} I_{rec}^{no} - \sum_{ij} I_{rec}^{id}}{\sum_{ij} I_{rec}^{id}} \tag{4.18}$$

where I_{rec}^{id} presents the reconstruction of a noise free pulse, and I_{rec}^{no} is the reconstruction of the same pulse with noise added. $\sum_{ij}$ is a summation over the discrete array.

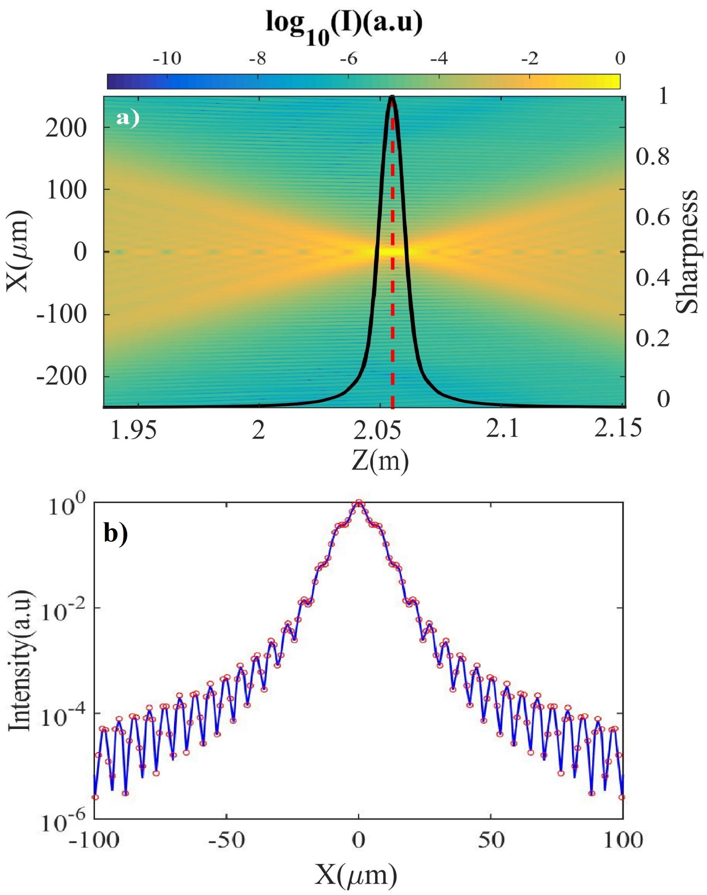

Figure 4.8: The image plane wave field reconstruction of the simulated data. A meridional profile of the focused wave field's intensity is shown in (a). The image plane on-axis location (red dashed line) was determined accurately ($z = 2.054m$) using eq.(3.13) as plotted (black curve) in (a). In (b) the line profile of the intensity distribution for reconstructed (red dots) and simulated (blue line) wave field are depicted on a logarithmic scale to highlight the full recovery of the contribution of the sidelobes. Note that the sharpness is normalized to unity in (a).

For a small noise level in the detection plane (i.e. 1 or 2% of the signal level) the difference between the noisy and noise free image are relatively small. Increasing the noise level, for instance 3 and 5% of the signal level, imposes a series of artifacts inside the reconstructed wave field, as well as upscaling the error metric level. As soon as approaching a higher noise level more than 10% the convergence is interrupted. This is reflected in the real space α being approximately 0.035(for 1% signal level), 0.060(for 2% signal level),0.1(for 3% signal level),0.13(for 5% signal level) and 0.24(for 10% signal level). Also, the imposed effect in the reconstruction can be seen in fig.(4.9).

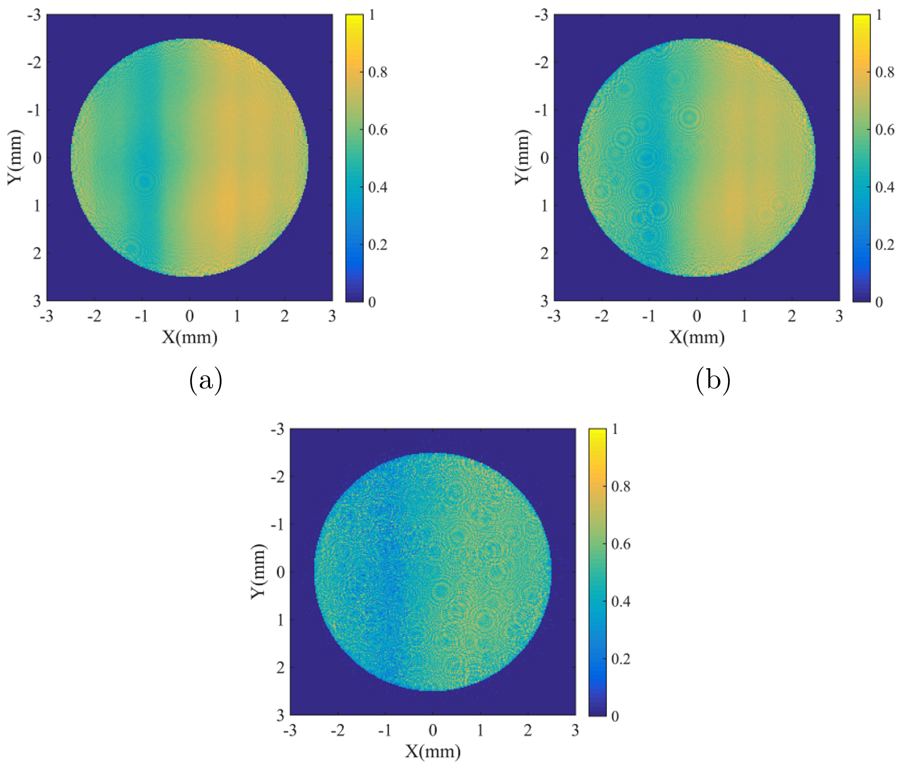

(a) (b) (c)

Figure 4.9: Reconstructed noisy wave field. A Gaussian noise was added to the detector plane diffracted intensity with the different levels. Adding a noise more than 3% of the signal level imposes an unwanted artifacts which potentially can be misinterpreted. A noise level higher than 10% leads to the lack of the algorithm convergence. (a-c) reflect the reconstructed wave fields at the aperture plane, with added 3%,5% and 10% Gaussian noise.

4.2.5 Partially Coherent Wave Field Retrieval

As a conceptual assumption, the iterative algorithm assumes a coherent field illumination. Practically, as studied in [96, 61], at FLASH the SASE process can amplify a variety of active modes that may alter in transverse coherence from shot to shot. As demonstrated in [97], the Fresnel coherent diffraction imaging can be directly applied to retrieve partially coherent wave fields with a specific generalized treatment which will be discussed in the next chapter broadly. Practically, it was shown[13] that some deviation in coherence from ideally to highly coherent wave field illumination is tolerable by the current algorithm. Therefore, a fully spatially coherent illumination is not necessarily required to apply the algorithm; a highly coherent wave field, which is practically accessible as A1(2) regime at FLASH1, would lead to a successful implementation of the iterative algorithm. Here as a simple example to basically understand this effect, we simulated a highly coherent illumination by blurring a simulated coherent experiment.

A blurring by a few pixels does not dramatically change the degree of coherence and one can expect that algorithm reconstructs the wave field successfully.

Fig.(4.10.a) illustrates the blurring as smoothing of the highly oscillating region of data. It is seen that algorithm converges reliably after 200 iteration to a solution in general agreement with the simulated complex wave field with a Q equals to 0.02. This realization build up the Fresnel coherent diffraction imaging method as a robust approach to be implemented at the FLASH beamline BL2 considering a coherence degree above of 80% for pulses delivered by the weak compression regime.

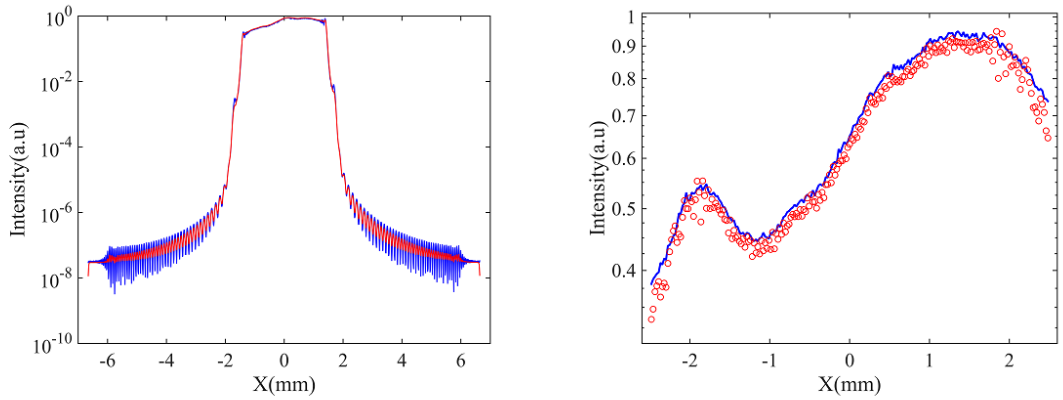

(a) (b)

Figure 4.10: Focused highly coherent wave field retrieval. An approximately highly coherent wave field was generated by slight blurring of the diffracted wave field (red solid line of (a)). As a consequence of blurring, the high angle tails of simulated diffraction pattern (blue solid line of (a)) were smoothed out. (b) shows the 1D central profile of the simulated and reconstructed intensities. It implies that for highly coherent pulses, but not full coherent, the algorithm is still able to reconstructs the wave fields. Note the plots in (a-b) are the meridional profiles of intensities to be easily compared.

4.3 Results

4.3.1 Data Treatment

The data were acquired for each of the three different apertures (3 mm, 5 mm, 10 mm diameter) downstream of the elliptical mirror, as well as for a variety source parameters such as the weak and strong compression regimes and different active undulator segments (as listed in Table(3.3)).

Fig.(4.11) displays histograms of the intensity distribution (pixel counts in a single-shot) of the acquired data frames versus the different aperture sizes and different regimes. In the A3 regime (3^{rd} row) the intensity distribution falls in a negative exponential distribution, suggesting the perfect SASE performance[5]. To monitor the fluctuation in each data set, σ_m was introduced as the ratio of the standard deviation to the mean intensity. As seen, by decreasing the aperture size σ_m scales down significantly. For the 3 mm aperture size in A4 and A3 regimes one can recognize a larger σ_m in respect to A2 and A1 which reflects a higher level of fluctuation in the presence of the strong bunch compression.

The subsets of data was selected by including frames which are correlated with a deliberately measured reference frame taken during the experiments. The reference frame for each data set was selected among the frame collected between two consecutive losses of the beam with the longest period of the beam stability between the gap. This ensures a reference measurement during the most stable period of radiation. The correlation made enables us to disregard known instabilities in the apparatus and beamline, as well as the occasional loss of beam observed during the experiments, and observe only the meaningful variations of the source. The cross-correlation operator is defined as[13],

$$Q_{ij} = \frac{\sum_{n=1}^{N} I^i(x_n)\, I^j(x_n)}{\sum_{n=1}^{N} I^i(x_n)\, \sum_{n=1}^{N} I^j(x_n)}, \tag{4.19}$$

where x_i are collection of N pixels in the array. Note that Q_{ij} is calculated with respect to the one frame across the data set. A typical cross correlation plot is shown in fig.(4.12). As seen, during 700s data acquisition the loss of beam possesses a very strong instability such that only half of the collected data are self-consistent. In addition, in the data treatment, we consider reconstruction with the subset including frames with $Q > 0.95$. This value ensures a reasonable data processing in respect to the numerical time consumption for a bunch analysis. The frequent instabilities requires a long period of data acquisition to ensure a proper data analysis for a single-shot pulse study.

To account for noise contributions, dark frames were collected during the experiment, separately for each data set, were averaged and used in a background subtraction for each data frame. the subtraction was performed on a pixel by pixel basis according to

$$I^{corr} = \max\{I^{frame} - (1+\beta)I^{dark}, 0\}. \tag{4.20}$$

By application of Eq(4.20) the camera readout noise contributions to I^{corr} can be strongly inhibited due to the regularization term β. β denotes the standard deviation of the dark images, relative to its mean. Values of β approaching zero (from 10^{-3}) are applied and the results remain unaffected by this regularization term, building confidence in the absence of modal bias in these reconstructions.

The position of the approximate image plane was also chosen as identical to the simulation for each single-shot reconstruction which will be modified within the algorithm. Note that for each case we monitor the error metric versus the number of iterations.

4.3.2 Overview of The Wave Fields Reconstruction

In fig.(4.13–4.15), we display a series of the complex wave field reconstructions for the different cases. For each case, 100 pulse reconstructions were performed and those with the lowest error level are shown here. Note that, the reconstructed wave fields listed

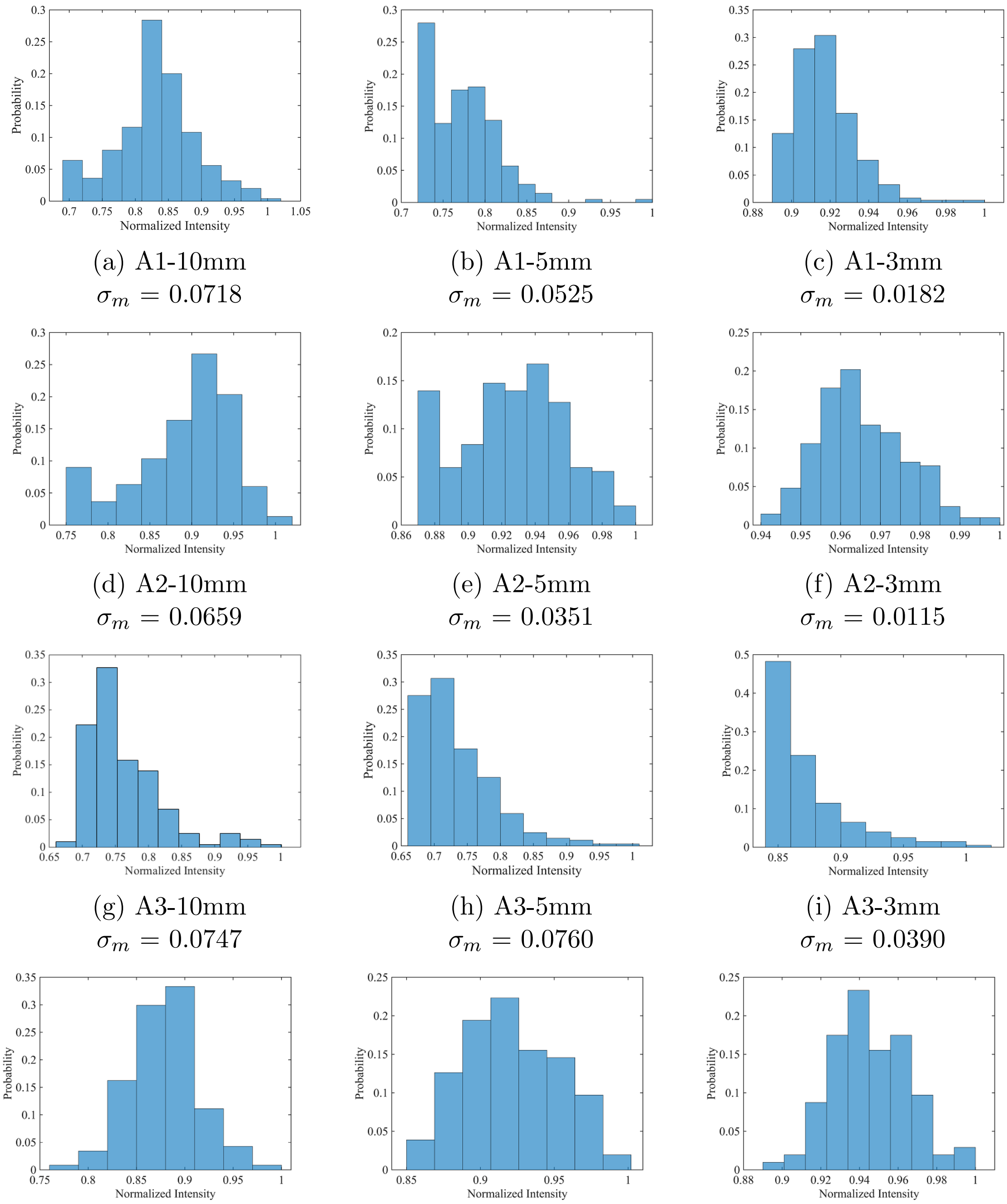

(a) A1-10mm $\sigma_m = 0.0718$
(b) A1-5mm $\sigma_m = 0.0525$
(c) A1-3mm $\sigma_m = 0.0182$
(d) A2-10mm $\sigma_m = 0.0659$
(e) A2-5mm $\sigma_m = 0.0351$
(f) A2-3mm $\sigma_m = 0.0115$
(g) A3-10mm $\sigma_m = 0.0747$
(h) A3-5mm $\sigma_m = 0.0760$
(i) A3-3mm $\sigma_m = 0.0390$
(j) A4-10mm $\sigma_m = 0.0425$
(k) A4-5mm $\sigma_m = 0.0356$
(l) A4-3mm $\sigma_m = 0.0261$

Figure 4.11: Histograms of the acquired data. The intensity fluctuation due to the chaotic nature of SASE process can be seen in all cases, especially in A3 regime (using the strong electron bunch compression and four undulators) falling into a negative exponential distribution.

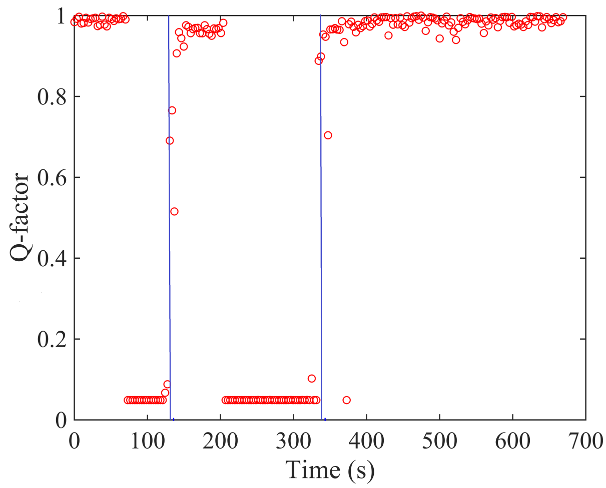

Figure 4.12: Cross correlation of 250 frames of A4 data with 5 mm aperture size. The Q-factor was calculated against a single data frame collected at 477s. The gaps reflects the periods of the beam loss, indicated by blue solid line. The subset with a Q>0.95 and longer period of consistency was chosen to be retrieved.

were retrieved at the aperture plane. A comparison between reconstructed pulses of the A3 and A4 regimes with the measured data showed a convergence to a local minimum. As discussed earlier, the iterative phase retrieval algorithm may converge to a steady state which is not the solution of the problem due to the either noise level or a lack of coherence. As seen in fig(4.14.g-l), the algorithm reached to a minimum value of error after which no improvement in reconstruction was achieved while the reconstructed amplitudes (fig(4.13.g-l)) showed α values higher that 0.12, stating unsuccessful reconstructions. For the A1 and A2 regimes α values were less than 0.03, and the difference in the amplitude of reconstructed and measured pulses were not recognizable by eye. Hereafter, an incompatibility between the convergence of the error metric and α is called a partial convergence attributed mainly to the coherence level of the pulses measured. This effect of partial coherence is addressed specifically in the next chapter.

Hence, in this chapter, only the phase reconstructions of the successful (highly coherent) cases are displayed. This includes subtracting the defocus and tilt-top term to monitor the phase fluctuation. The defocus subtracted phase shown here were selected as those yield the minimum peak-to-valley among the frames of the data set. Here, the Zernike polynomials were fitted to each reconstructed unwrapped phase. In the previous chapter, we have performed a similar operation at the detector plane to retrieve the phase fluctuation.

In fig.(4.16) the peak-to-valley and rms error of the reconstructed phases for the larger aperture size within A1 and A2 regimes are listed. The calculated peak-to-valley covers a range from less than λ to more than 4.5λ demonstrating a significant change within a time series of acquired data. As discussed, the reliability of the algorithm was established by performing many trials for every single-shot of a specific dataset. A unique phase reconstruction was observed over all trials performed for every single pulse. The reconstructed phases upon 50 trials for every single-shot always yielded a pair-wise correlation of higher than 97% and a difference of less than 0.01λ regarding the corresponding peak-to-valleys. This observation shows that the phase fluctuations measured are invariant under different trials of the algorithm.

A correlation analysis (as α with the phase values instead of the intensities measured) of retrieved phases showed a mean value of 88% with a standard deviation 10% for the A1, and 82% with a standard variation 10% for the A2. The variations in peak-to-valley and correlation made imply that for the A1 and A2 regime the phase of a pulse may be described by a general map due to the higher level of α (a general boundary with the known separated subdivisions), with changes of the phase value within the subdivision (describing the peak-to-valley change). A combination of both effects would be regarded to quantitatively describe the phase variations. A higher level of the peak-to-valley fluctuation was observed within the reconstructed data using the iterative technique compare to the Hartmann wavefront sensing. However, in both methods the reconstructed phases yielded a pair-wise correlation value of higher than 80% on average. The difference observed in the peak-to-valley can be attributed to the limited resolution and sensitivity of the Hartmann wavefront sensing method. As pointed out earlier, the subset of measured intensities were selected such that α value remains larger than 95%. Therefore, the analyzed intensities are as correlated as the reconstructed phases.

A comprehensive understanding of the phase change for every given regime relies on the study of the all pulses measured using a general iterative algorithm applied to the partially coherent pulses measured. This will be discussed in the next chapter.

4.3.3 Image Plane Wave Field Reconstruction

We follow the approach discussed in sec.(3.5) to retrieve the image plane distribution of the varied radiation regimes. Here, to continue the data analysis carefully and more reliably we discuss only the A1 and A2 regimes which generate spatially coherent single pulses to be back propagated numerically within the frame of free-space light propagation. We refer to the image plane when the sharpness norm reaches its maximum value in a vicinity of the intermediate plane, in a range within that the Fresnel near field propagation criterion is kept. In fig4.17 the meridional profiles of the intensity for a single-pulse (yielding the lowest value of the error metric within the data set) for the different aperture sizes in the A1 regime are shown.

On average, a longitudinal image position of $\bar{z}_{23} = 2.060$ m with a standard deviation of $\Delta z = \pm 4$ mm is determined for the A1 regime over all the reconstructed pulses (300 frames) with the different aperture sizes since the determination of the image plane position would not be a function of the different aperture sizes. A similar analysis for the A2 regime resulted in $\bar{z}_{23} = 2.050$m with a standard deviation of $\Delta z = \pm 7$ mm, indicating image-plane on-axis fluctuations smaller than the Rayleigh range.

Additionally, in table(4.1) the averaged lateral FWHMs of reconstructed single-shot pulses with the iterative phase retrieval algorithm approach and the Hartmann wave-

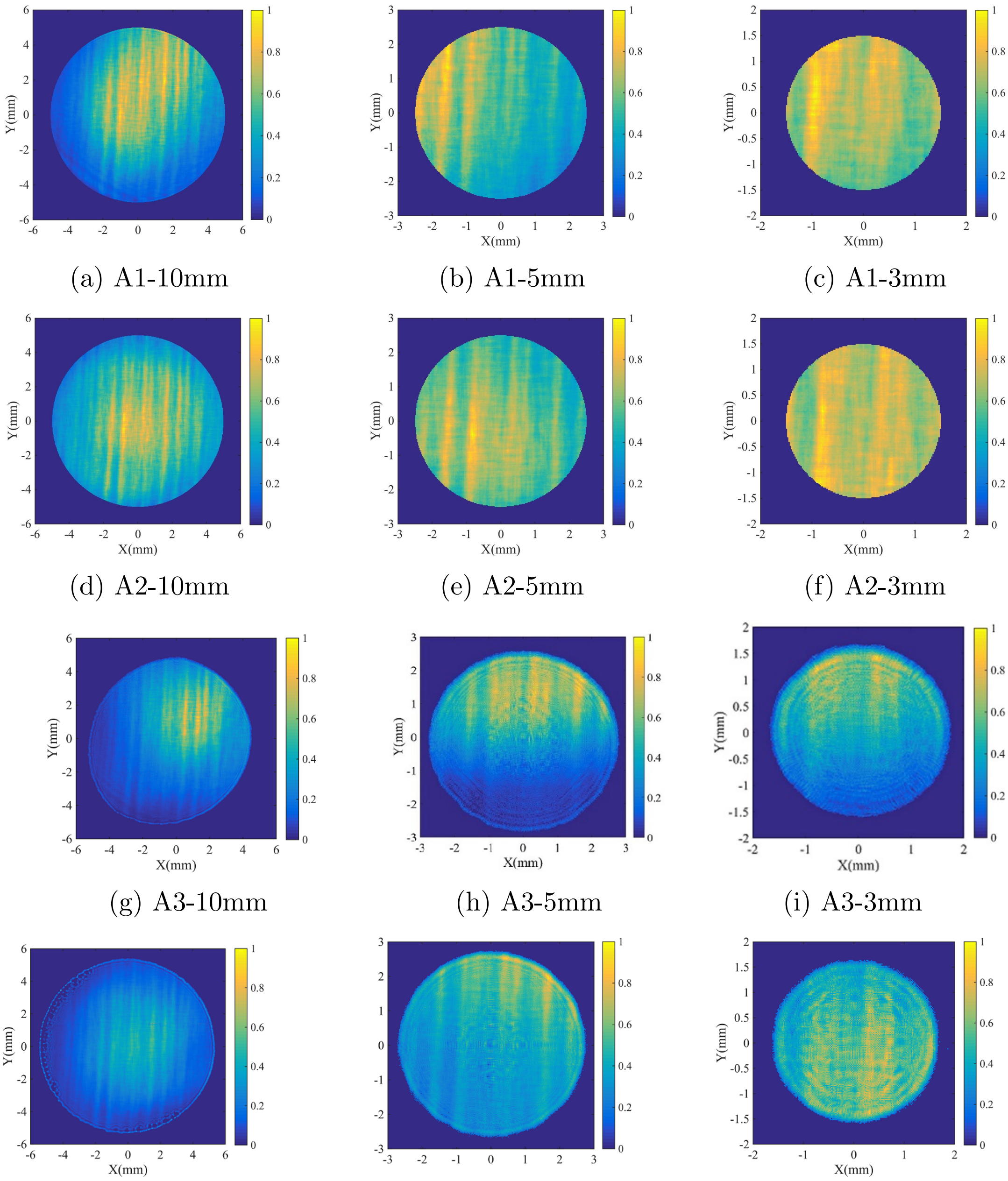

(a) A1-10mm (b) A1-5mm (c) A1-3mm

(d) A2-10mm (e) A2-5mm (f) A2-3mm

(g) A3-10mm (h) A3-5mm (i) A3-3mm

(j) A4-10mm (k) A4-5mm (l) A4-3mm

Figure 4.13: The single-shot intensity reconstruction. An overview of the intensity (in a normalized unit) reconstruction at the aperture plane utilizing the shrink-wrap algorithm in 200 iterations. In A3-A4 regimes due to a lower level of coherence, the lack of convergence can be seen qualitatively in (g-l) and, as expected, the algorithm did not completely converge to a global minimum. The color bars are in a normalized unit in linear scale.

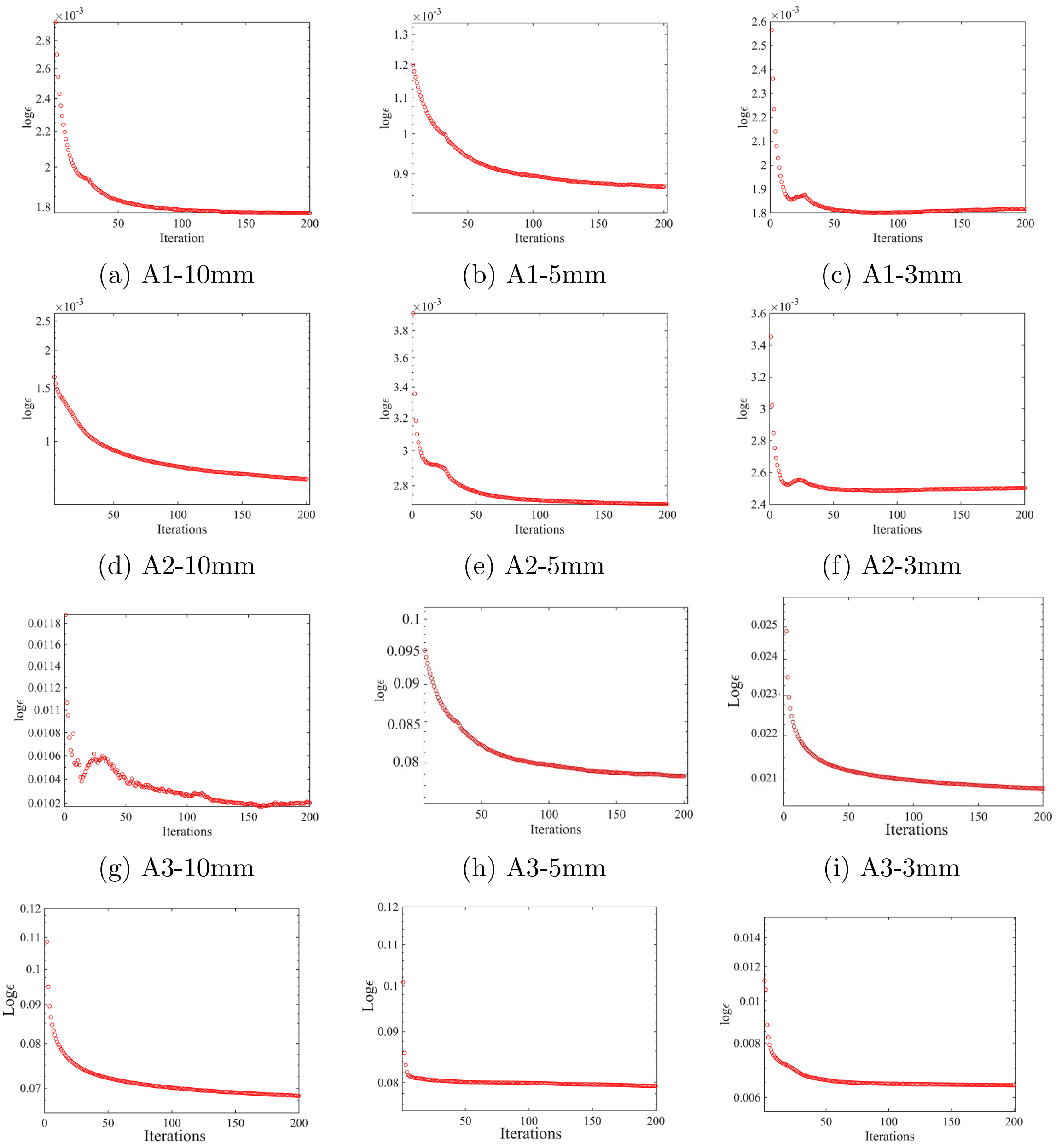

(a) A1-10mm (b) A1-5mm (c) A1-3mm

(d) A2-10mm (e) A2-5mm (f) A2-3mm

(g) A3-10mm (h) A3-5mm (i) A3-3mm

(j) A4-10mm (k) A4-5mm (l) A4-3mm

Figure 4.14: Logarithmic error metric of the reconstructed single-shot pulses yielding the lowest value of the error among the reconstructed frames within the data sets. As shown the phase retrieval algorithm approaches to a minimum value which necessarily does not reflect that the solution is found. The comparison of measured amplitudes with the reconstructions shown in fig(4.13.g-l) show that the iterative phase retrieval algorithm is stagnated in a local minimum may be attributed to the partial coherence properties of the A3 and A4 regime. The A1 and A2 pulses were reconstructed successfully in 200 iterations with a α level of less than 0.02.

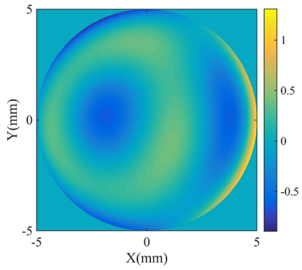

(a) A1-10mm

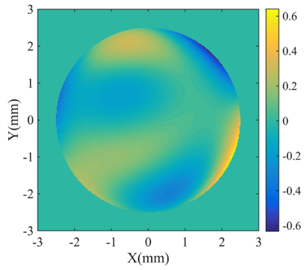

(b) A1-5mm

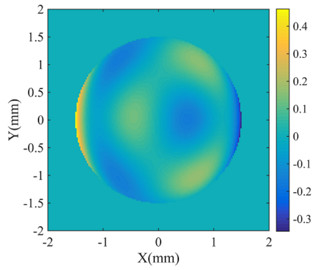

(c) A1-3mm

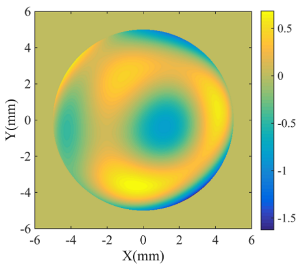

(d) A2-10mm

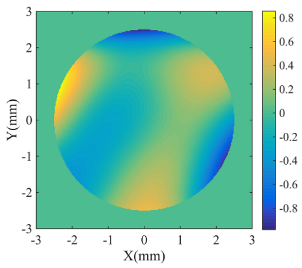

(e) A2-5mm

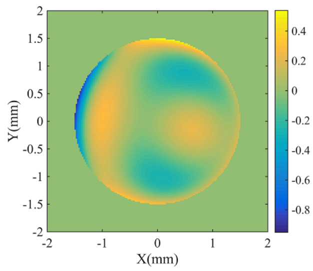

(f) A2-3mm

Figure 4.15: Reconstructed single-shot phases of the A1 and A2 regimes at the aperture plane. A defocus term was subtracted from the single-shot reconstructed phases to observe the meaningful variations of the phases. The phases shown here yielded the lowest peak-to-valley value within the retrieved phases in the data sets. Within 100 frames of the measured data for the A1 and A2 regimes a high level of correlation (up to 80%) was observed between the single-shot reconstructions. The changes in peak-to-valley and the correlation quantify a significant shot-to-shot phase change between the pulses measure.

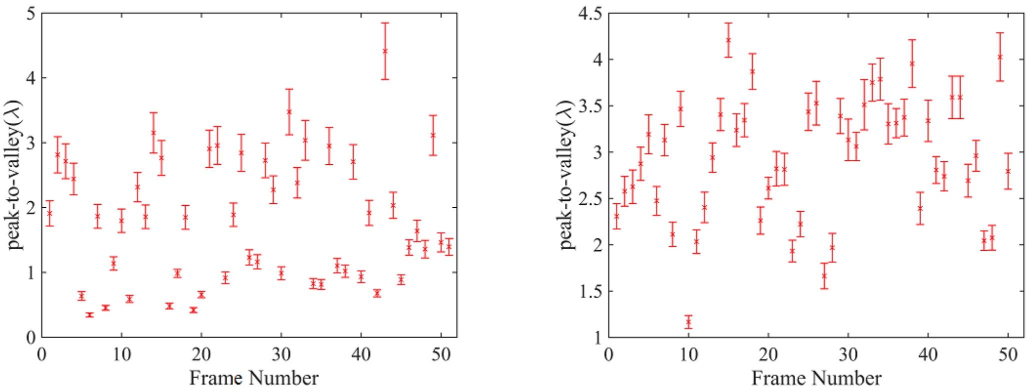

(a) A1-10mm (b) A2-10mm

Figure 4.16: Monitoring the phase fluctuation. For every single shot the reconstructed phase was unwrapped at the aperture and detector planes. The peak-to-valley values were calculated at the aperture plane subtracting the defocus term as the dominant effect encoded into the phase.

front sensing method are compared. The calculated FWHMs in both cases are larger than the diffraction spot sizes that is seen in the previous chapter. Note that, as used in the previous chapter, we consider the 4σ method to find the beam width and consequently the transverse FWHMs in each lateral direction. The current results are in a reasonable agreement with the data analyzed in the previous chapter demonstrating a reliable consistency in both methods.

Table 4.1: **The average beam parameters in weak compression regime versus different aperture sizes. A standard deviation of $1\mu m^2$ is considered to the calculated FWHMs here, as the maximum level of the standard deviations found within the determined parameters of the different data sets.**

	Aperture size(mm)	Averaged beam width(μm^2) – Imaging method	Averaged beam width(μm^2) – Hartmann wavefront sensing method
	10	6.72×6.77	6.71×6.66
A1	5	9.53×9.58	9.5×9.43
	3	16.24×16.10	17.86×16.95
	10	5.15×5.23	5.35×5.25
A2	5	9.55×9.5	10.24×9.80
	3	15.14×15.21	17.10×17.32

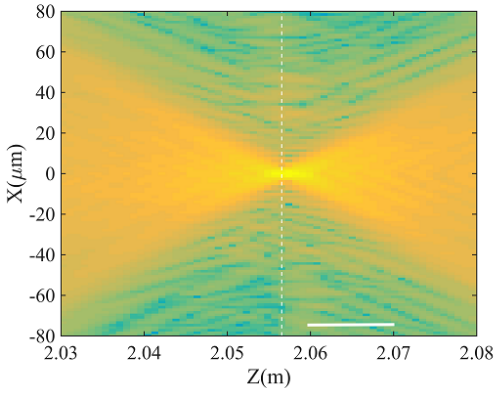

(a) A1-10mm

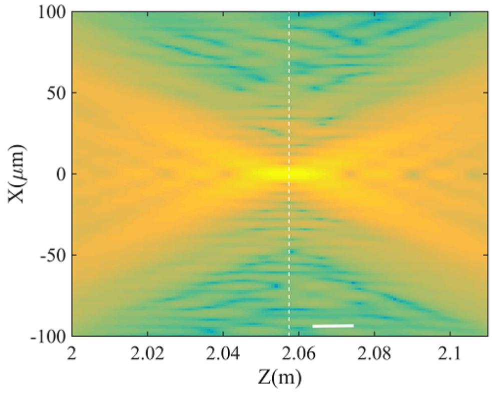

(b) A1-5mm

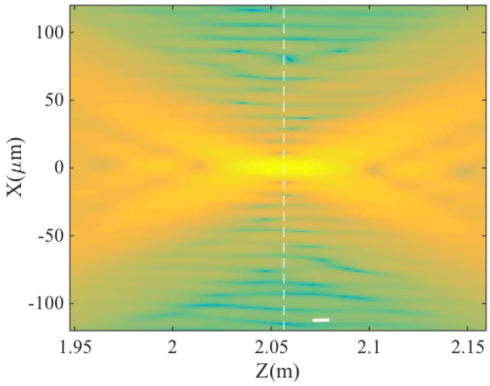

(c) A1-3mm

Figure 4.17: The reconstructed meridional profiles of the intensity for the different aperture sizes. A reconstructed wave field at the detector plane can be back propagated to the intermediate plane when the coherence assumption is valid. Thus, the image plane can be found when the sharpness reaches its maximum in a vicinity of the intermediate plane. The single pulses shown here yielded the lowest value of the error metric among 100 reconstructed pulses of the data sets. The dashed lines in (a-c) indicates the image plane position as 2.056 m,2.057 m,2.056 m downstream of the elliptical mirror. Here, a numerical (systematical) error of 4 mm would be considered to interpret the single-shot determined values accurately. The solid white line is a 1 cm scale bar. The plots are in a logarithmic scale with an arbitrary unit.

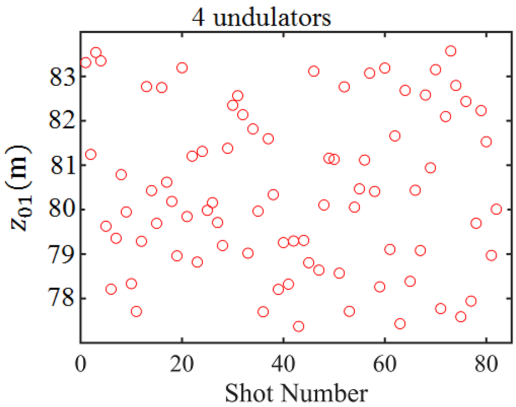

(a) A1-5mm

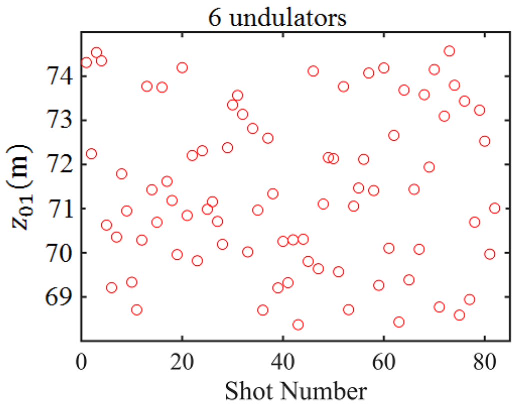

(b) A2-5mm

Figure 4.18: An example of the shot-to-shot longitudinal source position fluctuation. (a-b) show the fluctuation of the longitudinal source position upstream of the end of the last undulator. The wavefront radius of curvature was determined as 80.50±2.5 in (a) and 71.50±2.5 in(b).

4.3.4 The Systematic Source-Point Position

Finding the single shot image plane positions informs one of the longitudinal source-point position fluctuation. As the image plane is the image of the source performed by the elliptical mirror, one can simply use the optical law of image formation and calculate the elliptical mirror-source distance and the aperture-source distance. To illustrate the fluctuation of the source position, one subset from A1 and one subset from A2 were chosen. These subsets were the most self-consistent subsets among the data measured. Despite the photon noise, the measured source-aperture distance (or conventionally wavefront radius of curvature) follows the nominal displacement with a relative accuracy of about 2.5 m. For these specific subsets of data the average effective-source position for the 4 undulators setup (fig4.18.a) was found to be 80.50±2.5 m, and 71.50±2.5 m for the 6 undulators setup (fig4.18.b), yielding a difference of 9m. On average, the relative difference of the source position between 4 undulators and 6 undulators setting was found approximately 10m (with a standard deviation of 2.5m) which is comparable with the length of two undulator segments (≃10m). Throughout the experiment, the source point remained upstream of the end of the last undulator[86]. Such longitudinal fluctuations reflect a gain variation along the undulator. The positional fluctuation does not fit perfectly to a Gaussian function, which may be attributed to an insufficient statistics or a complex process governing the radiation within the undulator.

4.4 Summary and Conclusion

An algorithmic phase retrieval approach to characterize coherent, focused FEL pulses on a single-shot basis has been demonstrated numerically and experimentally. The results obtained compare favorably with the established Hartmann wavefront sensing method performed with the same FEL parameters. A high level of correlation was observed between the results of both methods, illustrating the ability of the new iterative method to reconstruct focused wave fields without the need for using conventional manipulative optics such as absorbing screens.

It should be noted that the comparison between both Hartmann wavefront sensing and iterative methods was made due to the applicable FEL energy of FLASH for the Hartmann sensor. In general, Hartmann plates function well for softer energy ranges and may not apply to the hard photon energies at XFELs, such as the European XFEL. The iterative imaging method—not relying on the properties of absorptive optics between the focusing optics and detector—provides a general technique applicable across a very broad photon energy range, as well as for different focusing optics for highly spatially coherent beam.

The degree of coherence and signal-to-noise ratio manifest themselves as the key issues governing the algorithm convergence. For source parameters satisfy both conditions the algorithm rapidly converges to a reliable solution with a α value less than 0.02. As discussed, a successful complex wave field reconstruction is achieved by monitoring both the error metric convergence and α value. Reaching to a steady state of the error evaluation may imply that the algorithm is stagnated at a local minimum. This effect was observed when the strong compression data were analyzed due to the a deviation in the degree of coherence, as theoretically was predicted. The partially coherent case is addressed in the next chapter.

Statistical analysis of the different regimes reflected the shot-to-shot variation of the wave fields, and also as the exact on-axis position of the image plane for every single-shot is resolved, the associated longitudinal source-position fluctuations can be found. This enables, for example, to introduce an effective source-position within the undulators, and for monitoring of the source gain variation within the active undulators of an FEL source.

CHAPTER 5

Partially Coherent Wave Field Characterization : An Extension of Coherent Diffraction Imaging Techniques

In general, different compression regimes of FELs may result in wave fields of that are not perfectly coherent . Partially coherent diffracted intensities cannot be simply interpreted as the moduli of wave fields determined by their amplitudes and phases. Therefore, the prerequisite of coherent propagation, and consequently coherent phase retrieval algorithms, is fundamentally not satisfied. We also recall that the method of phase recovery discussed in the preceding chapter often fails in the presence of partially coherent pulses. In this chapter we discuss the Generalized Schell's Theorem and demonstrate a revised and generalized iterative algorithm to reconstruct partially coherent wave fields as well as estimate the degree of coherence associated with them.

5.1 Various representations of a partially coherent wave field

The general framework of optical coherence theory is well established and has been described in numerous publications([60],[62],[47],[98]). As shown in the first chapter, a partially coherent wave field is no longer a solution of Maxwell's equations and measured diffraction patterns of an aperture illuminated by partially coherent radiations are not simply the moduli of the diffracted wave fields. Therefore, the prerequisite of a phase retrieval algorithm, as simultaneously satisfying both constraints, is violated. In order to achieve the goal of recovery the wave field for partially coherent FEL pulses, the properties of either cross spectral density or mutual optical intensity as a way to be applicable to phase retrieval algorithms are revised.

5.1.1 Modal representation

It is clear that a numerical implementation of cross spectral density function may be difficult due to the high dimensionality of the problem. A desirable solution might treat the cross spectral density as an ensemble of electrodynamic fields, of the same frequency of ω, depending solely on one spatial component $\boldsymbol{r}$. An affirmative solution to expand the cross spectral density as ensemble of separable basis in $\boldsymbol{r_1}$ and $\boldsymbol{r_2}$ was given in[99],[100].

Since $W(\boldsymbol{r}, \boldsymbol{r}, \omega)$ represents the intensity at frequency ω, $I(\boldsymbol{r}, \omega)$, measuring of the instantaneous power can be practically assumed in the sense that[99]:

$$\int I(\boldsymbol{r}, \omega) d^2 r < \infty. \tag{5.1}$$

Consequently, by Plancherel's theorem, $W(\boldsymbol{r_1}, \boldsymbol{r_2}, \omega)$ is square-integrable with respect to $\boldsymbol{r_1}, \boldsymbol{r_2}$ and ω as follows[99]:

$$\int |W(\boldsymbol{r_1}, \boldsymbol{r_2}, \omega)|^2 d^2 r_1 d^2 r_2 < \infty. \tag{5.2}$$

From eq(2.48) and eq(2.52), it directly follows that:

$$W(\boldsymbol{r_1}, \boldsymbol{r_2}, \omega) = W^*(\boldsymbol{r_1}, \boldsymbol{r_2}, \omega), \tag{5.3}$$

and the positive definite property of the characteristic function integral,

$$\int W(\boldsymbol{r_1}, \boldsymbol{r_2}, \omega) f(\boldsymbol{r_1}) f^*(\boldsymbol{r_2}) d^2 r_1 d^2 r_2 \geq 0. \tag{5.4}$$

Eqs.(5.2)-(5.4) imply that $W(\boldsymbol{r_1}, \boldsymbol{r_2}, \omega)$ is a non-negative, Hermitian and square-integrable function. The Gram-Schmidt procedure systematically admits a uniformly convergent expansion, constructing a set of orthonormal functions in the general form[43],

$$W(\boldsymbol{r_1}, \boldsymbol{r_2}, \omega) = \sum_n a(\omega)_n \psi_n(\boldsymbol{r_1}, \omega)\psi_n^*(\boldsymbol{r_2}, \omega), \tag{5.5}$$

where $a(\omega)_n' s$ are eigenvalues and $\psi_n' s$ are the eigenfunctions determined by the Friedholm's integral equation as follows[43]:

$$\int W(\boldsymbol{r_1}, \boldsymbol{r_2}, \omega)\, \psi_n(\boldsymbol{r_1}, \omega)\, d^2 r_1 = a_n(\omega)\psi_n(\boldsymbol{r_2}, \omega). \tag{5.6}$$

Since each term on the right hand side of eq(5.5) is factored with respect to variables $\boldsymbol{r_1}$ and $\boldsymbol{r_2}$, eq(5.5) represents the cross spectral density as a series of spatially coherent wave fields, contributing as self-coherent, mutually incoherent modes, all of the same frequency ω. The expansion of cross spectral density to a series of single modes is the so-called **Coherent Mode Representation** method.

Depending on the type of radiation sources to be studied, diverse sets of coherent modes are introduced to describe the cross spectral density entirely[101, 102, 103]. The mode decomposition approach might be of practical use to determine pseudo-stationary statistically sources such as well-known Gaussian radiations generated by synchrotrons.

Therefore, further insight into the concepts of partially coherent pulses may be provided by a more generalized method which would be independent of the modes representation and able to treat the mutual mutual optical intensity or cross spectral density determination as a 2D problem as well.

5.1.2 Generalized Schell's theorem

As an alternative approach to deal with the evolution of partially coherent wave fields, a technique for the determination of the radiation pattern of a partially coherent illuminated aperture was introduced by Schell, known as **Schell's theorem**, which connects the far-field diffracted intensity of an aperture to it's geometrical structure and the coherence function of the illuminating wave field at the aperture position[104]. As such, it was an important and successful result for the calculation of the intensity pattern and associated power of antenna radiations in situations involving partially coherent radiations. It was shown in([105]) that Schell's theorem can be applied even in the Fresnel regime without the need for far-field condition to apply. The foregoing definition of the mutual optical intensity in the Schell's theorem is written,

$$J(\boldsymbol{r_1}, \boldsymbol{r_2}) \;=\; \psi(\boldsymbol{r_1})\psi^*(\boldsymbol{r_2})\gamma(\boldsymbol{r_{1\perp}} - \boldsymbol{r_{2\perp}}) \tag{5.7}$$

where $\psi(r)$ is a description of rms amplitude over the aperture extent and γ is termed as the normalized spatial coherence function.

The propagation of mutual optical intensity from a plane at z = 0 to a given plane located at z within the paraxial approximation is straightforward to obtain,

$$J(\rho_1, \rho_2, z) = \frac{1}{(\lambda z)^2} \exp(i\frac{k}{2z}(\rho_1^2 - \rho_2^2))$$
$$\iint J(\rho_1', \rho_2', 0) \exp(i\frac{k}{2z}(\rho_1'^2 - \rho_2'^2)) \exp(i\frac{k}{z}\boldsymbol{\rho_1}.\boldsymbol{\rho_1'}) \exp(-i\frac{k}{z}\boldsymbol{\rho_2}.\boldsymbol{\rho_2'}) d^2\rho_1'\, d^2\rho_2' \quad (5.8)$$

where $\rho = (x, y)$. The geometry followed are depicted in fig.(2.1). The mutual optical intensity leaving the aperture is a direct multiplication of $J(\rho_1, \rho_2, 0)$ with the mutual amplitude function of aperture $A(\rho_1).A^*(\rho_2)$. The detailed calculation of the mutual optical intensity and intensity associated have been presented in[105]. As a modification of the problem, here the mutual optical intensity propagation of a highly localized partially coherent wave field is calculated such that the quadratic terms of eq(5.8) contribute in a short range extent. Therefore, one can recast eq(5.8) by an explicit usage of the coherent function,

$$J(\rho_1, \rho_2, z) = \frac{1}{(\lambda z)^2} \exp(i\frac{k}{2z}(\rho_1^2 - \rho_2^2))$$
$$\iint \psi(\rho_1')\psi^*(\rho_2')\gamma(\rho_1' - \rho_2') \exp(i\frac{k}{2z}(\rho_1'^2 - \rho_2'^2)) \exp(i\frac{k}{z}\boldsymbol{\rho_1}.\boldsymbol{\rho_1'}) \exp(-i\frac{k}{z}\boldsymbol{\rho_2}.\boldsymbol{\rho_2'}) d^2\rho_1'\, d^2\rho_2', \quad (5.9)$$

where ψ is termed as the complex wave field and γ the coherence function. $|\psi|$ can be interpreted as the wave amplitude for the fully coherent condition of $J(\rho_1', \rho_2', 0)$ where the intensity is $I(\rho', 0) = |\psi(\rho', 0)|^2$ and $\gamma(\rho_1' - \rho_2') = 1$. Substituting a pair of new coordinates as $\Delta\rho = \rho_1' - \rho_2'$ and $\rho_{av}' = \frac{\rho_1' + \rho_2'}{2}$ in eq(5.9), one can represent the intensity at plane z as,

$$I(\rho, z) = \frac{1}{(\lambda z)^2} \iint \psi(\rho_{av} + \frac{1}{2}\Delta\rho) \exp(i\frac{k}{2z}(\rho_{av} + \frac{1}{2}\Delta\rho)^2)$$
$$\psi^*(\rho_{av} - \frac{1}{2}\Delta\rho) \exp(i\frac{k}{2z}(\rho_{av} - \frac{1}{2}\Delta\rho)^2)\gamma(\Delta\rho) \exp(i\frac{k}{z}\boldsymbol{\rho}.\boldsymbol{\Delta\rho}) d^2\Delta\rho\, d^2\rho_{av}, \quad (5.10)$$

where $\rho = \rho_1 = \rho_2$. The integrands can be reformed as an auto-correlation term convolving with the Fourier transformation of γ,

$$I(\rho, z') = |\frac{i}{\lambda z'} \int \psi^*(\rho'') \exp(i\frac{k}{2z'}(\rho - \rho''))^2 d^2\rho''|^2 \otimes \int \gamma(\Delta\rho) \exp(i\frac{k}{z'}\boldsymbol{\rho''}.\boldsymbol{\Delta\rho}) d^2\Delta\rho \quad (5.11)$$

The first term in the right hand side of eq(5.11) implies the Fresnel propagation of a coherent wave field and the latter represents the Fourier transform of the γ function. Eq(5.11) can be represented in an alternative format that describes a partially coherent intensity in terms of an associated fully coherent intensity propagated by the Fresnel formalism and Fourier transformation of the coherence function of the source as follows,

$$I_p = I_c \otimes \mathcal{F}(\gamma), \tag{5.12}$$

where I_p and I_c are the partially coherent and coherent intensity respectively, and $\mathbb{F}$ is the Fourier transformation. When $\frac{k}{2z'}\rho^2 \ll 1$ and $\frac{k}{2z'}\rho''^2 \ll 1$, the auto-correlation term converts to the Fraunhofer propagation of the wave field, reproducing the original representation of the Schell's theorem in the far-field regime.

Alternatively, in the near field region $\frac{k}{z'}\boldsymbol{\rho''}.\boldsymbol{\Delta\rho} \gg 1$ and, the Fourier integral responds to the exponential term as,

$$I(\rho, z') = |\frac{i}{\lambda z'} \int \psi^*(\rho'') \exp(i\frac{k}{2z'}(\rho - \rho''))^2 d^2\rho''|^2 \otimes \gamma(\rho). \tag{5.13}$$

Schell's approach is a general representation of the modal decomposition method which tentatively expresses the partially coherent wave field as a pair of physically understandable terms without a need to choose a suitable basis to decompose the cross spectral density according to its properties and geometry of the optical pipeline given. In this chapter we will treat the evolution of a partially coherent wave field as it is described by Schell's theorem.

5.2 A general version of an iterative phase retrieval algorithm for partially coherent radiations

As shown in the preceding section, the partially coherent diffraction pattern is no longer the modulus of the diffracted wave field which results in there being no physical localized wave field that simultaneously satisfies the modulus and real space constraint. Depending on the degree of coherence, the iterative algorithm, as seen in the previous chapter, might diverge or contain many undefined artifacts. The symptoms of the algorithm's failure to converge and the expectation of lower coherence in the case of the FEL running in the so-called strong compression regime motivate an interest to improve the algorithm developed such that it retrieves the effective wave field for partially coherent radiation along with the coherence function by taking advantage of Schell's theorem.

Following the geometry shown in fig.(2.1), the intensity at the detector plane is a convolution of the propagated coherent intensity and the Fourier transform of the coherence function at the image plane. So, if one could deconvolve the right hand side of eq(5.12), it would result in finding separately the coherence function and the coherent wave amplitude at the detector plane. Furthermore, the coherent wave field can be retrieved using the algorithm developed in the previous chapter. Here as a clarification, the phase of a partially coherent wave is treated as that associated with the coherent wave field to be reconstructed. In other words, when a wave field is expressed as an expansion of mutual modes the phase of the dominant mode is ascribed as the physical phase of the wave field.

To start the retrieval algorithm, intuitively we would employ a deconvolution routine with no information of functions convolved with each other. When both I_c and γ are unknown and desirable to be resolved, the problem is a so-called Blind Deconvolution. It is an ill-posed and non-convex problem which might return an infinite number of solution for a given intensity. In general, a blind deconvolution algorithm practically consists on an iterative scheme which optimizes itself in each iteration by improving the initial guess of the coherence function given to the algorithm[106]. A close guess would bring a faster convergence while a completely random start might diverge altogether or stagnate quickly to a wrong solution. Therefore, one measure of the perfectness of the deconvolution outputs is to monitor χ^2 as,

$$\chi^2 = ||I_p - I_c^{BD} \otimes \gamma_D^{BD}||, \tag{5.14}$$

which should monotonically decrease with an increasing number of iterations. Here, BD is an abbreviation of the blind deconvolution and γ_D refers to the coherence function at the detector plane.

On the other hand, the Lucy-Richardson algorithm (LC) can be employed to iteratively retrieved a numerical estimate of γ_D using the measured intensity I_p, and a combination of current and previous estimate of the coherent intensity, $I_c^{\Delta j} = I_c^{j+1} - I_c^j$[107]. The iterative scheme follows as,

$$\gamma_{DL}^{j+1} = \gamma_{DL}^{j}(I_c^{\Delta j} \otimes \frac{I_p}{I_c^{\Delta j} \otimes \gamma_{DL}^{j}}) \tag{5.15}$$

where DL index indicates the **D**etector coherence function reconstructed using **L**C algorithm.

Therefore, as an alternative measure one can compare the final γ_D^{BD} and γ_{DL}. The difference between those γs is minimized when the blind deconvolution converge to the exact solution, otherwise the retrieved γ_{DL} significantly deviates from γ_D^{BD}. A numerical simulation in the following section will illustrate this argument.

Here we introduce $O_{P\to C}$ as the deconvolution operator taking in the measured intensity and determining the coherent intensity, as well as the coherence function. So, the algorithmic steps to retrieve partially coherent measured pulses can be respectively summarized as an initialization level, the main body, and a feedback level to compare the coherence functions (see **Algorithm 1**). The main body straightly follows from the instruction described in detail in the previous chapter and refers to **Algorithm 0**. The new algorithm begins with a guess wave field of amplitude $\sqrt{I_c^{BD}}$ and returns iteratively the exact ψ_{CE4} associated with the measured data.

5.3 Numerical Modeling

As a simple picture, the partial coherence property is expected to manifest itself as a blurred measured diffraction pattern at the detector plane. So, identical to the steps we followed in chapter 4, a stochastic wave field with a phase curvature of z_{01}, propagates from the aperture plane of 5 mm in diameter, to the intermediate plane, located 2.054 m downstream of the elliptical mirror. Then, we assign a coherence function for the detector

Algorithm 1 Partially coherent wave field recovery

Begin

- *Initialization level*
  1. $O_{P\to C}(I_{PE_4}) \to (I_{CE_4}, \gamma_{E_4})$
  2. If $\lim_{iteration\simeq O(10^2)} \alpha = \|I_{PE_4} - I_{CE_4} \otimes \gamma_{E_4}\| \simeq 0$
     $\to I_{coh} = I_{CE_4}$ and $\psi_{CE_4^{guess}} = \sqrt{I_{coh}}.\exp(i\phi_{initial})$

- *Main body*
  1. **Algorithm 0** $_{j=1}^{N}(\psi_{CE_4^{guess}})$
     * While ϵ monitors convergence,

     If Mod(j,10) = 0 ,
     $\gamma_{DL}^{1} = \mathrm{f}(\rho) \in \mathbb{R}^2$
     $\gamma_{DL}^{j+1} = \gamma_{DL}^{j}(I_c^{\Delta j} \otimes \frac{I_p}{I_c^{\Delta j} \otimes \gamma_{DL}^{j}})$

- *Feedback level*
  1. $\beta^{j+1} = ||\gamma_{DL}^{j+1} - \gamma_{D}^{BD}||$
     If $\beta^{j+1} - \beta^{j} > 0$
     Break
     Reinitialize

- Once the simultaneous convergence of β and ϵ is achieved the algorithm is stopped.

end

plane which enables the use of eq(5.12) to find the partially coherent intensity. In fig.(5.1.a-b) the partially coherent simulated intensity, as well as the coherence function are depicted. The partial coherence suppresses the coherence fringes as can be seen from a comparison of fig.(5.1.a) and fig.(5.1.c) . However, a ±10% variation in the FWHM of the coherence function did not dramatically change the partially diffraction pattern such that the correlation between the changed and unchanged functions yielded a value of 95%. As soon as the variation of FWHM exceeds ±10%, the pairwise correlation reduces significantly. Consequently, it is observed that the recovery of the coherence function carries an uncertainty of less than 10% in the FWHM or equivalently in the coherence length to be resolved.

$O_{P\to C}(I_{PE_4})$ was initialized by an off-centered Gaussian function as the initial coherence function suggestion with a FWHM of three times larger than the simulated one. It was seen that the blind deconvolution algorithm is sensitive to the initial parameter, and might not converge if the input is far away from the real solution. However, a start guess close to the final solution would result in retrieving the coherence function easily. A start guess of the coherence function may be understood from radiation simulations.

Fig.(5.2) displays the evolution of α, β and ϵ after 300 iteration for a successful re-

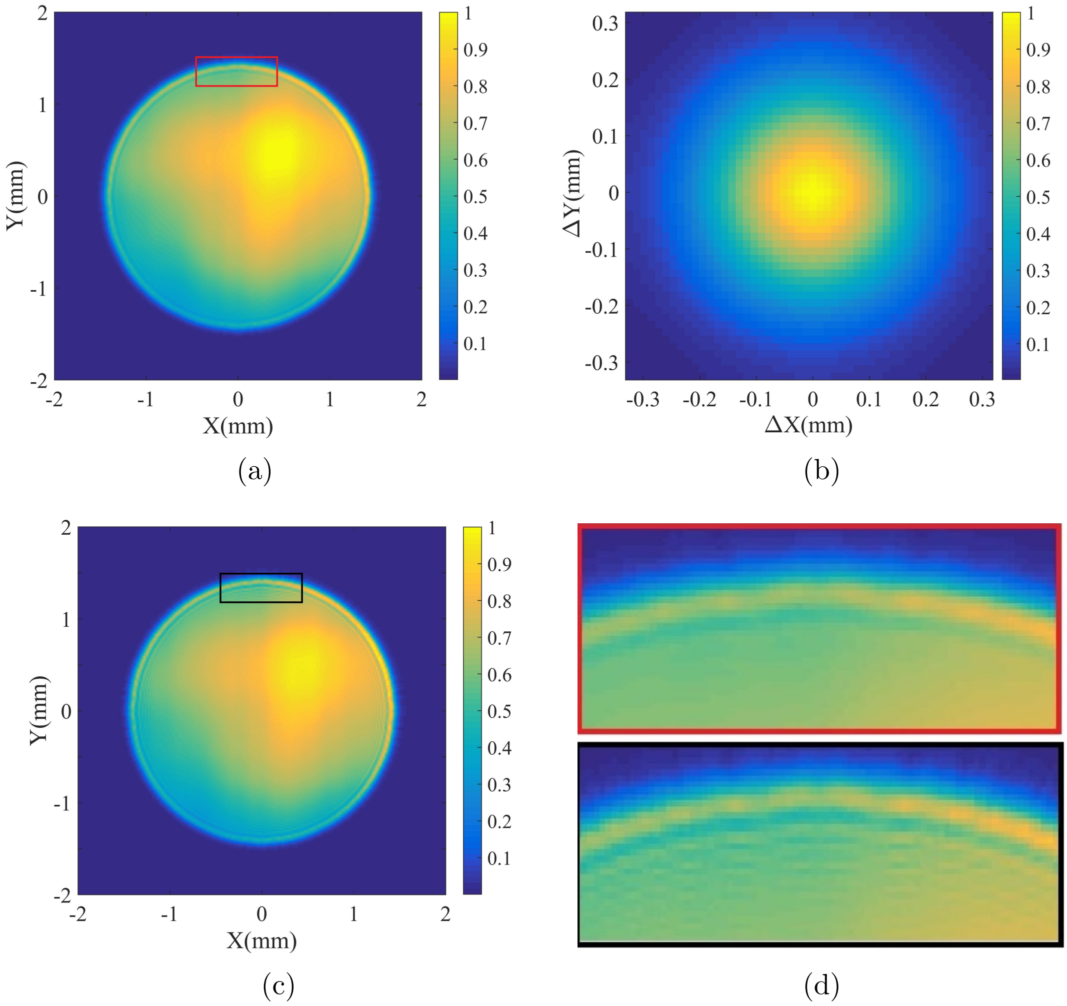

Figure 5.1: Partially coherent wave field simulation. (a) displays partially coherent diffraction pattern of a 5 mm aperture 3.2 m upstream of the detector. (b) the coherence envelope as a function of the relative lateral coordinates ($\Delta\boldsymbol{\rho}$). (c) represents the coherent intensity associated. (d) shows that the coherence fringes in (c) are surpassed in (a) as the influence of the partial coherence. The images are 1024×1024 pixels with 23 μm square pixels. The wavelength is 14.7 nm.

construction. Consequently, the result of the main body are presented in fig.(5.3). It is seen that the coherent intensity and coherent function both are reconstructed accurately. The phase reconstruction at the aperture plane reflects an error of less than 1% in the reconstruction of the phase. As a remaining question to find the exact place of the image plane, it would be desirable to compare the caustics of the reconstructed coherent wave field and the partially coherent wave field obeying eq(5.13). As seen in fig.(5.3.c) both coherent and partially coherent wave field's intensity caustic distribution result in finding a unique image plane position. Simply, the delivery of the source image through the optical pipeline is not affected by the presence of the coherence function, and the image plane position can be precisely determined as followed in the previous chapters. Determining the position of the image plane, the source image FWHM can be calculated using the second momentum method. The ratio of the coherence function FWHM to the intensity distribution FWHM would reflect a measure of the average degree of coherence, even though an uncertainty in order of 10% in reconstructing the coherence function unavoidably exists.

The normalized degree of coherence at the image plane is depicted in fig.(5.4). It releases a average degree of coherence of 44% which is in general agreement with the ideal value considered in the simulation as 48% (the ratio of FWHMs of simulated functions at the detector plane), given the expected uncertainty in the recovered degree of coherence.

A stagnation state was found as a probable situation that may occur when a noise level of more than 8% was added to the diffraction pattern. The stagnation is recognized by simultaneous monitoring of the convergence of error metrics and the mean difference of the reconstructed and simulated diffraction pattern. As discussed in the previous chapter, the mean difference would be in order of 10^{-3} for a successful reconstruction. Adding noise levels of 8%, 10% and 15% to fig.(5.2.a) resulted in finding the mean differences of 0.02, 0.1, 0.3 while the error metrics converged.

It is observed that even in the presence of the uncertainty associated with the recovery of the coherence function, the successful wave field reconstruction satisfies both conditions of the error metrics convergence and a mean difference in order of 0.003 indicating a reliable reconstruction. Therefore, it can be concluded that the method provides a reliable measure of the wave field and an approximation of the coherence with an expected level of the uncertainty. The mean difference between the partially coherent intensity reconstructed with the highest and lowest error level of the coherence function recovered never exceeds a value of more than 10^{-3}.

5.4 Overview of partially coherent wave field reconstructions

Since the general algorithm can accommodate partial coherence and simultaneously determine the coherence function, all pulse categories are expected to be fully reconstructible with this general algorithm, regardless of the degree of coherence associated with them. In the following section the results of A3 and A4 regimes will be presented primarily, since the explicit lack of convergence was seen when they were applied with the coherent version of the algorithm in the previous chapter. A comparison between the general and coherent algorithm to reconstruct the pulses of A1(2) regime will follow in the second section.

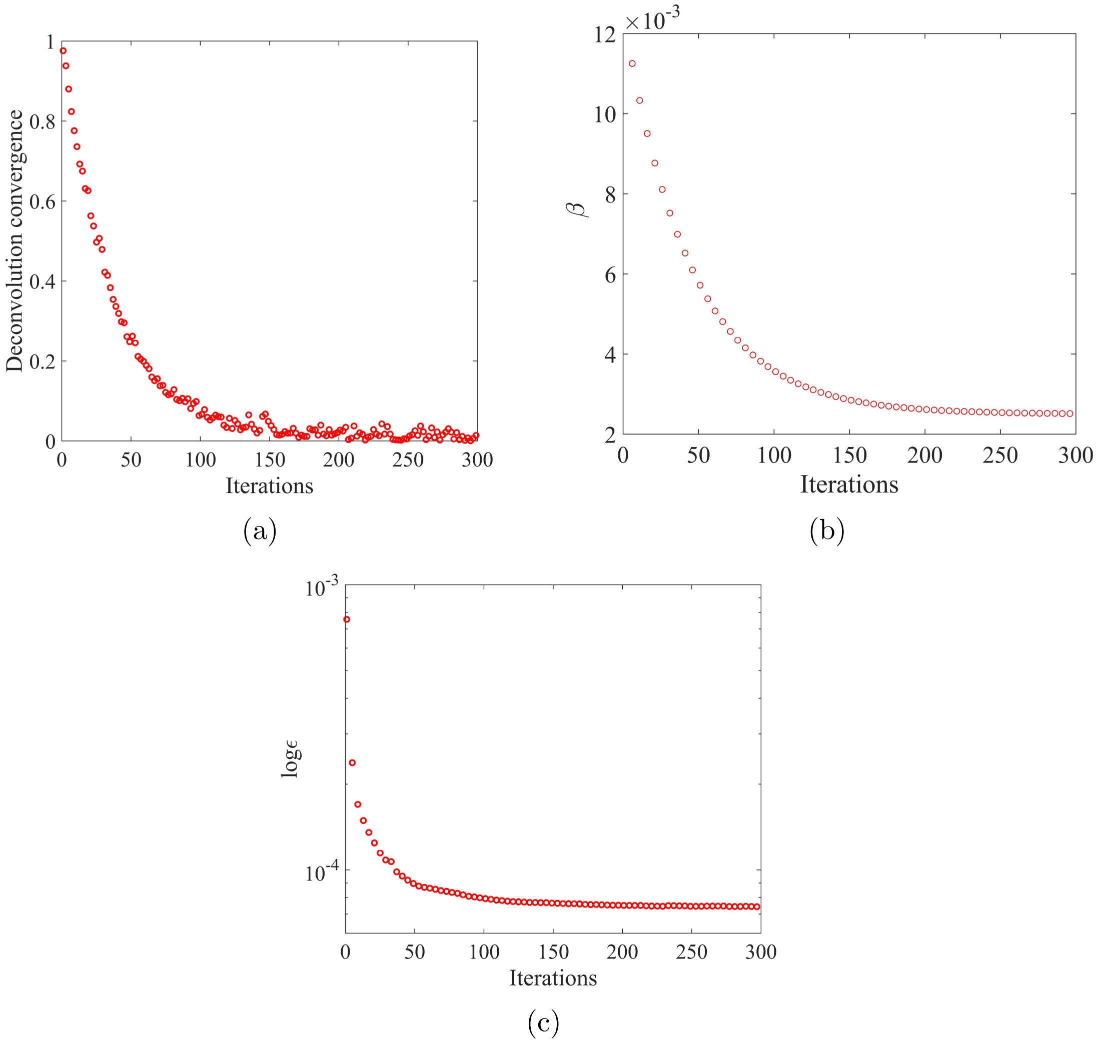

Figure 5.2: Evolution of convergence parameters. In (a) α is represented in a normalized fashion as it is conventionally implemented to most of deconvolution routines. The absolute difference between γ_{DL} and γ^{BD} iteratively decreases to a steady state in (b). (c) shows the convergence of **Algorithm 0** error metric on a logarithmic scale. The simultaneous convergence of all three parameters conclude a successful reconstruction.

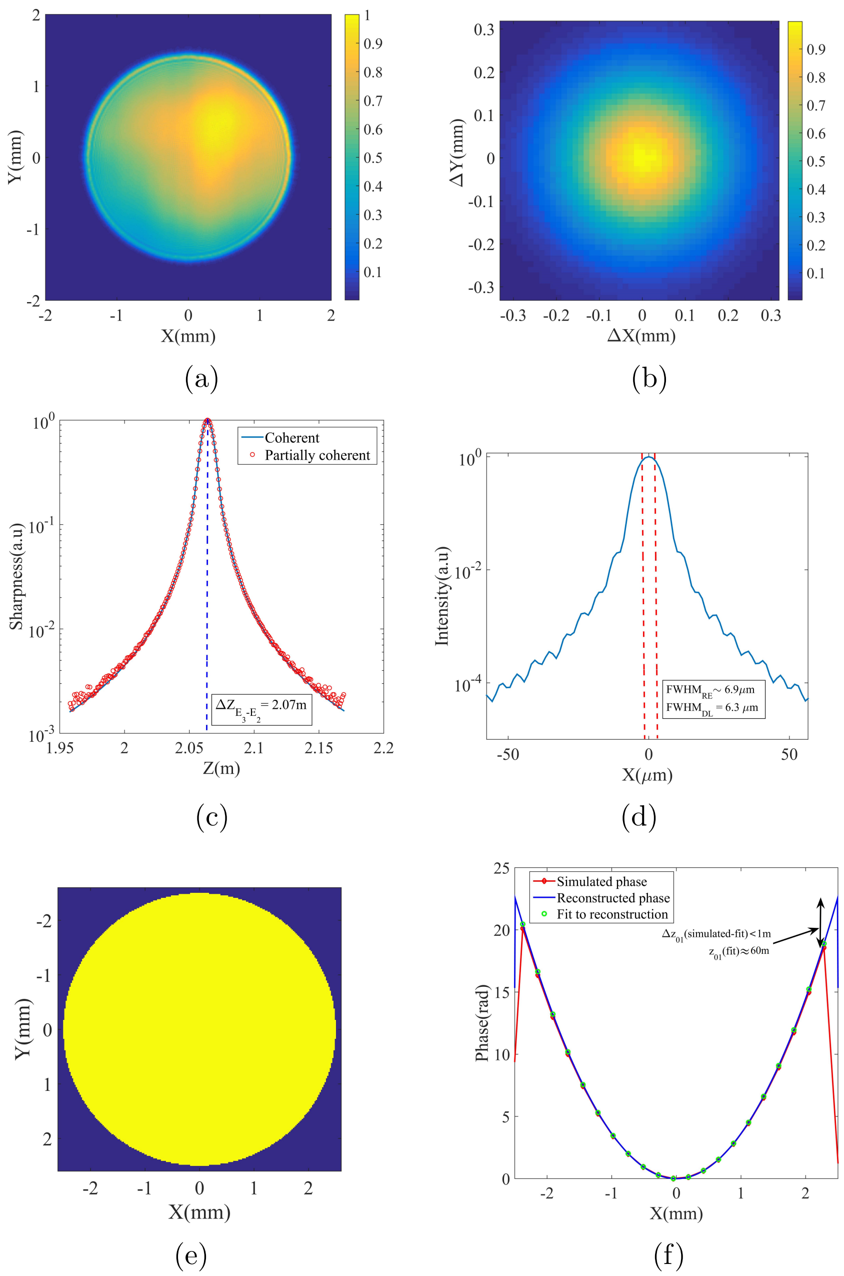

Figure 5.3: Implementation of the generalized phase retrieval algorithm for a partially coherent wave field shown in (a). The difference between Lucy-Richardson and blind deconvolution reconstruction was not resolvable by eye so only one of them is represented in (b). In (c) the red dots are the sharpness distribution in a vicinity of the intermediate plane when eq(5.13) applies. (d) shows the partially coherent intensity distribution at the image plane which reflects a larger image size ($FWHM_{RE}$) compared to the diffraction limited ($FWHM_{DL}$) value. The extent of the simulated aperture is completely recovered using the shrink-wrap algorithm within the main body of the generalized algorithm. The reconstructed phase reasonably fits the simulated phase yielding $z_{01} = 60$ m with an error of less than 1 m.

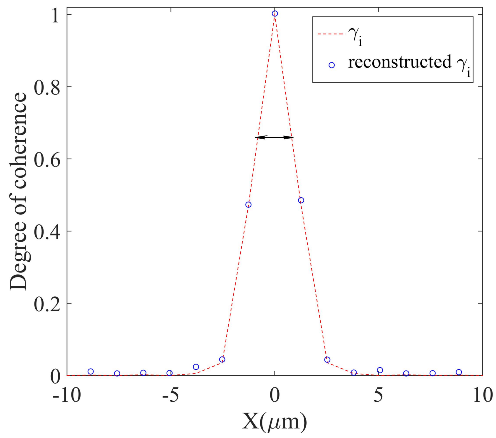

Figure 5.4: Degree of coherence. dashed lines present the Fourier back transformation of γ_D^{DB}, and the blue circles show the reconstructed coherence function employing the Lucy-Richardson algorithm.

5.4.1 Implementation to A3 and A4 regimes data

As an exception, as shown in fig.(5.5.a), the measured diffraction data for the case of 10 mm aperture size in A3 regime shows a tilt of the aperture which unfortunately avoids to apply the specified real space constraint into the reconstruction. And also, due to the high level of noise, the deconvolution process applied to those data failed to converge fig(5.5.b-d). Therefore, this set of data has been excluded from the analysis.

In fig(5.6), we display an example of complex wave field reconstructions for the A3 regime using an aperture of 3 mm in size. For the other variants, the same procedure was followed. Since many pulses were analyzed for each data set, the average of parameters analyzed over the ensembles is reported here.

The results reflect a series of successful reconstructions converging reliably and relatively fast. The deconvolution algorithm was initialized by a Gaussian function with a FWHM equal to the 40% of the aperture size. The choice of a Gaussian function led the deconvolution algorithm to converge to the solutions perfectly close to the reconstructed coherence function using the Lucy-Richardson algorithm. A random choice to initialize the deconvolution resulted in a lack of convergence or trapping in a stagnation state. Therefore, the initialization without any knowledge of the coherence function might be a bottleneck preventing to start the whole algorithm. It should be noted that as the result of radiation simulations, a Gaussian function is used as a reasonable guess of the coherence envelope. The main body of the algorithm was initialized as described in the previous chapter. For each data frame, 20 trials were compiled to monitor the reproducibility of the algorithm. A standard deviation of less than 8% was observed in ϵ_{final} for all data frames reconstructed.

The results show a size increase of the source image in comparison with those obtained through A1 and A2 regimes. A small shape variation and lateral positional displacement of the source image was observed as it is indicated by a red dashed line to illustrate the

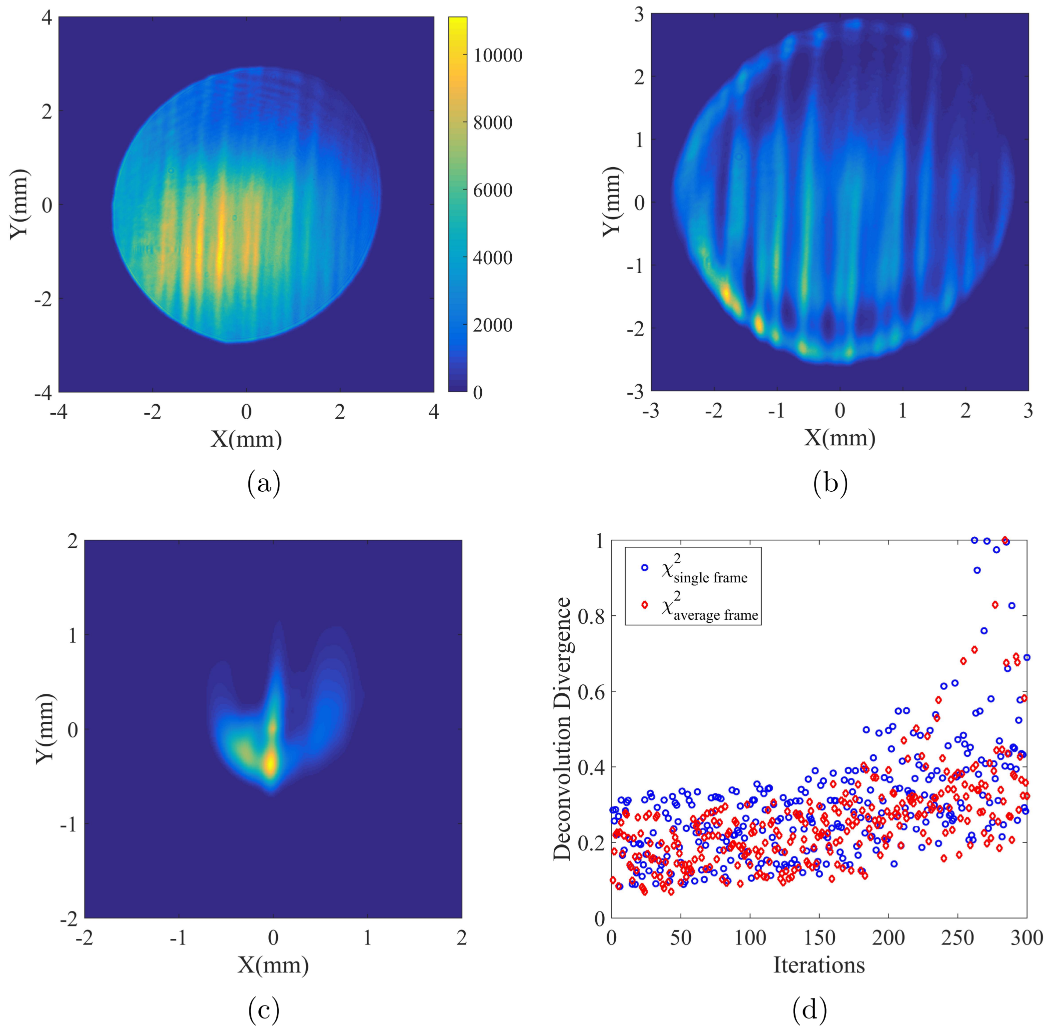

Figure 5.5: Failure to reconstruct the wave field with a 10 mm aperture size in the A3 regime (strong compression- 4 undulators). (a) shows an example of the measured data which clearly illustrates the effect of the aperture misalignment to the diffraction pattern. The wave field was not constrained well enough. Therefore, the reconstructed coherent intensity and coherence function could not be retrieved successfully as shown in (b,c). The divergence of the single frame and average pulse are shown in(d).

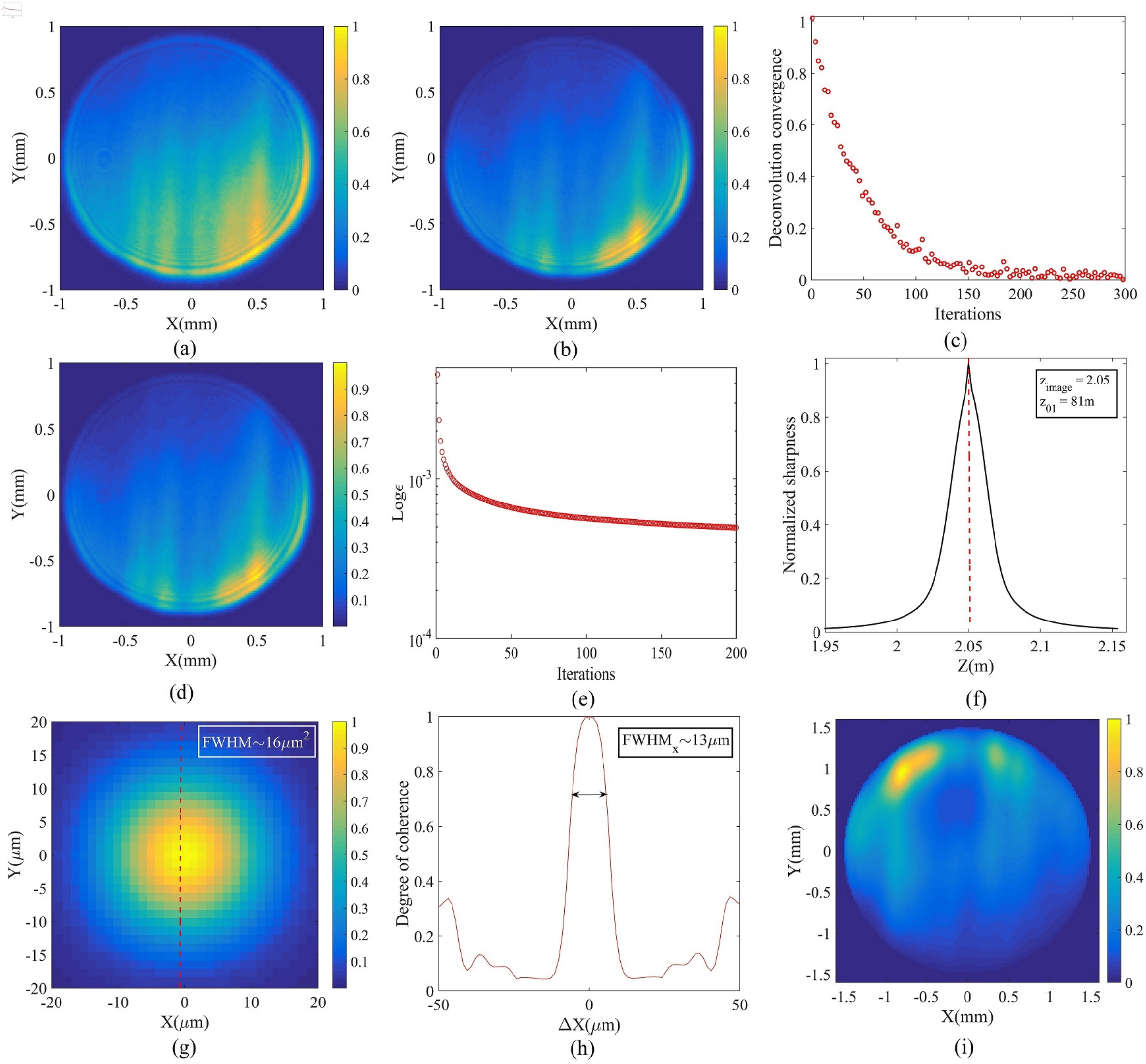

Figure 5.6: Partially coherent single-shot wave field reconstruction applied to A3 regime using a 3mm aperture.(a). the measured intensity, (b). deconvolved intensity, (c). deconvolution convergence, (d). reconstructed coherent intensity, (e). evolution of the reconstruction error metric, (f). the normalized sharpness, (g). the intensity distribution at the image plane, (h). the degree of coherence obtained at the image plane, (i). the partially coherent intensity at the aperture plane as the convolution of the reconstructed coherence intensity and geometrically scaled coherence function. Note that the main body of the algorithm was given 200 iterations to reconstruct the coherent wave field, as it was conceived to be enough by the convergence behavior of the algorithm seen in the previous chapter.

off-center positions and rotations resolved. In fig.(5.7) the statistics of change in FWHM of the source image and coherence functions for A3-A4 using 5 mm aperture are shown. The average degree of coherence for both regimes statistically varies. More accurately speaking, if the discussed uncertainty to the reconstruction of the coherence function was considered, which is comparable with the standard deviation of the fluctuations observed, the average degree of coherences should be treated as quasi-dynamic parameter with the smooth fluctuations around its mean value. The reconstructions mostly determined symmetric coherence functions such that the difference in the lateral FWHMs is fairly negligible. Hereafter, the 1D profile of the coherence function is plotted and we refer to FWHM as the value assigned for both lateral directions.

Table(5.1) summarizes the coherence degree for A3-A4 regimes and different aperture sizes. As seen, the coherence degree approaches 73% in the A3 regime when the smallest aperture was used while the situation for A4 shows a 5% decrease of the coherence degree. A4-10 mm reflects the lowest value of the coherence delivered by the radiation setups. Here, it should be noted that selecting the consistent subset of data enables us to monitor the consistent performance of the source.

Table 5.1: **Overview of the coherence degree of the pulses delivered via A3-A4 regimes. The data shown were resolved using the general algorithm. A3-10 mm data set, as explained previously, was excluded from the data analysis.**

Case	Average source image size(H×Vμm^2)	Coherence degree(±10%)
A3 - 5 mm	11.8×11.3	73%
A3 - 3 mm	16.8×16.4	78%
A4 - 10 mm	9.8×10.1	70%
A4 - 5 mm	13.9×14	72%
A4 - 3 mm	17.7×17.7	75%

The normalized sharpness of the reconstructed coherent pulses identifies the focal plane, and hence reflects the longitudinal source position displacement within the undulator segments. For different bunches (fig.5.8), the source fluctuates in a range of the order of one undulator length with a standard deviation of approximately half an undulator length. Theses longitudinal fluctuations are in general agreement with those determined in the previous chapter.

In fig.(5.9) the peak-to-valley (p-v) and rms error of the reconstructed phases (of the detector plane) for both radiation regimes when a 5 mm aperture was considered are listed. The reconstructed phases were unwrapped and the first 7 Zernike polynomials were subtracted. In general, the results yield a larger phase variation in A4 regime compare to A3. We recall that in the previous chapter the A2 regime showed a higher level of phase variation in comparison to A1. It can be suggested that increasing the active undulator segments may result in observing a higher statistical phase change.

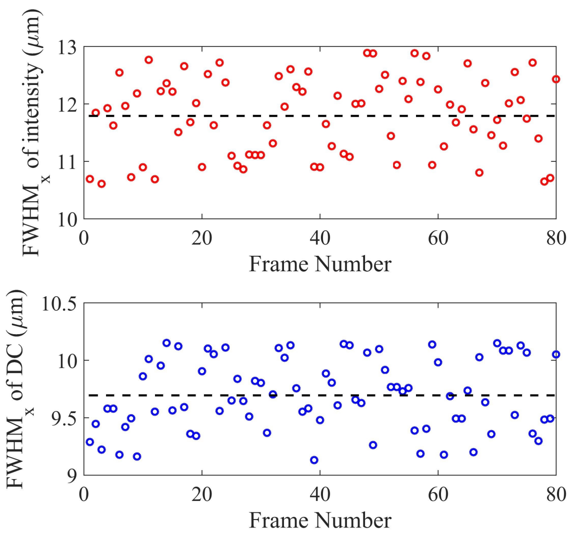

(a)

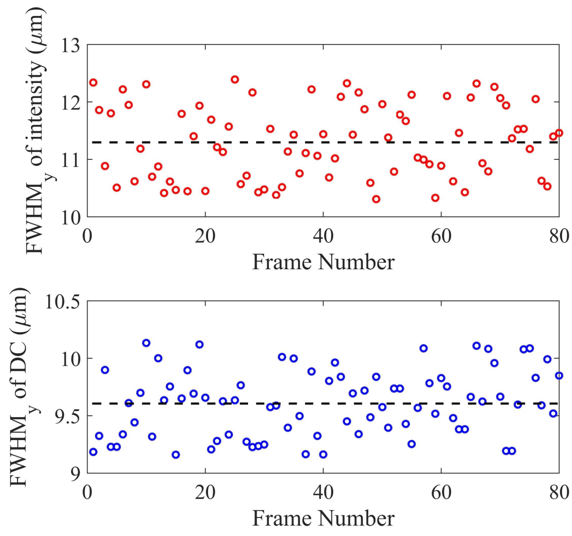

(b)

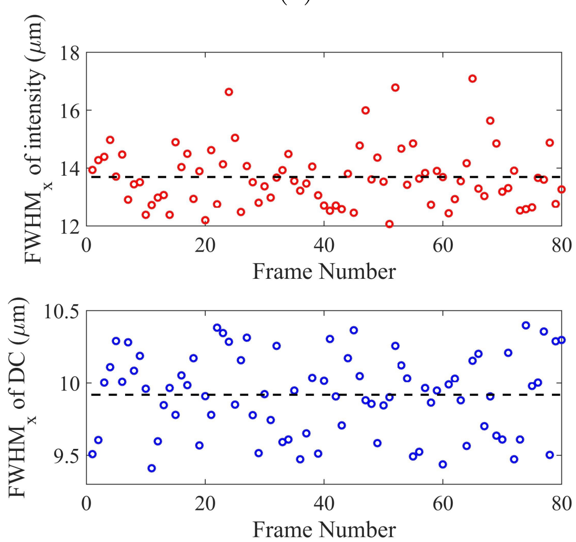

(c)

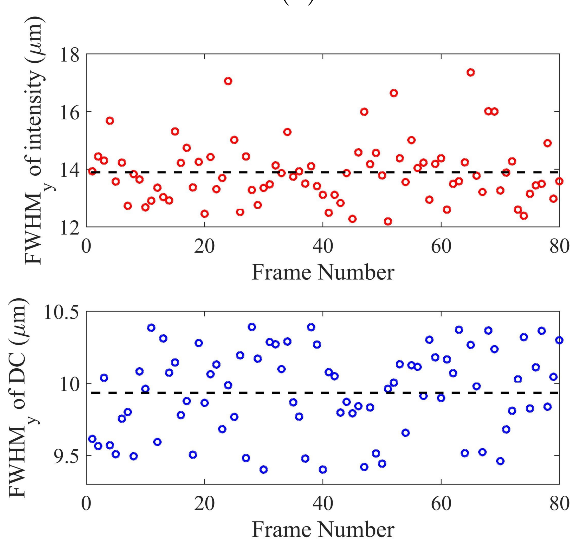

(d)

Figure 5.7: Variation in image size and coherence function using. Here DC abbreviates the degree of coherence. (a-b) reflect an average image size (FWHM) of $11.8_h \times 11.4_v$ μm^2 and an average coherence function size (FWHM) of $9.6_h \times 9.7_v$ μm^2, for the A3 regime using a 5 mm aperture . (c-d) present a relatively lager image size (FWHM) for the A4 regime using 5 mm aperture size, as $13.7_h \times 13.9_v$ μm^2 while the coherence function size (FWHM) $9.8_h \times 9.9_v$ μm^2 has been approximately preserved. The black dashed lines display the average values.

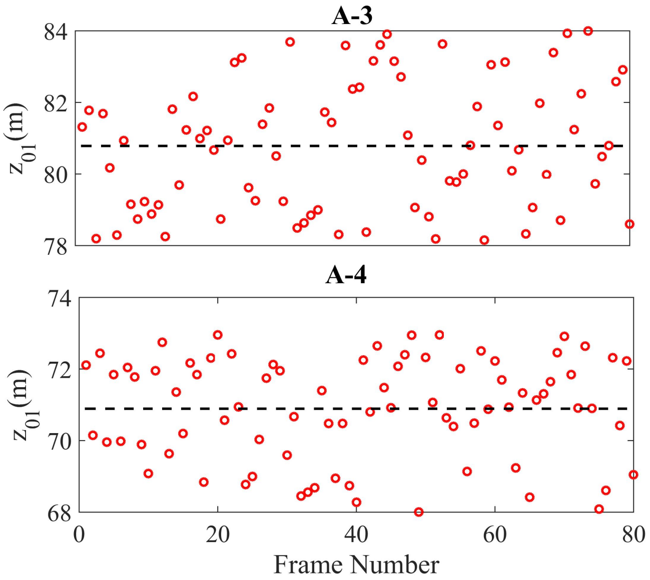

Figure 5.8: Longitudinal source positional fluctuation of A3 and A4 regimes when a 5mm aperture was applied. As seen the longitudinal source fluctuation is clearly resolved and shows an average difference of 10m (2 undulators length) between A3 and A4 regimes, supporting the results of simulations reported by FLASH accelerator sector[86]. The black dashed lines display the average values.

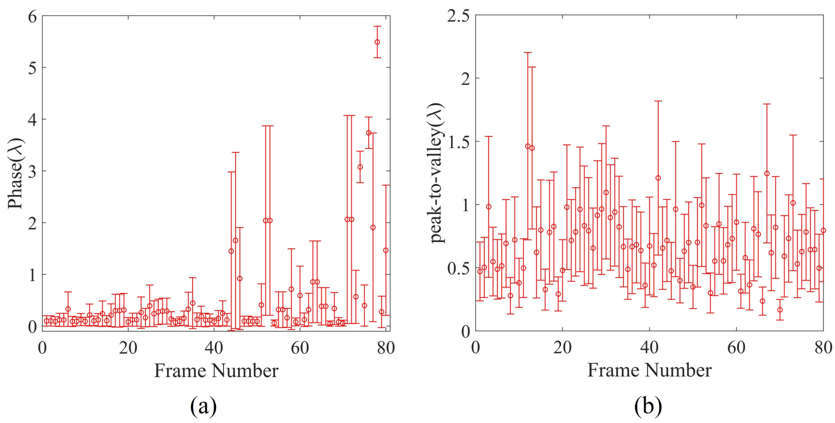

Figure 5.9: Monitoring the phase variations. For every single-shot the first 7 Zernike polynomials were subtracted from the unwrapped phase at the detector plane when a 5mm aperture was used. (a-b) show the phase fluctuations for A3 and A4 regimes respectively.

5.4.2 Implementation to A1 and A2 regimes data

In the previous chapter A1(2) regimes data were analyzed successfully using the conventional algorithm. For all pulses reconstructed, the algorithm convergence was monitored for many trials to prove the reproducibility of the results. The transition from A1(2) to A3(4) clearly illustrated that below a certain level of the coherence (when radiation are partially coherent) the algorithm has to be modified in order to reconstruct pulses measured. The successfulness of applying the **Algorithm 0** to A1(2) meant that up to a certain level of coherence the algorithm would be able to reconstruct the complex wave field of the pulses. By the knowledge of the preceding section, we can assert that a high-level of coherence would be enough to employ the **Algorithm 0** instead of assuming a fully coherent illumination that might not be achieved practically. So, of importance and interest is to understand the cross-over point of the coherence level, defining the inevitable transition to the general algorithm.

In fig.(5.10) the complex wave field reconstruction of a frame of A1 data using both algorithms is compared. The measured intensity was used as the input of the coherent algorithm as described in the last chapter while the associated coherent intensity (here we use $\otimes$ and $\otimes^{-1}$ as the convolution and deconvolution operators) initiated the general algorithm . To meaningfully compare the results of both algorithms, the reconstructed coherent intensities of the general algorithm were convolved with the associated coherent functions at the image and aperture planes.

Both algorithms converge reliably after 200 iterations to a reproducible solution (20 trials were performed). A reduction in the error metric of 13% using the partially coherent reconstruction method compared with assuming highly coherent beam was determined. This improvement compares well with the results and explanation of the previous works on the partially coherent diffractive imaging[27] . As seen, the reconstructed image source complex wave field and aperture plane intensities display a high level of correlation between the performance of the two algorithms. The position of the image source was found to be the same in both algorithms while the general algorithm resulted in a relatively larger image size in the vertical direction ($0.2\mu m$) which manifests a negligible difference that might arise from the imperfect reconstruction of the coherence function by the blind deconvolution algorithm. The reconstructed degree of coherence at the image plane reflects a coherence degree of 82%. It is seen that applying the **Algorithm 1** or **Algorithm 0** to A1(2) resulted in a series of the same wave field reconstructions without any significant variations in the statistical parameters of the pulses.

Consequently, different pulses from A1 and A2 for 3-5-10 mm aperture sizes were compared similarly. Regardless of the aperture size, A1 pulses could be fully characterized by both algorithms with a high level of correlation between the reconstructed wave fields. The transition to A2 regimes significantly decreased the signal to noise ratio and the deconvolution process often required a high level of the noise threshold to apply. Nevertheless, the pairwise comparison of reconstructed pulses of A2 regime via both algorithms, on average, showed a correlation of 92%.

Fig.(5.11) shows the reconstructed average degree of coherence for A1 and A2 regimes. It can be determined that both regimes deliver pulses with a coherence degree of higher

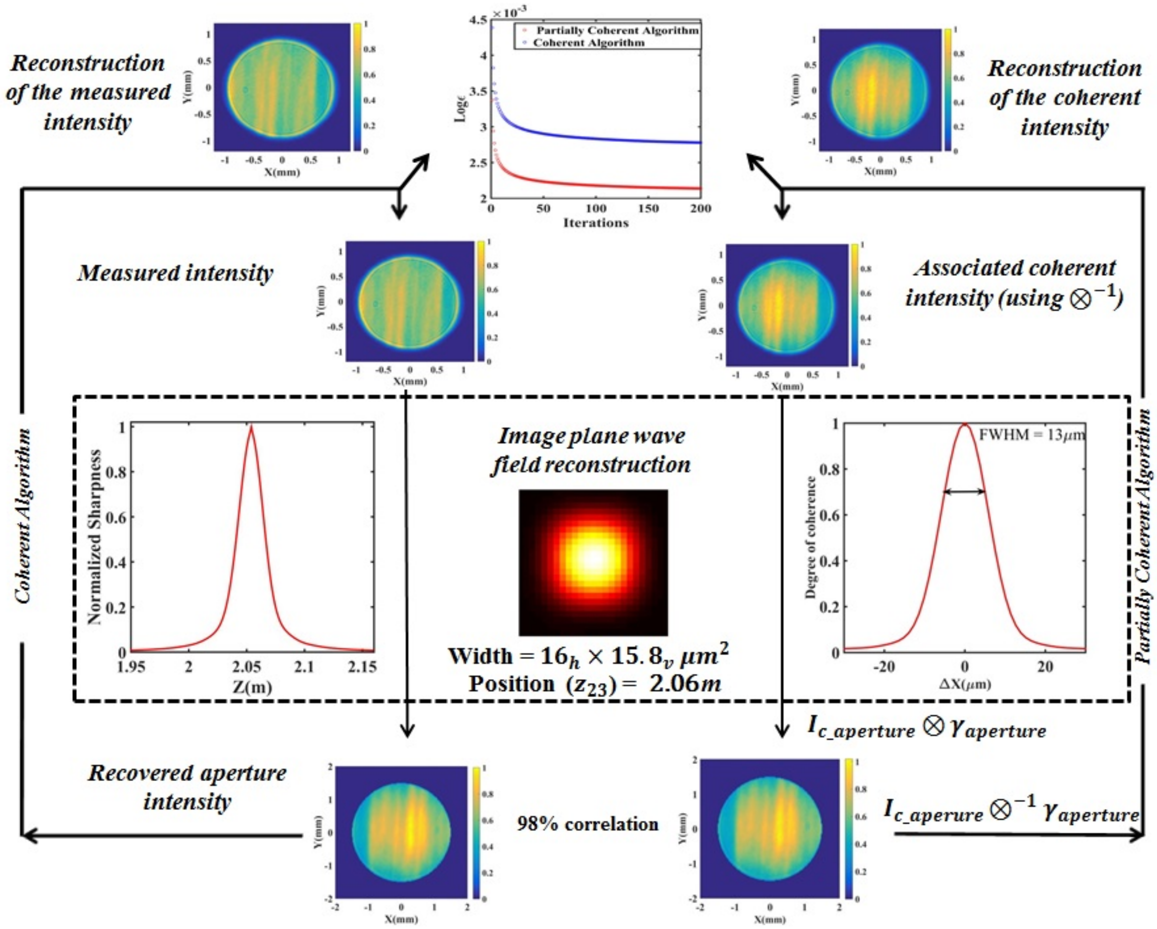

Figure 5.10: Partially wave field reconstruction applied to A1 regime using a 3 mm aperture size. A frame of data were reconstructed using the coherent (left loop) and partially coherent algorithm (right loop). As expected, due to the high coherence degree of A1 regime, both algorithms determined the same complex wave field. As an advantage of the general algorithm, the coherence function was found, yielding an 82% coherence degree. The source image size and on-axis position resolved in both algorithms are in a general agreement. Both approaches converged to a reliable solution after 200 iterations. $\otimes$ and $\otimes^{-1}$ display the convolution and deconvolution operators.

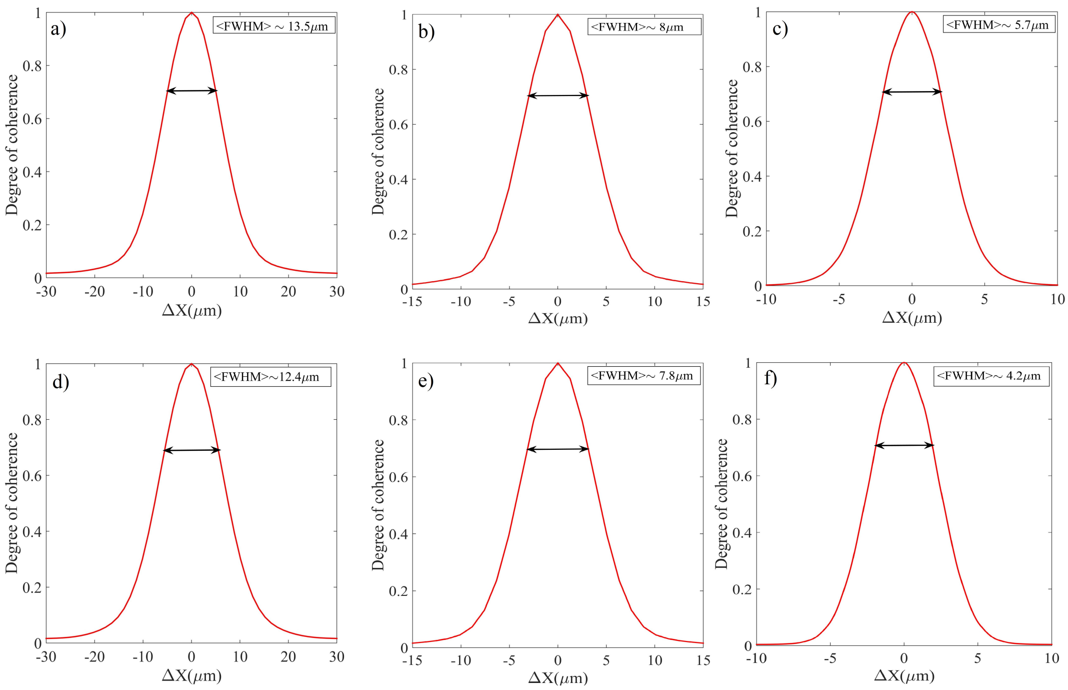

Figure 5.11: Determination of the degree of coherence at the image plane. The upper and lower rows display the reconstructed degree of coherence for A1 and A2 regimes respectively. The aperture size used increases from the left to right as 3-5-10 mm. The ratio of the average FWHMs to the source image sizes shows a high level of radiation parameters stability over the measurements periods (as shown in Table(5.2)). <> is the average (mean) over the ensemble.

than 81%. The coherence degree of A1 reflects the highest level of consistency in comparison to the other regimes, proving the stability of the radiation parameters over the measurement periods. Accordingly, Table(5.2) categorizes the coherence degrees for A1-A2 regimes using different aperture sizes. The results confirm, as the probability density function analysis showed, that A1 regime delivers the most coherent pulses compared to the other machine-aperture setups.

Our analysis shows that the cross-over governing the transition to the general algorithm is a coherence degree less than 80% associated with pulses. It was clearly shown that the partially coherent algorithm significantly improves the algorithmic convergence in every radiation case. A level less than this boundary, as shown in the previous chapter, would results in a lack of convergence. This effect is attributed to the variation-in-contribution of the γ function in eq(5.10). This shows that a slight decrease in the coherence length can drastically change the assumption of $\gamma \simeq 1$ and requires the general algorithm to be applied. Therefore, the general algorithm might be considered as a very applicable tools for the beamlines delivering pulses with lower levels of coherence. Nevertheless, we note that the success of the general algorithm strongly connects to

Table 5.2: **Overview of the coherence degree of the pulses delivered via A1-A2 regimes. The data shown were resolved using both general and conventional algorithms.**

Case	Average image size(H×Vμm^2)	Coherence degree(±10%)
A1 - 10 mm	6.72×6.77	78%
A1 - 5 mm	9.53×9.58	83%
A1 - 3 mm	16.24×16.10	89%
A2 - 10 mm	5.15×5.23	76%
A2 - 5 mm	9.55×9.5	82%
A2 - 3 mm	15.14×15.21	87%

the signal to noise ratio. A high level of noise significantly affects the BD algorithm as of seen for A3-10 mm data set. Apparently, developing a powerful tool dedicated to deconvolve noisy data with no *a prior* model or form is strongly required to facilitate the initiation of the general algorithm.

5.5 Conclusion

A general phase retrieval algorithm was developed to reconstruct partially coherent pulses delivered in the strong compression regime. The general algorithm enables the reconstruction of the complex wave fields, as well as the coherence function associated with them using the so-called Lucy-Richardson algorithm. An inevitable level of uncertainty (±10%) was determined in the reconstruction of the coherence function. It was shown that this uncertainty does not significantly change the reconstructed partially coherent pulses. The general approach yields a more reliable level of convergence, compared to the coherence algorithm, for all pulses of the different regimes, and a reasonable approximation of the coherence degree for each single-shot.

The shot-to-shot fluctuation of the source's parameters were determined, and a reasonable level of correlation was found between them. The resolved degree of coherence was in general agreement with radiation simulations. The reconstruction of the transverse degree of coherence in this chapter potentially supports the results of the simulated radiations and the assumption of considering solely A1-A2 datasets in the third chapter to apply the Hartmann wavefront sensing method. It should be recalled that the generalized imaging approach may apply to different states of a FEL machine delivering pulse with different degree of transverse coherence, if enough signal to noise ratio was achieved.

Table(5.3) presents an overview of all four regimes regarding the determined properties obtained in the previous and present chapters. A high level of correlation (abbreviated as C), more than 85%, has been observed between the intensities and respective retrieved phases, implying a similar pattern of variation through each of them regardless of the FEL machine state. As seen, aperturing the photon beam upstream of the focusing optics improves its coherence. However, a clear trade-off between the highest achievable

Table 5.3: **Comparison of the determined properties across the different radiation regimes**

	Aperture size (mm)	C(intensity and phase)	Average degree of coherence (±10%)	Average image size(μm^2) (H×V)	Average source position(m ± 2.5 m)
A1	10	0.9	78%	6.7×6.8	81
	5	0.93	83%	9.53×9.58	
	3	0.95	90%	16.2×16.1	
A2	10	0.88	76%	5.15×5.23	72
	5	0.92	82%	9.55×9.5	
	3	0.95	88%	15.1×15.2	
A3	10	0.89	74%	————	80
	5	0.93	73%	11.8×11.3	
	3	0.91	79%	16.8×16.4	
A4	10	0.87	70%	9.8×10.1	71
	5	0.90	72%	13.9×14	
	3	0.90	76%	17.7×17.7	

level of the transverse coherence and blocking more photons was observed. The focal size distribution was found as a function of the aperture size and the degree of coherence. Applying the same aperture, partially coherent pulses yielded larger focal distribution than the coherent pulses. Even a small change in the beam coherence (less than 10%) may result in 30% increase in the image size. Both algorithms developed in this thesis conclude a consistent effective source position regarding the number of active undulators independent of the bunch compression. However, the iterative scheme inherently contains a level of uncertainty to resolve the source position which is practically smaller than the gap between the undulator segments.

CHAPTER 6

Conclusion

Determining shot-to-shot fluctuations in properties of focused X-ray FEL pulses is essential for many experiments at SASE based FELs, in particular for imaging single non-crystalline biological particles. The characterization of highly focused X-ray pulses is particularly challenging due to the stochastic shot-to-shot fluctuations of the SASE process as well as a focused peak intensity that exceeds the damage threshold of any material. An approach to solve this problem is to use an iterative diffractive imaging technique applied to single far-field diffraction patterns from a highly focused beam. This method comprises an iterative phase retrieval with support and intensity modulus constraints, utilizing the spherical phase curvature of the focused beam; known as the Fresnel coherent diffraction imaging method.

Within this thesis, an extension of the Fresnel coherent diffraction imaging method to systematically characterize highly focused X-ray pulses has been proposed to the case where the support constraint can be imposed in a plane that differs from the plane of the focusing optics. This approach enables wave field characterization experiments to be performed under more general experimental conditions than previously assumed. The method has been developed to apply to a broad range of photon energy, without imposing a limit on the resolution.

Furthermore, the method has been generalized to reconstruct partially coherent wave fields delivered at FELs by taking advantage of Schell's generalized theorem in the context of partially coherent optics. In this approach, the measured intensities have been treated as a convolution of the so-called coherent intensities and associated coherence functions. This improvement enables the additional benefit of retrieving the coherence function associated with the pulses, as an additional inverse problem implemented to the coherent algorithm, with a reliable, if limited, accuracy.

The use of the coherent and generalized algorithms has been simulated by modeling the wave field characterization experiments for fully and partially coherent pulses. Both approaches predict successful single-shot wave field retrievals with reliable and reproducible convergence to a unique solution, as well as the precise determination of the source parameters. The simulations suggest that the general algorithm (partially coherent) offers an improvement in the solution reliability, at the cost of decreasing the convergence speed and noise robustness. It has been observed that the coherent algorithm retrieves the wave fields of simulated highly coherent pulses, and an apparent failure of reconstruction appears when pulses are partially coherent.

This work has demonstrated the application of the coherent and generalized algorithm to characterize single-shot FEL pulses and determine source parameters by the FLASH beamline BL2 for a variety of radiation regimes including the different electron bunch compression and a different number of active undulators. The former affects the signal-to-noise (SNR) ratio of pulses delivered, and the latter influences the coherence degree associated with pulses. Additionally, delivered single-shot X-ray pulses have been expected to show different levels of beam instability, as well as chaotic variations of the intensity and phase.

The imaging technique has been benchmarked against the well-established Hartmann Wavefront Sensing method for soft X-ray pulses of FLASH. The Fourier Demodulation method has been introduced as a fast, and precise approach to analyze data measured of wavefront sensors in Fourier space. A high level of correlation between the properties of the reconstructed wave fields and source parameters has been observed using both methods. The results have shown the shot-to-shot fluctuations of the source parameters within the subsets and between the different subsets of different regimes.

It has been demonstrated that the generalized algorithm resolves the coherence properties of the measured pulses and effective source position such that the statistical average of those parameters compares well with the theoretical expectation. The identification of effective source position potentially removes the conventional assumption of a (nearly) planar illuminating probe to be characterized and suits both algorithms for pulse characterizations of short beamlines regardless of the coherence degree.

The method generalizes well to the hard X-ray regime which is a distinct advantage compared to other methods. The method offers the possibility to enable wave field characterization to the upcoming the European XFEL, with the highest resolution possible and potentially fast, online feedback for users to optimize and the understand radiation delivered. The unambiguous separation of the wave field and coherence function may assist the precise conduct and interpretation of novel experiments, especially single particle imaging experiments at the SPB/SFX instrument.

Acknowledgements

First, I would like to express my sincere gratitude to my immediate supervisor, Dr. Adrian Mancuso, for the invaluable learning opportunity he gave me to work under his supervision. Your guidance and continuous support equipped me with knowledge and experience that will help me in my career. I would like to thank Dr. Thomas Tschentscher and Prof. Dr. Henry Chapman for agreeing to be my supervisors. I am grateful for the generous time given to discuss my research activities and for the insightful comments and advice.

A special thank you goes to Dr. Klaus Giewekemeyer and Dr. Patrik Vagovic for their tireless efforts to stimulate my research activities, sharing brilliant ideas and for encouraging me to look forward to all situations. I am grateful for your precious advice and discussions during the beamtimes and your immense support from the very beginning. I would like to express my gratitude for the lengthy scientific discussions we had regarding the experiments simulations, data interpretations and preparing publications. I would like to thank you for all advice both at the scientific and personal life.

The experiments at FLASH have been performed in large collaborations and would not be possible without the distinguishable efforts of Dr. Barbara Keitel, Dr. Elke Plönjes, Dr. Marion Kulmann. I would like to thank the DESY accelerator group, especially Dr. Evgeny Scneidmiller and Dr. Mikail Yurkov for their support during the FLASH beamtime and providing the radiation simulations of the FAST software.

My heartfelt appreciation goes to all SPB/SFX group members for being an integral part of the beamtimes. Dear Dr. Takushi Sato, I would like to thank you regarding many stimulating discussions about x-ray science and lasers.

I would like to thank my good friends at DESY and the European XFEL Mr. Amir Rafipoor, Mr. Sadegh Bakhtiarzadeh and Dr. Pooneh Saffari for their encouragements and continuous support.

I would like to extend my gratitude to my previous supervisors, Prof. Dr. Sergey Vasilevich Gaponenko and Dr. Arashmid Nahal, who helped me in conducting my career.

And last, but not least, it is my very great pleasure to thank my family and my lovely wife Soodabeh, all of whom have shown me their unwavering love and support in all aspects of my life.

Bibliography

[1] H. N. Chapman, A. Barty, M. J. Bogan, and others. Femtosecond diffractive imaging with a soft-x-ray free-electron laser. *Nat. Phys.*, 2:839–843, **2006**.

[2] T. L. Blundell and L. N. Johnson. *Protein Crystallography.* Academic Press, London, **1987**.

[3] M. F. C. Ladd and R. A. Palmer. *Theory and Practice of Direct Methods in Crystallography.* Plenum Press, New York, **1980**.

[4] G. H. Stout and L. H. Jensen. *X-ray Structure Determination: A Practical Guide.* The Macmillan Company, New York, **1986**.

[5] E. Saldin, E.V. Schneidmiller, and M.V. Yurkov. *The Physics of Free Electron Lasers.* Springer, **2000**.

[6] A. Barty, S. Boutet, A. J. Bogan, and others. Ultrafast single-shot diffraction imaging of nanoscale dynamics. *Nat. Photon.*, 2:415–419, **2008**.

[7] A. Barty, J. Küpper, and H. N. Chapman. Molecular Imaging Using X-Ray Free-Electron Lasers. *Annual Review of Physical Chemistry*, 64:415–435, **2013**.

[8] J. Miao, R. L. Sandberg, and C. Song. Coherent x-ray diffraction imaging. *IEEE Journal of Selected Topics in Quantum Electronics*, 18(1):399–410, **2012**.

[9] I. A. Vartanyants, I. K. Robinson, I. McNulty, C. David, P. Wochner, and Th. Tschentscher. Coherent x-ray scattering and lensless imaging at the european xfel facility. *Journal of Synchrotron Radiation*, 14(6):453–470, **2007**.

[10] I. Robinson and R. Harder. Coherent X-ray diffraction imaging of strain at the nanoscale. *Nat. mat.*, 8(march):291–298, **2009**.

[11] J. R. Fienup. Phase retrieval algorithms: a comparison. *App. opt.*, 21(15):2758–69, **1982**.

[12] J. R. Fienup. Phase-retrieval algorithms for a complicated optical system. *App. Opt.*, 32(10):1737, **1993**.

[13] G. J. Williams, H. M. Quiney, A. G. Peele, and K. A. Nugent. Fresnel coherent diffractive imaging: Treatment and analysis of data. *New. J. Phys.*, 12, **2010**.

[14] S. Rutishauser, L. Samoylova, J. Krzywinski, O. Bunk, J. Grünert, H. Sinn, M. Cammarata, D. M. Fritz, and C. David. Exploring the wavefront of hard X-ray free-electron laser radiation. *Nat. comm.*, 3:947, **2012**.

[15] C. Kottler, C. David, F. Pfeiffer, and O. Bunk. A two-directional approach for grating based differential phase contrast imaging using hard x-rays. *Opt. Express*, 15(3):1175–1181, **2007**.

[16] A. Momose, S. Kawamoto, I. Koyama, and et al. Demonstration of x-ray talbot interferometry. *JOSSA*, 42(7B):L866, **2003**.

[17] T. Weitkamp, B. Nöhammer, A. Diaz, C. David, and E. Ziegler. X-ray wavefront analysis and optics characterization with a grating interferometer. *Appl. Phys. Lett.*, 86:054101, **2005**.

[18] T. Weitkamp, A. Diaz, C. David, F. Pfeiffer, M. Stampanoni, P. Cloetens, and E. Ziegler. X-ray phase imaging with a grating interferometer. *Opt. Express*, 13(16):6296–6304, **2005**.

[19] F. Pfeiffer, T. Weitkamp, O. Bunk, and C. David. Phase retrieval and differential phase-contrast imaging with low-brilliance x-ray sources. *Nat. Phys.*, 2:258 – 261, **2006**.

[20] H. R. Bilger and T. Habib. Knife-edge scanning of an astigmatic gaussian beam. *Appl. Opt.*, 24(5):686–690, **1985**.

[21] R. Fulton, J. Haggerty, R. Jared, and et al. A high resolution wire scanner for micron-size profile measurements at the slc. *Nuclear Instruments and Methods in Physics Research Section A: Accelerators, Spectrometers, Detectors and Associated Equipment*, 274(1):37 – 44, **1989**.

[22] H. Mimura, S. Handa1, T. Kimura, and et al. Predicting the coherent x-ray wavefront focal properties at the linac coherent light source (lcls) x-ray free electron laser. *Nat. Phys.*, 2:122 – 125, **2009**.

[23] A. Takeuchi, Y. Suzuki, and K. Uesugi. Differential-phase-contrast knife-edge scan method for precise evaluation of x-ray nanobeam. *JOSSA*, 54(9):092401, **2015**.

[24] F. Zernike. Diffraction theory of the knife-edge test and its improved form, the phase-contrast method*. *Journal of Micro/Nanolithography, MEMS, and MOEMS*, 1(2):87–94, **2002**.

[25] A. Schropp, R. Hoppe, V. Meier, J. Patommel, F. Seiboth, H. J. Lee, B. Nagler, E. C. Galtier, B. Arnold, U. Zastrau, J. B. Hastings, D. Nilsson, F. Uhlén, U. Vogt, H. M Hertz, and C. G. Schroer. Full spatial characterization of a nanofocused x-ray free-electron laser beam by ptychographic imaging. *Scientific reports*, 3:1633, **2013**.

[26] A. Schropp, P. Boye, J. M. Feldkamp, R. Hoppe, J. Patommel, D. Samberg, S. Stephan, K. Giewekemeyer, R. N. Wilke, T. Salditt, J. Gulden, A. P. Mancuso, I. A. Vartanyants, E. Weckert, S. Schöder, M. Burghammer, and C. G. Schroer. Hard x-ray nanobeam characterization by coherent diffraction microscopy. *App. Phys. Lett.*, 96(2010):10–13, **2010**.

[27] L. W. Whitehead, G. J. Williams, H. M. Quiney, D. J. Vine, R. A. Dilanian, S. Flewett, K. A. Nugent, A. G. Peele, E. Balaur, and I. McNulty. Diffractive imaging using partially coherent x rays. *Phys. Rev. Lett.*, 103:243902, **2009**.

[28] C. David, S. Gorelick, S. Rutihauser, J. Krzywinski, J. Villa-Commala, V. A. Guzenko, O. Bunk, E. Färm, M. Ritala, M. Cammarata, D. M. Fritz, R. Barrett, L. Samoylova, J. Grünet, and H. Sinn. Diffractive imaging using partially coherent x rays. *Scientific Reporsts*, 1:57, **2011**.

[29] J. Chalupsk, L. Juha, J. Kuba, and et al. Utilizing ablation of solids to characterize a focused soft x-ray laser beam, **2007**.

[30] J. Chalupský, J. Krzywinski, L. Juha, and et al. Spot size characterization of focused non-gaussian x-ray laser beams. *Opt. Express*, 18(26):27836–27845, **2010**.

[31] H. H. Barret, C. Dainty, and D. Lara. Maximum-likelihood methods in wavefront sensing: stochastic models and likelihood functions. *J. Opt. Soc. Am*, 24:391–414, **2003**.

[32] M. Sikorski, S. Song, A. Schropp, and others.

[33] R. W. Gerchberg and W. O. Saxton. Wave phase from image and diffraction plane pictures. *Image processing and computer-aided design in electron optics*, pages 66–81, **1973**.

[34] S. Marchesini, H. He, H. N. Chapman, S. P. Hau-Riege, A. Noy, M. R. Howells, U. Weierstall, and J. C. H. Spence. X-ray image reconstruction from a diffraction pattern alone. *Phys. Rev. B*, 68(14):140101, **2003**.

[35] V. Elser. Phase retrieval by iterated projections. *Journal of the Optical Society of America. A, Optics, image science, and vision*, 20(1):40–55, **2003**.

[36] H. M. Quiney, A. G. Peele, Z. Cai, D. Paterson, and K. A. Nugent. Diffractive imaging of highly focused X-ray fields. *Nat. Phys.*, 2(2):101–104, **2006**.

[37] K. A. Nugent, A. G. Peele, H. M. Quiney, and H. N. Chapman. Diffraction with wavefront curvature: a path to unique phase recovery. *Acta. Crystallographica. Section A*, 61(3):373–381, **2005**.

[38] T. A. Pitts and J. F. Greenleaf. Fresnel transform phase retrieval from magnitude. *IEEE Transactions on Ultrasonics, Ferroelectrics, and Frequency Control*, 50(8):1035–1045, **2003**.

[39] K. Tiedtke, A. Azima, N. von Bargen, L. Bittner, S. Bonfigt, S. Düsterer, B. Faatz, U. Frühling, M. Gensch, C. Gerth, N. Guerassimova, U. Hahn, T. Hans, M. Hesse, K. Honkavaar, U. Jastrow, P. Juranic, S. Kapitzki, B. Keitel, T. Kracht, M. Kuhlmann, W. B. Li, M. Martins, T. Nunez, E. Plönjes, H. Redlin, E. L. Saldin, E. A. Schneidmiller, J. R .Schneider, S. Schreiber, N. Stojanovic, F. Tavella, S. Toleikis, R. Treusch, H. Weigelt, M. Wellhöfer, H. Wabnitz, M. V. Yurkov, and J. Feldhaus. The soft x-ray free-electron laser flash at desy: beamlines, diagnostics and end-stations. *New. J. Phys.*, 11(2):023029, **2009**.

[40] P. Emma. *Handbook of Accelerator Physics and Engineering*. World Scientific, **2013**.

[41] J. D. Jackson. *Classical Electrodynamics*, volume 1. ACADEMIC PRESS (UK), **1999**.

[42] R. Churchill. *Foureir series and boundary value problem*. McGraw- Hill, New York, 2nd edition, **1963**.

[43] G. Arfken and H. Weber. *Mathematical methods for physicists*. ACADEMIC PRESS, San Diego, CA, 5 edition, **2001**.

[44] D.M.Paganin. *Coherent X-ray Optics*. Oxford University Press, **2006**.

[45] R. T. Michael. Deterministic phase retrieval: a Greens function solution. *J. Opt. Soc. Am.*, 73(11):1434, **1983**.

[46] D. Constales and R. S. Krauhar. Multi-periodic eigensolutions to the dirac operator and applications to the generalized helmholtz equation on flat cylinders and on the n-torus. *Mathematical Methods in the Applied Sciences*, 32(16):2050–2070, **2009**.

[47] J. W. Goodman. *Introduction to Fourier Optics*, volume 1. ROBERTS COMPANY, 3 edition, **2005**.

[48] C. E. Shannon. Communication in the Presence Noise. *PROCEEDING of the I.R.E*, pages 10–21, **1947**.

[49] The shannon sampling theorem and its implications. `http://www-users.math.umn.edu/~lerman/math5467/shannon_aliasing.pdf`. Accessed: 2017-08-10.

[50] P. L. Butzer. A sampling theorem for duration limited function with error calculation. *Information and Control*, 65:55–65, **1977**.

[51] L. Jung-Ping. Controlling the aliasing by zero-padding in the digital calculation of the scalar diffraction. *J. Opt. Soc. Am. A*, 29(9):1956–1964, **2012**.

[52] T. Shimobaba, T. Kakue, N. Okada, M. Oikawa, Y. Yamaguchi, and T. Ito. Aliasing-reduced fresnel diffraction with scale and shift operations. *J. Opt.*, 15(7):075405, **2013**.

[53] O. Levent. Sampling of the diffraction field. *Appl. Opt.*, 39(32):5929–5935, **2000**.

[54] D. G. Voelz and M. C Roggemann. Digital simulation of scalar optical diffraction: revisiting chirp function sampling criteria and consequences. *App. opt.*, 48(32):6132–42, **2009**.

[55] S. Matsuyama, H. Yokoyama, R. Fukui, Y. Kohmura, K. Tamasaku, M. Yabashi, W. Yashiro, A. Momose, T. Ishikawa, and K. Yamauchi. Wavefront measurement for a hard-x-ray nanobeam using single-grating interferometry. *Opt. Express*, 20(22):24977–24986, **2012**.

[56] A. Polo, V. Kutchoukov, F. Bociort, S. F. Pereira, and H. P. Urbach. Determination of wavefront structure for a hartmann wavefront sensor using a phase-retrieval method. *Opt. Express*, 20(7):7822–7832, **2012**.

[57] D. R. Neal, W. J. Alford, J. K. Gruetzner, and M. E. Warren. Amplitude and phase beam characterization using a two-dimensional wavefront sensor. *SPIE*, 2870:72–82, **1996**.

[58] B. Abbey, K. A. Nugent, G. J. Williams, J. N. Clark, A. G. Peele, M. A. Pfeifer, M. De Jonge, and I. McNulty. Keyhole coherent diffractive imaging. *Nat. Phys.*, 4:394–398, **2008**.

[59] G. J. Williams, H. M. Quiney, B. B. Dhal, C. Q. Tran, K. A. Nugent, A. G. Peele, D. Paterson, and M. D. de Jonge. Fresnel coherent diffractive imaging. *Phys. Rev. Lett.*, 97:025506, **2006**.

[60] L. Mandel and E. Wolf. *Optical coherence and quantum optics.* Cambridge University Press, 1 edition, **1995**.

[61] A. Singer, F. Sorgenfrei, A. P. Mancuso, N. Gerasimova, O. M. Yefanov, J. Gulden, T. Gorniak, T. Senkbeil, A. Sakdinawat, Y. Liu, D. Attwood, S. Dziarzhytski, D. D. Mai, R. Treusch, E. Weckert, T. Salditt, A. Rosenhahn, W. Wurth, and I. A. Vartanyants. Spatial and temporal coherence properties of single free-electron laser pulses. *Opt. Express*, 20(16):17480–17495, **2012**.

[62] E. Wolf and M. Born. *Principles of Optics.* Cambridge University Press, London, **1959**.

[63] E. A. Saleh. *Fundamental of Photonics.* John Wiley and Sons,Inc., 1 edition, **1991**.

[64] B. Schäfer, M. Lübbecke, and K. Mann. Hartmann-shack wave front measurements for real time determination of laser beam propagation parameters. *Review of Scientific Instruments*, 77, **2006**.

[65] P. Mercère, P. Zeitoun, M. Idir, S. Le Pape, D. Douillet, X. Levecq, G. Dovillaire, S. Bucourt, K. A. Goldberg, P. P. Naulleau, and S. Rekawa. Hartmann wave-front measurement at 13.4 nm with λeuv/120 accuracy. *Opt. Lett.*, 28(17):1534–1536, **2003**.

[66] B. Schäfer and K. Mann. Determination of beam parameters and coherence properties of laser radiation by use of an extended hartmann-shack wave-front sensor. *Appl. Opt.*, 41(15):2809–2817, May **2002**.

[67] M.J. Greay. Introduction to Wavefront Sensors. *SPIE Optical Engineering Press*, 1, **2015**.

[68] *Hartmann Wavefront Analyzer Tutorial*. www.spirincon.com. Accessed: 2017-06-28.

[69] W. H. Southwell. Wavefront estimation from wavefront slope measurements. *J. Opt. Soc. Am.*, 70(8):998–1006, **1980**.

[70] D. L. Fried. Least-square fitting a wave-front distortion estimate to an array of phase-difference measurements. *J. Opt. Soc. Am.*, 67(3):370–375, **1977**.

[71] B. Pathak and B. R. Boruah. Improved wavefront reconstruction algorithm for shackhartmann type wavefront sensors. *J. of Optics*, 16(5):055403, **2014**.

[72] V. P. Lukin, N. N. Botygina, O. N. Emaleev, and P. A. Konyaev. Wavefront sensors and algorithms for adaptive optical systems. *Proc. SPIE*, 7736:773659, **2010**.

[73] Y. Carmon and E. N. Ribak. Reconstructing wave fronts with varying hartmann rays. *Proc. SPIE*, 4840:453–458, **2003**.

[74] Y. Carmon and E. N. Ribak. Fast fourier demodulation. *App. Phys. Lett.*, 84(23):4656–4657, **2004**.

[75] E. N. Ribak, Y. Carmon, A. Talmi, O. Glazer, and C. Canovas. Hartmann fourier analysis for sensing and correction. *Adaptive Optics: Analysis and Methods/Computational Optical Sensing and Imaging/Information Photonics/Signal Recovery and Synthesis Topical Meetings on CD-ROM*, page AWC3, **2007**.

[76] C. Canovas and E. N. Ribak. Comparison of hartmann analysis methods. *Appl. Opt.*, 46(10):1830–1835, **2007**.

[77] Y. Carmon and E. N. Ribak. Phase retrieval by demodulation of a hartmannshack sensor. *Opt. Comm.*, 215(46):285 – 288, **2003**.

[78] N. Zon, O. Srour, and E. N. Ribak. Hartmann-shack analysis errors. *Opt. Express*, 14(2):635–643, **2006**.

[79] M. Takeda and K. Mutoh. Fourier transform profilometry for the automatic measurement of 3-d object shapes. *Appl. Opt.*, 22(24):3977–3982, **1983**.

[80] C. Roddier and F. Roddier. Interferogram analysis using fourier transform techniques. *Appl. Opt.*, 26(9):1668–1673, **1987**.

[81] K. Ishizuka and B. Allman. Phase measurement of atomic resolution image using transport of intensity equation. *Journal of Electron Microscopy*, 54(3):191–197, **2005**.

[82] J. C. Wyant and K. Creath. Basic wavefront aberration theory for optical metrology. *Applied Optics and Optical Engineering*, l:1–53, **1992**.

[83] Welford. F. A. Aberrations of optical system, **1986**.

[84] E. A. Schneidmiller and M. V. Yurkov. Coherence properties of the radiation from flash. *Journal of Modern Optics*, 64:293–308, **2016**.

[85] Hartmann-shack wavefront sensor (visible ir spectral range). `http://www.llg-ev.de`. Accessed: 2017-04-27.

[86] B. Flöter, P. Juranić, S. Kapitzki, B. Keitel, K. Mann, E. Plönjes, B. Schäfer, and K. Tiedtke. Euv hartmann sensor for wavefront measurements at the free-electron laser in hamburg. *New. J. Phys.*, 12(8):083015, **2010**.

[87] M. A. Schofield and Y. Zhu. Fast phase unwrapping algorithm for interferometric applications. *Opt. Lett.*, 28(14):1194–1196, **2003**.

[88] R. Cusack and N. Papadakis. New robust 3-d phase unwrapping algorithms: Application to magnetic field mapping and undistorting echoplanar images. *NeuroImage*, 16:754–764, **2002**.

[89] J. Vila-Comamala, A. Diaz, M. Guizar-Sicairos, A. Mantion, C. M. Kewish, A. Menzel, O. Bunk, and C. David. Characterization of high-resolution diffractive x-ray optics by ptychographic coherent diffractive imaging. *Opt. Express*, 19(22):21333–21344, **2011**.

[90] D. Shapiro, P. Thibault, T. Beetz, and et al. Biological imaging by soft x-ray diffraction microscopy. *Proceedings of the National Academy of Sciences of the United States of America*, 6:15343–15346, **2005**.

[91] A. Barty, R. Soufli, T. McCarville, and et al. Predicting the coherent x-ray wavefront focal properties at the linac coherent light source (lcls) x-ray free electron laser. *Opt. Express*, 17(18):15508–15519, **2009**.

[92] B. Keitel, E. Plönjes, S. Kreis, M. Kuhlmann, K. Tiedtke, To. Mey, B. Schäfer, and K. Mann. Hartmann wavefront sensors and their application at FLASH. *Journal of Synchrotron Radiation*, 23(1):43–49, **2016**.

[93] F. Mastropietro, D. Carbone, A. Diaz, J. Eymery, A. Sentenac, T. H. Metzger, V. Chamard, and V. Favre-Nicolin. Coherent x-ray wavefront reconstruction of a partially illuminated fresnel zone plate. *Opt. Express*, 19(20):19223–19232, **2011**.

[94] D. R. Luke, J. V. Burke, and R. G. Lyon. Optical wavefront reconstruction: Theory and numerical methods. *SIAM Review*, 44(2):169–224, **2002**.

[95] D. Sayre. Some implications of a theorem due to Shannon. *Acta. Crystallographica.*, 5(6):843, **1952**.

[96] B. Sch˙ {FEL} beam characterization from measurements of the wigner distribution function. *Nuclear Instruments and Methods in Physics Research Section A: Accelerators, Spectrometers, Detectors and Associated Equipment*, 654(1):502 – 507, **2011**.

[97] G. J. Williams, H. M. Quiney, A. G. Peele, and K. A. Nugent. Coherent diffractive imaging and partial coherence. *Phys. Rev. B*, 75:104102, **2007**.

[98] J. Perina. *Coherence of light.* REIDEL PUBLISHING COMPANY, 2 edition, **1985**.

[99] E. Wolf. New spectral representation of random sources and of the partially coherent fields that they generate. *Opt, Comm.*, 38(1):3 – 6, **1981**.

[100] R. Martínez-Herrero. Expansion of complex degree of coherence. *Il Nuovo Cimento B (1971-1996)*, 54(1):205, **2008**.

[101] M. W. Kowarz and G. S. Agarwal. Bessel-beam representation for partially coherent fields. *J. Opt. Soc. Am. A*, 12(6):1324–1330, **1995**.

[102] S. R. Seshadri. Partially coherent gaussian schell-model electromagnetic beams. *J. Opt. Soc. Am. A*, 16(6):1373–1380, **1999**.

[103] Z. Qin, R. Tao, P. Zhou, X. Xu, and Z. Liu. Coherence evolution of partially coherent beams carrying optical vortices propagating in non-kolmogorov turbulence. *Appl. Opt.*, 52(33):8176–8183, **2013**.

[104] A. Schell. A technique for the determination of the radiation pattern of a partially coherent aperture. *IEEE Transactions on Antennas and Propagation*, 15(1):187–188, **1967**.

[105] K. A. Nugent. A generalization of schell's theorem. *Opt. Comm.*, 79(5):267 – 269, **1990**.

[106] G. R. Ayers and J. C. Dainty. Iterative blind deconvolution method and its applications. *Opt. Lett.*, 13(7):547–549, **1988**.

[107] J. N. Clark, X. Huang, R. Harder, and I. K. Robinson. High-resolution three-dimensional partially coherent diffraction imaging. *Nat. Comm.*, 3, **2012**.